UNIVERSITÀ DI SIENA 1240

UNIONE EUROPEA
FSE REACT-EU

Percorso dottorale sviluppato con il sostegno finanziario del programma PON REACT-EU

Dipartimento di Biotecnologie, Chimica e Farmacia

Dottorato in Chemical and Pharmaceutical Sciences

XXXVII Ciclo

Coordinatore: Prof. Maurizio Taddei

Repurposing human Carbonic Anhydrase 2 for artificial photosynthesis: structural and functional role of selected transition metals

Settore scientifico disciplinare: *CHEM-03/A*

Candidata

Beatrice De Bonis

Dipartimento di Biotecnologie, Chimica e Farmacia

Supervisore

Prof.ssa Cecilia Pozzi

Dipartimento di Biotecnologie, Chimica e Farmacia

Co-supervisori

Dr. Marco Mazzorana

Diamond Light Source

Dr.ssa Giusy Tassone

Dipartimento di Biotecnologie, Chimica e Farmacia

Beatrice De Bonis
07.05.2025
18:45:00
GMT+02:00

Anno accademico di conseguimento del titolo di Dottore di ricerca

2023/2024

Università degli Studi di Siena
Dottorato in Chemical and Pharmaceutical Sciences
XXXVII Ciclo

Data dell'esame finale
19/05/2025

Commissione giudicatrice
Prof. Marco Consumi
Prof. Massimiliano Perduca
Prof. Duccio Rocchini

Supplenti
Prof.ssa Sandra Furlanetto

A mio padre, mia madre e mio fratello,
a voi devo tutto.

.

Acknowledgments

Writing this thesis has led me to reflect on my entire PhD journey, a path marked by both challenges and successes, moments of frustration and joy. It has been a transformative experience that has pushed me to grow, to face difficulties with determination, to continuously challenge myself, and to cultivate a constant desire to learn. Like any meaningful journey, this one was not undertaken alone. For this reason, I would like to sincerely thank all those who have been part of it.

First of all, I acknowledge BANDO PON 37° ciclo - REACT-EU FSE DM 1061 del 10/08/2021 PhDs on Green Themes for providing the funding for the PhD project.

I would like to express my gratitude to my supervisor, Prof. Cecilia Pozzi, for her invaluable guidance, continuous support, and the wealth of knowledge she has shared with me throughout these years. Her professionalism, dedication, and encouragement have been instrumental in my academic progress.

I would also like to extend my sincere gratitude to my co-supervisor, Dr. Marco Mazzorana, for the incredible opportunity to spend six months at the Diamond Light Source in the UK. I am deeply thankful for all the teachings, advice, and guidance I received during my time there. It was a truly rewarding experience that has contributed immensely to my growth and development.

I am very grateful to my co-tutor, Dr. Giusy Tassone, for his continuous support throughout this journey. His availability, valuable advice, and constant encouragement have had a significant impact on my research experience. I have always felt supported, not only during difficult times but also when I needed motivation. I am deeply thankful for the time, patience, and encouragement he has generously given me along the way.

I would like to thank my colleagues in Italy and the UK for the scientific discussions, technical and personal support, and for creating a working environment that was both stimulating and collaborative.

A special thought goes to my family: in particular, to my parents, who have always supported me with love and discretion and believed in me; to my brother, for all the strength and determination he has given me every single day; and to someone special for sharing with me the challenges and rewards of this journey, with patience, love, and unwavering strength.

Finally, thank you to all my friends, near and far, who have been there and made this journey a little less difficult, filling it with laughter and joy.

To all of you, my deepest gratitude.

Beatrice De Bonis

Table of contents

Abstract

Natural photosynthesis has inspired the development of artificial systems designed to convert solar energy into chemical energy. In this context, artificial photosynthesis (AP) presents a promising approach for sustainable energy production, particularly through light-driven water splitting, which generates non-polluting by-products such as oxygen (O_2) and hydrogen (H_2). This study aims to develop and optimize novel biological catalysts for AP applications, focusing on human carbonic anhydrase II (hCA2), a ubiquitous enzyme that catalyses the reversible hydration and dehydration of carbon dioxide and bicarbonate. The catalytic activity of hCA2 relies on a Zn^{2+} ion, which is tetrahedrally coordinated by three histidine residues in the enzyme's active site. Previous studies have demonstrated that substituting Zn^{2+} with other metal ions (e.g., Co^{2+}, Ni^{2+}, Cu^{2+}) can significantly alter the enzyme's catalytic properties, opening new possibilities for different applications.

In this work, we explored metal-substituted hCA2, focusing on Ir^{3+}-substituted enzyme, as previous research suggested that the combination with this ion may drive unique water-splitting properties. To investigate this, hCA2 was expressed as a recombinant enzyme in *Escherichia coli*, and the active protein was purified through multiple steps, including affinity and size-exclusion chromatography. Following zinc removal by chelation, the apo-protein was used to generate various metal-substituted variants. These engineered enzymes were then characterized through isothermal titration calorimetry and X-ray crystallographic analysis to determine their metal-binding properties and structural integrity. Additionally, we evaluated the water-splitting capabilities of the metal-substituted hCA2 variants for AP applications.

Structural analysis of the metal-substituted enzymes highlighted the peculiar properties of each histidine residue involved in metal binding in relationship with the catalytic function. Notably, the discovery of a second binding site, located between residues 4 and 64, was explored with five alanine variants: H94A, H96A, and H119A (targeting the catalytic site) and H4A (targeting the second accessory site). Structural characterization and esterase kinetic assays of these variants provide deeper insights into the role of these residues in site stabilization and enzymatic activity.

This work also advances our understanding of enzyme-metal interactions and coordination geometry in catalytic processes through the characterization of hCA2, its alanine variants, and the substitution of different metals in the catalytic centre. These findings pave the way for future studies on substrate binding and metal coordination mechanisms, ultimately contributing

to the design of engineered enzymes with improved catalytic efficiency, increased oxygen production turnover rates, and enhanced long-term stability. Such advances could facilitate the large-scale implementation of biocatalysts in AP and sustainable energy technologies.

Abbreviations

ADA	N-(2-acetamido)iminodiacetic acid
Apo-hCA2	hCA2 with zinc ion removed
Cp*	Pentamethylcyclopentadiene
bCA2	bovine CA isozyme II
BES	N,N-Bis(2-hydroxyethyl)taurine
Bis-tris	Bis(2-hydroxyethyl)amino-tris(hydroxymethyl)methane.
bpy	2,2′-bipyridine
bpm	2,2′-bipyrimidine
CA	Carbonic anhydrase
CAN	Ceric ammonium nitrate
DSF	Differential scanning fluorimetry
DLS	Diamond Light Source
DNA	Deoxyribonucleic acid
DTT	Dithiothreitol
E. Coli	Escherichia coli
EDTA	Ethylenediaminetetraacetic
EDC	1-Ethyl-3-(3-dimethylaminopropyl)carbodiimide
ESRF	European Synchrotron Radiation Facility
hCA2	human CA isozyme II
HER	Hydrogen evolution reaction
HOMO	Highest occupied molecular orbital
HEPES	2-[4-(2-hydroxyethyl) piperazin-1-yl] ethane sulfonic acid
IEA	International Energy Agency

IMAC	Immobilized Metal Affinity Chromatography
ITC	Isothermal titration calorimetry
MALDI	Matrix assisted laser desorption/ionization
MW	Molecular weight
MOPS	3-morpholinopropane-1-sulfonic acid
MS	Mass spectrometry
NHE	Normal hydrogen electrode
NHS	N-Hydroxysuccinimide
PCET	Proton-coupled electron transfer
POM	Polyoxometalate
PSI	Photosystem I
PSII	Photosystem II
ppy	Phenylpyridine
PCR	Polymerase chain reaction
PDB	Protein Data Bank
POM	Polyoxotungstate
R.m.s.d	Root mean square deviation
SDS−PAGE	Sodium dodecyl−sulphate polyacrylamide gel electrophoresis
SEC	Size-exclusion chromatography
SPR	Surface plasmon resonance
TAML	Tetraamido macrocyclic ligand
T_m	Melting temperature
TMPD	N,N,N′,N′-tetramethyl-p-phenylenediamine
TOF	Turnover frequency

TON	Turnover number
TRIS	Tris(hydroxymethyl)aminomethane
UV	Ultraviolet
Wt	Wild type
ZYP−5052	ZYP−5052 auto−induction medium
WOC	Water oxidation catalyst
WMO	World Meteorological Organization
ε	Molar extinction coefficient

Chapter 1

Artificial photosynthesis

1.1 Introduction: the global energy crisis

The global energy crisis represents one of the major challenges of the 21st century. Innovative strategies and new energy sources are required to ensure a sustainable future for the planet. The analysis of global trends for energy production highlights the strong correlation with the rising of fossil fuel consumption and CO_2 emissions (Figure 1.1).[1] Despite the progression of low-carbon technologies[2] and the efforts in lowering the overall energy consumption,[3] fossil fuels (including coal, oil, and natural gas) are still the dominant energy source, applied worldwide for industrial activities, transportation, and residential needs.[4]

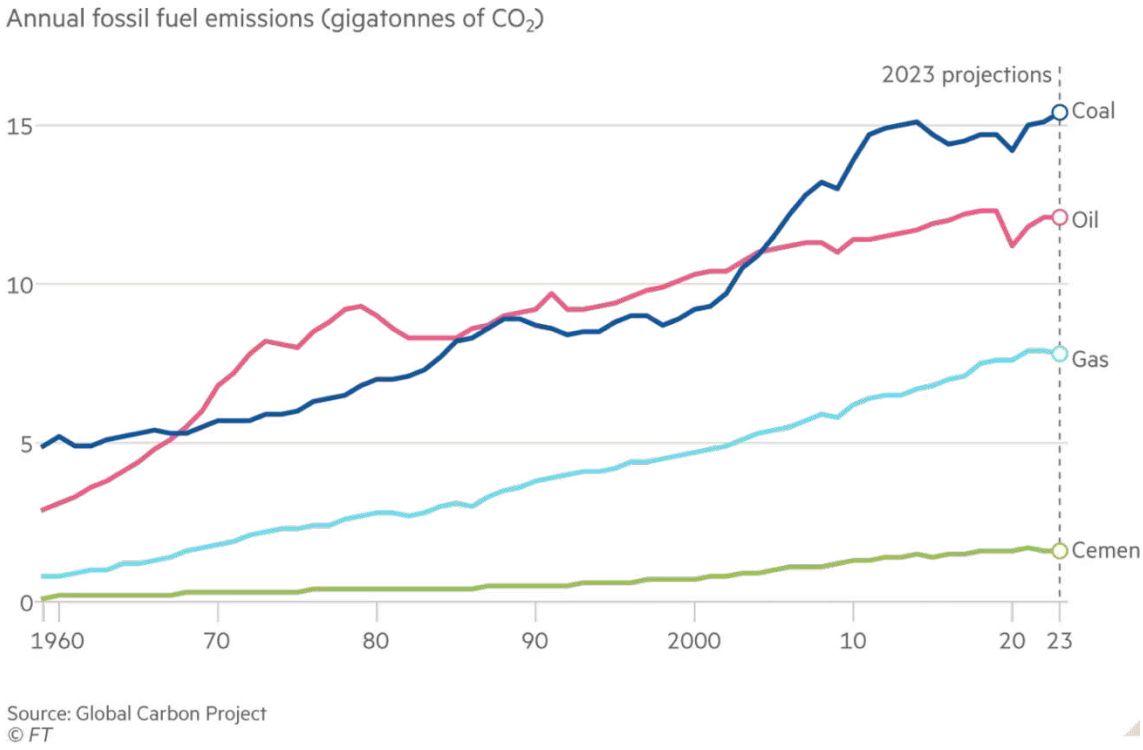

Figure 1.1: Annual global carbon dioxide emissions from burning coal, oil and gas.[1]

Increased CO_2 emissions accelerate global warming, triggering climate changes such as melting polar ice caps, rising sea levels, and increased frequency and severity of extreme weather events (*i.e.*, hurricanes, droughts, and wildfires).[5] The World Meteorological Organization (WMO) has officially confirmed 2024 as the warmest year, recording a 1.55 °C increase in global temperatures compared to the pre-industrial era. Notably, the recent years have seen a steady increase in the average temperature (Figure 1.2).[6]

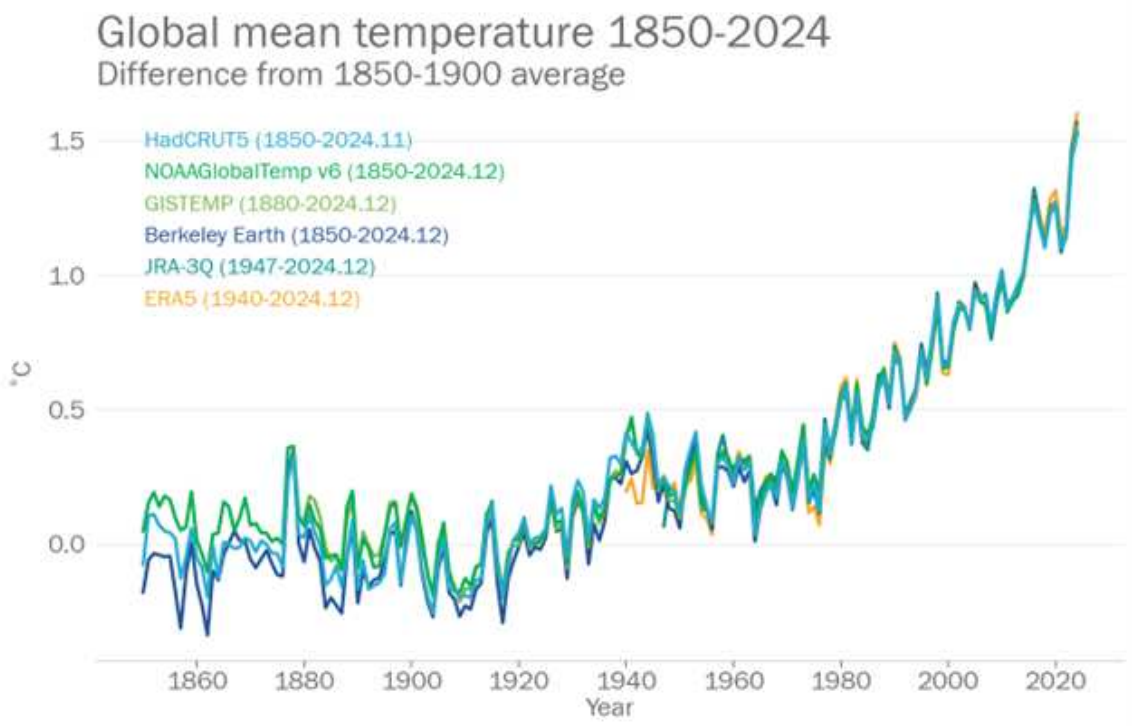

Figure 1.2: Evolution of the global mean temperature from 1850 to 2024, as reported by the WMO, illustrating the significant warming trend over the past century.[6]

Given the urgent need to accelerate the global transition to sustainable energy forms, the International Energy Agency (IEA) outlined a roadmap to achieve 'net zero emissions' by 2050, focusing on two critical steps: *i*) reduction of global energy demand from 632 to 541 exajoules; *ii*) replacement of fossil fuels with renewable energy sources (*e.g.*, solar, wind, and hydroelectric power). To effectively proceed in this latter step, IEA has estimated that fossil fuel reliance should decrease from 80% to 17% of total energy production, while renewable energy must increase from 12% to 71% (Figure 1.3).[7]

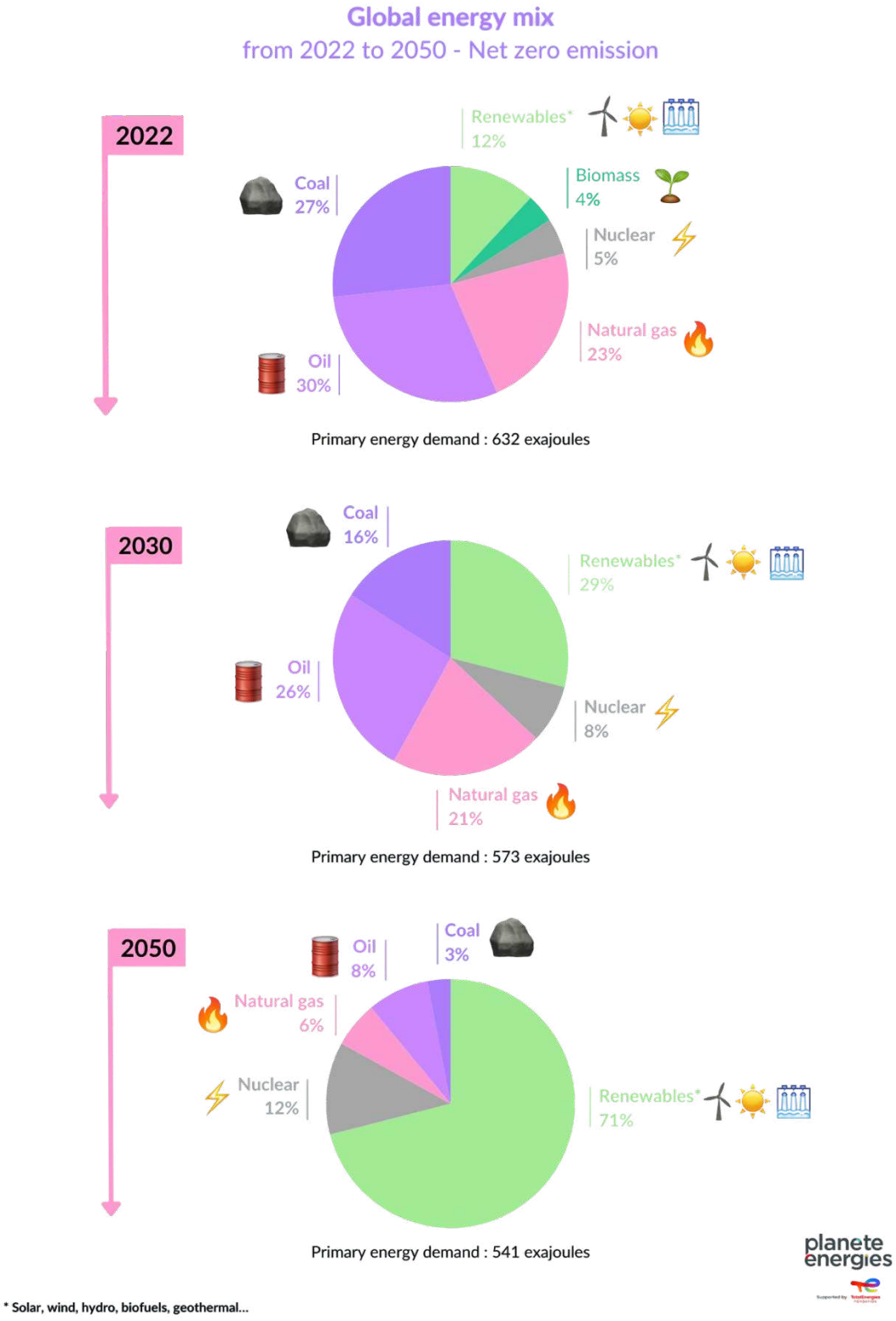

Figure 1.3: The road map from 2022 to 2050-net zero emission reported by International Energy Agency (IEA).[7]

1.2 Solar energy

The amount of energy per year supplied by the sun to our planet greatly exceeds the global demand. In the last decades, this remarkable evidence has driven the scientific community in the development of innovative technologies able to convert solar energy into fuels and electricity.[8,9,10,11] Therefore, one of the major challenges of the 21st century is to find effective ways to transform abundant, energy-poor molecules into energy-rich compounds, using sunlight as primary energy source.[12] To this purpose, solar energy should be firstly harvested (*e.g.*, by photovoltaic devices), and then converted into exploitable forms of energy (*e.g.*, energy-rich compounds).[9] In recent years, remarkable advancements have been made in the efficiency of photovoltaic devices, directly converting incident sunlight into electrical energy[10] (Figure 1.4).[13]

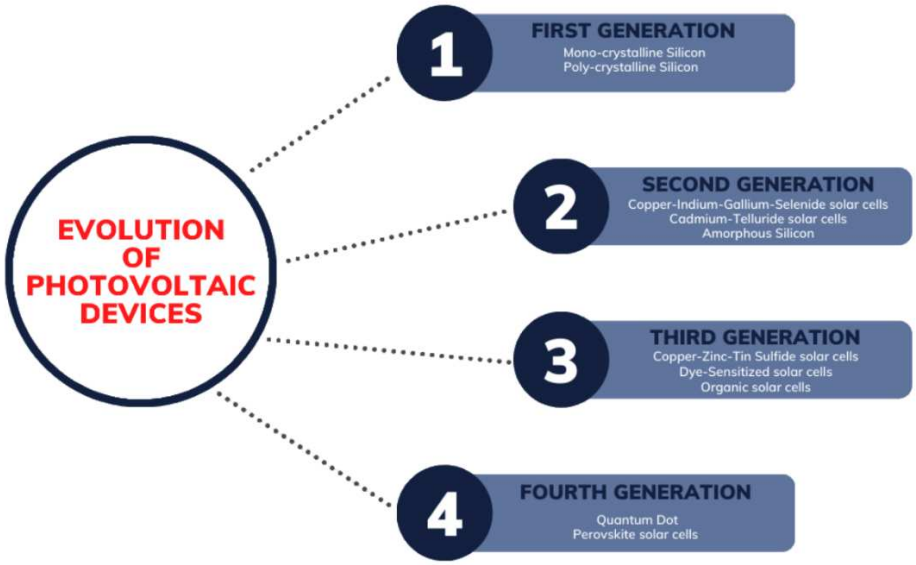

Figure 1.4: The four main generations of Photovoltaic Solar Cells.

Another strategy for harnessing solar energy is by storing it in the form of chemical bonds, a process that is naturally performed during photosynthesis. Mimicking this complex natural process poses major challenges in the development of efficient systems for both solar energy capture and energy conversion and storage in chemical compounds[8]. The nature-inspired process termed artificial photosynthesis aims to effectively harvest solar energy and store it in chemical fuels, avoiding environment-poisoning byproducts.

1.3 Natural and Artificial Photosynthesis

Photosynthetic organisms, as plants and algae, naturally catalyse the conversion of CO_2 and water into oxygen and carbohydrates (Eq. 1):

$$CO_2 + 12\ H_2O \rightarrow C_6H_{12}O_6 + 6\ O_2 + 6\ H_2O \qquad (1)$$

The photosynthetic process relies on two main stages (Figure 1.5). In the first of them, sunlight drives the endergonic splitting of water into dioxygen and dihydrogen, storing reducing equivalents in the $NADP^+$/NADPH conversion. The light-driven water oxidation takes place in Photosystem II (PS-II), a membrane-embedded pigment/protein super-complex.

The active site of PS-II catalyses the water splitting reaction through an oxygen-evolving complex (OEC) based on an oxo-bridged manganese–calcium cluster (Mn_4CaO_5).[14] Electrons and protons released in this reaction are transported across the membrane by complex protein systems to the Photosystem I (PS-I), where a second light-driven event allows to exploit them for catalysing the $NADP^+$/NADPH conversion and the phosphorylation of ADP to produce ATP. During this second stage, the chemical energy stored in NADPH and ATP is used as fuel for converting CO_2 into carbohydrate products. This process, known as Calvin-Benson cycle, (also referred to as the 'dark reaction'), is pivotal for the production of chemical energy in the form of sugars, used to support all vital processes, in plants and other photosynthetic organisms.[15,16,17]

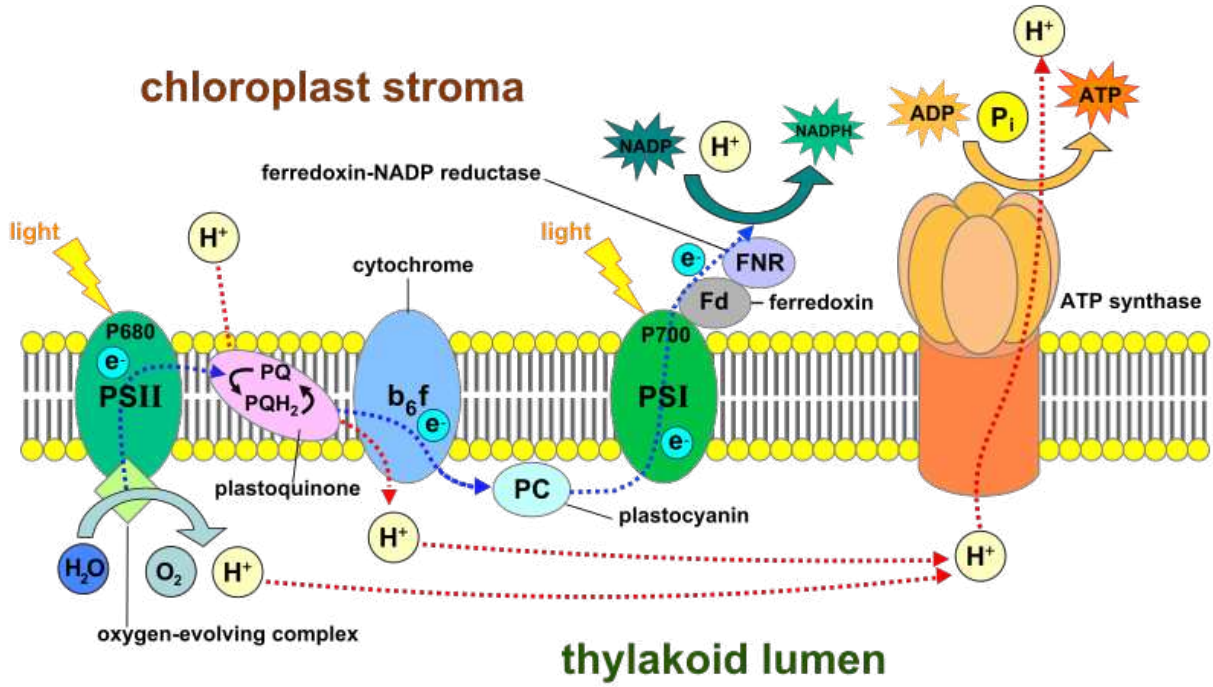

Figure 1.5: Schematic representation of the light-dependent reactions and electron transfer processes in natural photosynthesis. The system comprises four key protein complexes embedded in the thylakoid lumen: PSII, the cytochrome b6f complex, PSI, and ATP synthase. These complexes work together to facilitate the capture of light energy, electron transport, and ATP synthesis (*Image reprinted from Wikimedia Commons and licensed under **CC BY-SA 4.0s).*[18]

Artificial photosynthesis (AP) is a promising, nature-inspired approach that combines solar-driven water splitting with CO_2 consumption to produce hydrocarbons (Figure 1.6).[19] Guan *et al*. firstly proposed to use hybrid photocatalysts for mimicking the core processes of natural photosynthesis.[20]

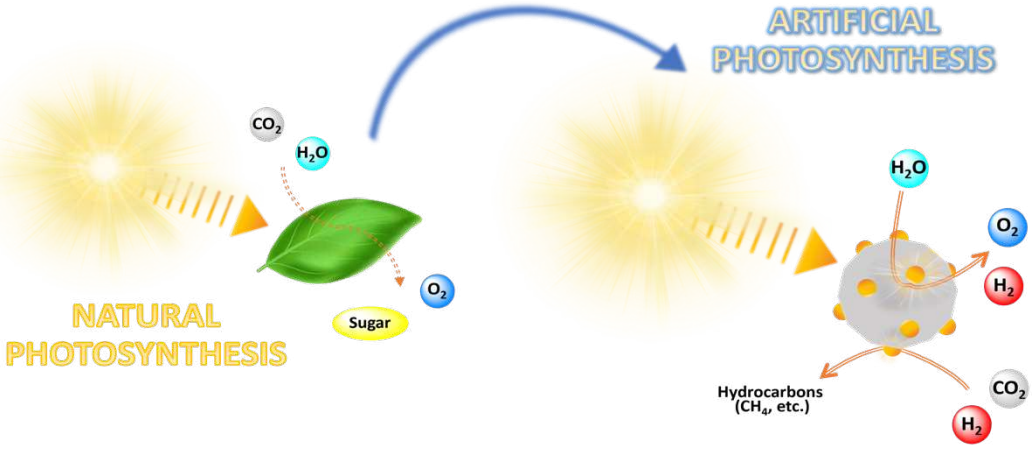

Figure 1.6: Conversion of solar energy: comparison between natural photosynthesis in a leaf and its replication in artificial systems through photocatalysis. Reproduced from Ref.[19]

AP systems are designed to mimic the natural PS-II, harnessing solar energy to drive the splitting of water into molecular oxygen and hydrogen (eq. 4). The overall process requires the coupling of two half-reactions: *i*) water oxidation to generate reducing equivalents (electrons) and molecular oxygen (oxygen evolving reaction, OER; eq 2) and *ii*) proton reduction to produce molecular hydrogen (hydrogen evolving reaction, HER; Eq 3). The whole water splitting process (eq. 4) is highly thermodynamically disfavoured ($\Delta G = +238$ kJ/mol).[21,22,23] Therefore, efficient photo or electro-catalysts are required to overcome this high energy barrier.

$$2\ H_2O \rightarrow O_2 + 4\ H^+ + 4\ e^- \quad (2)$$

$$4\ H^+ + 4\ e^- \rightarrow 2\ H_2 \quad (3)$$

$$2\ H_2O \rightarrow O_2 + 2\ H_2 \quad (4)$$

In OER, the process starts with the binding of a water molecule to the catalyst, where it loses a proton to form a hydroxyl species. Subsequently, it undergoes oxidation and deprotonation, creating a high-energy intermediate that promotes O–O bond formation and dioxygen production.[24] OER is a complex, four-electron process, requiring effective catalysts and a strong energy source to promote this highly disfavoured reaction.

The second stage is the HER, an electrochemical process in which protons are reduced to produce hydrogen gas.[24] A crucial aspect for HER is an effective proton-coupled electron transfer (PCET), allowing the OER products to diffuse in the reaction medium and to reach the catalysis for the second half-reaction.[25–27]

1.4 AP devices

The main goal in developing AP devices is to reach high efficiencies in simple systems, enabling large-scale implementation and industrial production of chemical fuels from solar energy. An efficient AP device requires specific dedicated systems, assembled in a well-defined sequence. The first system needed is a photosensitizer which absorbs a photon and subsequently transfers an electron to a reduction catalyst, creating a light-induced charge-separation. By a second light-induced event, the catalyst accumulates two electrons required to reduce two protons, forming molecular hydrogen. The photosensitizer is then regenerated through electron transfers from an oxidation catalyst, able to supply the electrons arising from the water splitting reaction, which further produces molecular oxygen and protons[28,29,22].

These processes can be implemented using either a single-step or a two-step approach, depending on the configuration of the device. In the single-step approach (Figure 1.7), photon

absorbers, such as semiconductors or dyes, have a peculiar chemical structure allowing to create electron-pair holes upon light absorption. To improve charge separation and energy transfer efficiency, these absorbers are often coupled with electron donors and acceptors. Despite its simplicity, the single-step process has an important limitation since it can exploit only a small fraction of sunlight (λ <680 nm) to drive both oxidation and reduction reactions.[21,23] A significant advancement in single-step devices was achieved by the introduction of semiconductors and metal oxide electrodes (*e.g.,* TiO_2 photoelectrode) working without co-catalysts. In this photoelectrochemical cells, photo-induced electron transfers occur at the TiO_2–electrolyte interface, allowing OER at the TiO_2 electrode and HER at a platinum counter-electrode.[30]

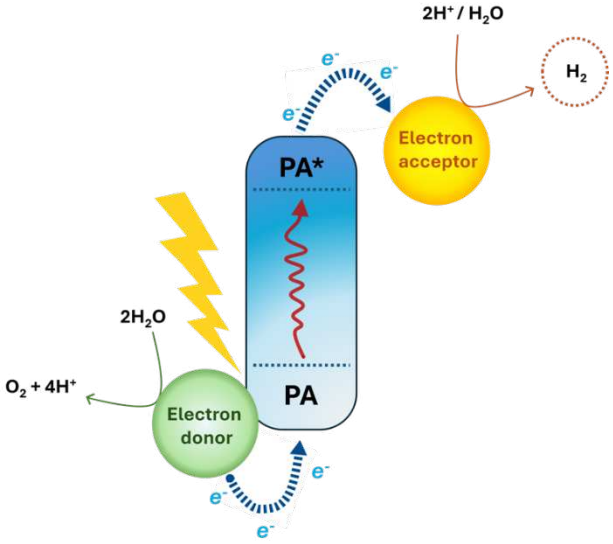

Figure 1.7: Schematic representation of an AP device relying on a single-step approach. Reproduced from Ref.[23]

On the other hand, the two-step approach (Figure 1.8) employs two photon absorbers connected by an electron transfer relay, mimicking the Z-scheme of natural photosynthesis. By this approach, two separate light absorption events occur at both sides. At first, the absorption of light promotes electron transfer from the donor catalysis, activating the water splitting catalysis. At the other side, a second light driven electron transfer occurs, supplying electrons to the acceptor and activating the proton reduction. Even if more efficient then the former, also this approach has challenges in keeping an efficient electron transfer, since charge recombination can cause meaningful energy losses.[21,23]

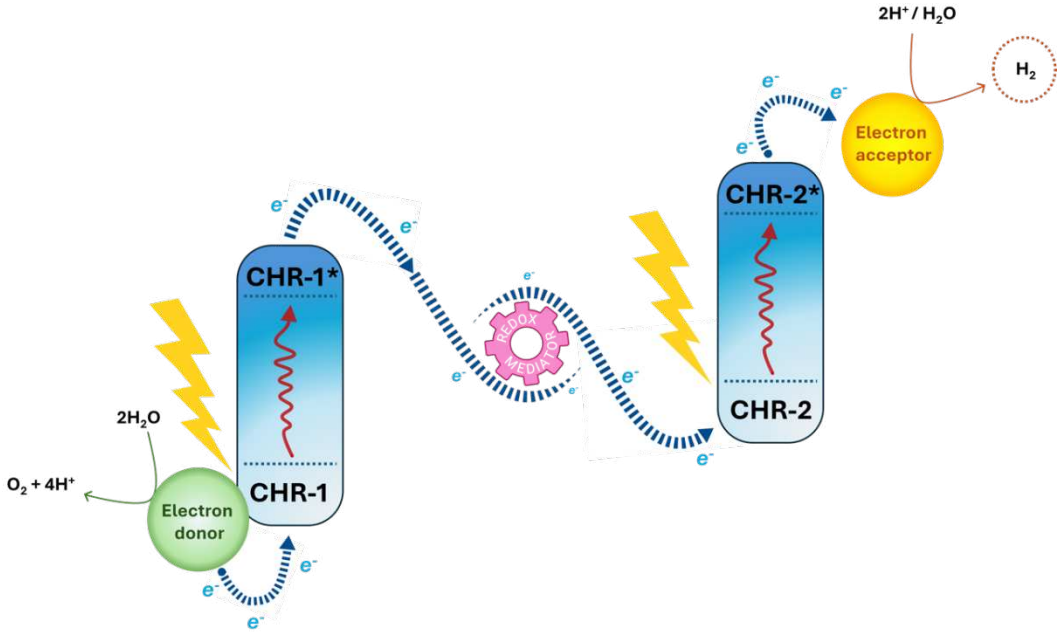

Figure 1.8: Schematic representation of artificial photosynthesis- a two-step process. Reproduced from ref.[23]

Several strategies have been proposed to enhance two-step devices, relying on Z-scheme systems.[31] A first strategy explored a Z-scheme based on the IO_3^-/I^- redox couple, where the redox species attached to the semiconductor surface controls the water splitting/electron transfer process.[32,33] A second strategy relied on a CdS–Au–TiO_2 Z-scheme system with a vectorial electron-transfer path, enhancing the charge separation and the overall efficiency.[34] A third strategy exploited a combined structure of two distinct semiconducting nanomaterials, promoting a rapid electron transfer.[35] Later on, tandem cell configurations, combining an oxygen-evolving electrode with a dye-sensitized TiO_2 electrode, were explored leading to improved light absorption, charge transfer, and water splitting efficiency.[36]

1.5 AP Catalysts

Three major types of catalysts were developed for application in AP devices: *i*) molecular catalysts, *ii*) material-based catalysts, and *iii*) biological catalysts.[37] The development of efficient HER catalysts requires a good balance between high activity, stability, and selectivity on one side, and cost-effectiveness and scalability on the other. To reduce reliance on expensive noble metals, the new research directions are focuses on transition metal-based materials, such as metallo-phosphides and metallo-sulfides, showing good catalytic rates and enhanced sustainability.[38–40]

The optimization of OER catalysts requires a comprehensive understanding of the reaction mechanism. Indeed, reaction intermediates can interact and interfere with the catalysts, significantly affecting adsorption energies, reaction kinetics, and energy barriers.[41,24] Therefore, efficiency of AP systems should rely on OER catalyst with minimized energy losses and stable reaction intermediates.

1.5.1 Molecular catalysts

Over the years, different systems have been developed and investigated as water oxidation catalysts (WOCs). WOCs can be classified in two main categories: *i*) heterogeneous molecular catalysts, providing simple and cost-effective synthetic processes, and *ii*) homogeneous molecular catalysts, having improved activity and offering deeper mechanistic insights. The first heterogeneous WOCs were developed using transition metals from groups 7, 8, and 9, having primarily catalytic properties as oxides, like IrO_2, Co_3O_4, RuO_2, $NiCo_2O_4$, Rh_2O_3, and Mn_2O_3.[42,43]

On the other hand, the first homogeneous WOC was the ruthenium bipyridinium complex, the $[\{RuIII(bpy)_2(H_2O)\}_2O]^{4+}$ ion, also known as the "blue dimer".[44] The blue dimer was shown to promote oxygen evolution in stoichiometric proportions when combined with cerium (IV). The mechanistic studies demonstrated that it acts as a dimer with two oxo-bridging ligands connecting the two ruthenium centres, both acquiring a +5 oxidation state. Furthermore, the final oxidation is not a proton-coupled process, resulting in a pH-independent water oxidation potential of ~1.44 V.[45] Following the blue-dimer, the catalytic activity of ruthenium complexes with various ligands was extensively explored, leading to meaningful improvements in water oxidation rates. [22,46,47,48,49,50] In 2004, Llobet *et al*. introduced a ruthenium dimer for water oxidation, utilizing the Hbpp ligand (3,5-bis(2-pyridyl)pyrazole) to enforce a *cis* configuration of the metal centres. Upon addition to cerium(IV), the complex catalysed oxygen evolution at a rate of 0.014 turnovers per second.[48] Paul, Papish, Grotjahn, and colleagues greatly enhanced the activity of mononuclear Ru(terpy)(bpy) catalysts by incorporating pendant electron-donating ligands, such as −OH and −OMe, on the bpy unit.[51] Sun *et al*. described a three-component system consisting of persulphate as an electron acceptor, a $Ru(II)(bpy)_3$ derivative as a sensitizer, and Ru-based mononuclear complexes of the $Ru(NNN\text{-pincer})(4\text{-picoline})_2$ type as catalysts.[52]

Since the metal composition of the natural OEC, manganese complexes were also deeply investigated as WOCs.[53–55] In 1994, the synthesis and characterization of a triple-dimeric

manganese triphenyl-porphyrin complex, having catalytic activity in the electrochemical oxidation of water, was reported.[56] Another example of a multinuclear manganese complex active as WOC was a soluble manganese-oxo cluster with 12 Mn centres reported by Christou *et al*. The cluster is active as WOC at a low overpotential (334 mV) under slightly acidic conditions.[57] Another highly abundant and cost-effective metal ion explored as WOC was iron.[54,58] Further developments were reported later on by Bernhard and collaborators, demonstrating the WOC activity of TAMLs immobilized on glassy carbon and coupled with cerium(IV) ammonium nitrate as oxidant. These systems were able to reach turnover numbers significantly higher than those of previous homogeneous systems.[59]

Cobalt-based WOCs were also developed, reporting significant examples as fluorinated phthalocyanine, porphyrins, and corrole cobalt complexes.[60,61] For cobalt complexes, the development of true heterogeneous catalysts remains challenging since cobalt salts in solution can promote oxygen evolution.[54,62] Hill *et al*. provided examples of cobalt catalysts, reporting a fast, soluble, and homogeneous cobalt-based water oxidation catalyst having polyoxotungstate (POM) ligands.[63] Berlinguette *et al*. introduced $Co(PY5)(OH_2)_2$, a single-site Co(II) complex featuring a pentadentate ligand, that demonstrated catalytic activity in water oxidation.[64]

The chemistry of iridium was also explored for WOC development. In 2008, a family of cyclometalated iridium complexes, $[Ir(ppy)_2(H_2O)_2]^+$ (ppy = phenylpyridine), featuring two phenylpyridine ligands, was firstly reported.[65] These complexes have two open coordination sites, allowing water binding directly to the iridium centre to perform the WOC activity using Ce^{4+} as a sacrificial oxidant.[22] Later on, a new class of iridium-based WOCs incorporating a pentamethylcyclopentadienyl (Cp*) ligand was reported. Since its electron-donating properties, the Cp* ligand was introduced to improve the catalytic efficiency, showing improved O_2 evolution rates with respect to the former cyclometalated iridium catalysts.[66] Iridium-based catalysts will be further discussed in Chapter 4 of this Thesis.

1.5.2 Material Catalysts

Recent advancements in nanomaterial fabrication have improved the development of various hetero nanostructures exploitable for water splitting reactions.[67] The rapid progress in this field has been extensively documented, emphasizing both innovative fabrication techniques and advancements in well-established wide-bandgap semiconductors such as TiO_2 and ZnO, being highly effective in photocatalytic water splitting.[68,69]

Despite these advancements, large-scale implementations are required to overcome critical economic and environmental sustainability challenges, including material costs, natural abundance, low toxicity, and long-term stability under intense solar irradiation. To address these challenges, research efforts are currently directed toward the application of inexpensive transition metals for sustainable solar water-splitting technologies.[21]

A wide array of inorganic materials, including metal sulfides,[70,71,72] metal nitrides,[71,73,74] and transition metal oxides[71,73] have been actively investigated for photocatalytic water-splitting and H_2 production.[72] Ternary metal sulphides emerged as compelling semiconducting materials for light-driven water splitting.[72] In this regard, several research groups worked on enriching the number of sulphur sites and promoting their photocatalytic process via heterojunction structures, which improved charge separation.[70] Transition metal oxides like Fe_2O_3, although cost-effective, face several intrinsic limitations in conductivity by prompting the development of multicomponent metal oxides towards best-performing technologies.[71] Additionally, two-dimensional materials are being explored for their unique electronic and mechanical features to improve the photoelectrochemical performances of photoelectrodes.[70]

1.5.3 Biological catalysts

Enzymes play a fundamental role in living organisms, being highly efficient catalysts of essential reactions. In the field of sustainable energy conversion, enzymes and proteins naturally involved in photosynthesis, have gained significant attention due to their ability to convert light into chemical energy.[37] However, the integration of natural PS or isolated enzymes in AP electrochemical devices is very challenging.[75]

An example of a biological catalyst applied for the purpose of hydrogen production are hydrogenases, complex enzymes catalysing the reversible reduction of protons to molecular hydrogen. Hydrogenases are widely represented among microorganisms, where they couple H_2 oxidation with energy production. The enzymes of this family are classified according to their cofactors as: [Fe]-hydrogenases, [Fe–Fe]-hydrogenases, and [Ni–Fe]-hydrogenases.[76,77] Among these, the [Fe–Fe]-hydrogenases have been shown as the most effective in H_2 production. In 2006, the first system integrating a hydrogenase and the PS-I was deployed in a device capable of using light energy to produce H_2. This device was shown to perform light-driven hydrogen production at a rate of 0.58 μmol H_2 mg^{-1} chlorophyll h^{-1}, using ascorbic acid, dithiothreitol (DTT), and *N*,*N*,*N*′-tetramethyl-*p*-phenylenediamine (TMPD) as electron donors.[78,79] To improve its efficiency, the hydrogenase was directly linked to the natural

photosynthetic components, and dithiol bridges lengths were optimized to anchor the [FeFe]-hydrogenase from *C. acetobutylicum* and the PS-I. This modification enhanced the hydrogen-production efficiencies by 50 times (30.3 µmol H_2 mg^{-1} chlorophyll h^{-1} at pH 8.3) in a system using cytochrome C_6, ascorbate, and phenazine methosulphate as electron donors. The device remained active for over two months under oxygen-free conditions.[80,81]

For the counterpart reaction, Kim *et al*. were inspired by the development of metal-based biological catalysis by the water oxidation activity of iridium complexes containing imidazole-based ligands. From this observation, they explored the incorporation of iridium in bovine carbonic anhydrase (CA), whose conserved metal-anchoring site composed of three imidazole rings in the side chains of His94, His96, and His119 (Figure 1.9). The resulting Ir-CA was shown to promote water oxidation.[84]

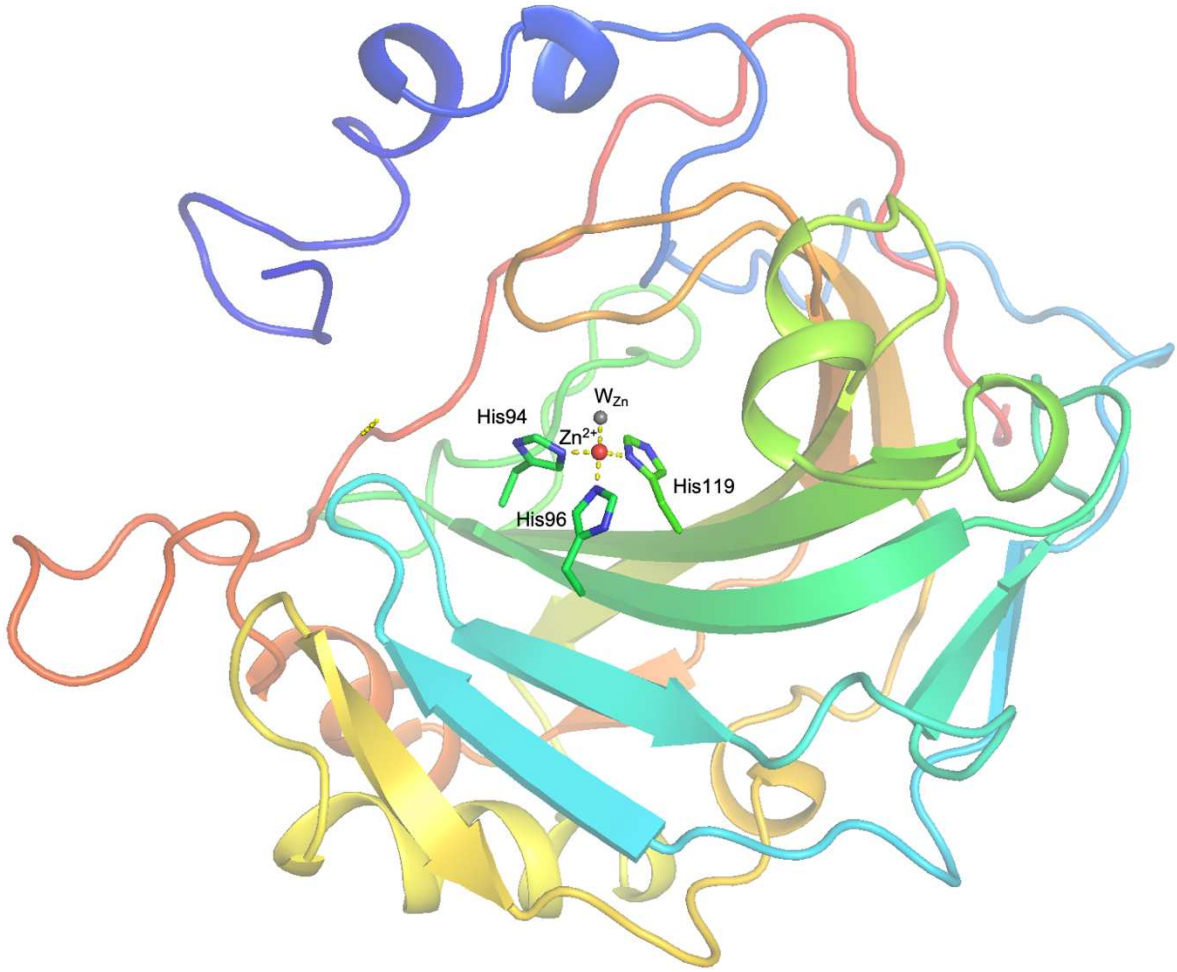

Figure 1.9: Cartoon representation of carbonic anhydrase (CA), PDB ID:2CBA.[83] The histidine residues of the catalytic centre are shown in stick, the metal ion as red spheres, and the water molecule as grey spheres.

1.6 Aim of the work

The aim of this thesis was to study the properties of a selected group of transition metal ions in relation to their binding to hCA2. In particular, my interest was driven by the Ir-substituted enzyme to be used in oxygen production, with the attempt to enhance its turnover and improve long-term stability for large-scale applications. During the three years of PhD, my research focused on the elucidation of the catalytic centre and mechanism of this enzyme from a structural and biophysical perspective. Since previous studies demonstrated that substituting the zinc cofactor with other metals can alter the catalytic activity of hCA2, modulating or abolishing its CO_2 hydration mechanism in favour of other reactions, this could open new avenues for a range of interesting applications. This research specifically focuses on the development of different metal-substituted hCA2, with particular emphasis on the Ir^{3+} substitution, which was shown to impart unique water-splitting properties to the enzyme. The present thesis is structured around three key objectives, detailed in the following chapters:

Chapter 2 - The development and structural characterization of the wild-type hCA2 protein, leading to the identification of a novel accessory Zn^{2+}-binding site in addition to the catalytic site. We developed five site-directed alanine mutants targeting histidine residues at both sites (H94A, H96A, H94A-H96A, H119A, and H4A). The wild-type protein and the mutants were characterized using isothermal titration calorimetry and X-ray crystallography, and their kinetic properties were assessed through activity assays.

Chapter 3 - The development of hCA2 substituted with transition metal divalent cations. Through detailed structural characterization, we investigated how various coordination geometries of these ions influence the catalytic activity of the enzyme. The variants described in Chapter 2 were subjected to structural studies to gain deeper insights into an accessory Cu^{2+}-binding site and their coordination chemistry.

Chapter 4 – The structural/functional study of Ir^{3+}-substituted hCA2. To confirm the binding between iridium and hCA, we conducted thermodynamic and structural studies. We also performed structural analyses on Ir^{3+}-substituted variants to assess how changes in binding sites affect this interaction. Additionally, we tested oxidative activity across all metal substitutions, confirming that iridium is uniquely capable of enhancing the production of oxygen when in conjunction with carbonic anhydrase.

1.7 References

(1) Mooney, A. Global Carbon Emissions from Fossil Fuels to Hit Record This Year.

(2) Figueres, C.; Le Quéré, C.; Mahindra, A.; Bäte, O.; Whiteman, G.; Peters, G.; Guan, D. Emissions Are Still Rising: Ramp up the Cuts. *Nature* **2018**, *564* (7734), 27–30. https://doi.org/10.1038/d41586-018-07585-6.

(3) Le Quéré, C.; Korsbakken, J. I.; Wilson, C.; Tosun, J.; Andrew, R.; Andres, R. J.; Canadell, J. G.; Jordan, A.; Peters, G. P.; Van Vuuren, D. P. Drivers of Declining CO2 Emissions in 18 Developed Economies. *Nat. Clim. Change* **2019**, *9* (3), 213–217. https://doi.org/10.1038/s41558-019-0419-7.

(4) Peters, G. P.; Andrew, R. M.; Canadell, J. G.; Friedlingstein, P.; Jackson, R. B.; Korsbakken, J. I.; Le Quéré, C.; Peregon, A. Carbon Dioxide Emissions Continue to Grow amidst Slowly Emerging Climate Policies. *Nat. Clim. Change* **2020**, *10* (1), 3–6. https://doi.org/10.1038/s41558-019-0659-6.

(5) Rocha, J.; Oliveira, S.; Viana, C. M.; Ribeiro, A. I. Chapter 8 - Climate Change and Its Impacts on Health, Environment and Economy. In *One Health*; Prata, J. C., Ribeiro, A. I., Rocha-Santos, T., Eds.; Academic Press, 2022; pp 253–279. https://doi.org/10.1016/B978-0-12-822794-7.00009-5.

(6) WMO Confirms 2024 as Warmest Year on Record at about 1.55°C above Pre-Industrial Level.Html.

(7) Global Energy Mix from 2022 to 2050 | Planète Énergies. **2022**.

(8) Lewis, N. S.; Nocera, D. G. Powering the Planet: Chemical Challenges in Solar Energy Utilization.

(9) Balzani, V.; Credi, A.; Venturi, M. Photochemical Conversion of Solar Energy. *ChemSusChem* **2008**, *1* (1–2), 26–58. https://doi.org/10.1002/cssc.200700087.

(10) Cook, T. R.; Dogutan, D. K.; Reece, S. Y.; Surendranath, Y.; Teets, T. S.; Nocera, D. G. Solar Energy Supply and Storage for the Legacy and Nonlegacy Worlds. *Chem. Rev.* **2010**, *110* (11), 6474–6502. https://doi.org/10.1021/cr100246c.

(11) Dasgupta, S.; Brunschwig, B. S.; Winkler, J. R.; Gray, H. B. Solar Fuels Editorial. *Chem. Soc. Rev.* **2013**, *42* (6), 2213. https://doi.org/10.1039/c3cs90016a.

(12) Gray, H. B. Powering the Planet with Solar Fuel. *Nat. Chem.* **2009**, *1* (1), 7–7. https://doi.org/10.1038/nchem.141.

(13) Chawla, R.; Singhal, P.; Garg, A. K. Photovoltaic Review of All Generations: Environmental Impact and Its Market Potential. *Trans. Electr. Electron. Mater.* **2020**, *21* (5), 456–476. https://doi.org/10.1007/s42341-020-00217-9.

(14) Yachandra, V. K.; DeRose, V. J.; Latimer, M. J.; Mukerji, I.; Sauer, K.; Klein, M. P. Where Plants Make Oxygen: A Structural Model for the Photosynthetic Oxygen-Evolving Manganese Cluster. *Science* **1993**, *260* (5108), 675–679. https://doi.org/10.1126/science.8480177.

(15) Dogutan, D. K.; Nocera, D. G. Artificial Photosynthesis at Efficiencies Greatly Exceeding That of Natural Photosynthesis. *Acc. Chem. Res.* **2019**, *52* (11), 3143–3148. https://doi.org/10.1021/acs.accounts.9b00380.

(16) Krewald, V.; Retegan, M.; Pantazis, D. A. Principles of Natural Photosynthesis. In *Solar Energy for Fuels*; Tüysüz, H., Chan, C. K., Eds.; Topics in Current Chemistry; Springer International Publishing: Cham, 2015; Vol. 371, pp 23–48. https://doi.org/10.1007/128_2015_645.

(17) Meyer, Y.; Buchanan, B. B.; Vignols, F.; Reichheld, J.-P. Thioredoxins and Glutaredoxins: Unifying Elements in Redox Biology. *Annu. Rev. Genet.* **2009**, *43* (1), 335–367. https://doi.org/10.1146/annurev-genet-102108-134201.

(18) Thylakoid_membrane_3.Svg.Png.

(19) Nguyen, V.-H.; Nguyen, B.-S.; Jin, Z.; Shokouhimehr, M.; Jang, H. W.; Hu, C.; Singh, P.; Raizada, P.; Peng, W.; Shiung Lam, S.; Xia, C.; Nguyen, C. C.; Kim, S. Y.; Le, Q. V. Towards Artificial Photosynthesis: Sustainable Hydrogen Utilization for Photocatalytic Reduction of CO2 to High-Value Renewable Fuels. *Chem. Eng. J.* **2020**, *402*, 126184. https://doi.org/10.1016/j.cej.2020.126184.

(20) Guan, G.; Kida, T.; Yoshida, A. Reduction of Carbon Dioxide with Water under Concentrated Sunlight Using Photocatalyst Combined with Fe-Based Catalyst. *Appl. Catal. B Environ.* **2003**, *41* (4), 387–396. https://doi.org/10.1016/S0926-3373(02)00174-1.

(21) Tachibana, Y.; Vayssieres, L.; Durrant, J. R. Artificial Photosynthesis for Solar Water-Splitting. *Nat. Photonics* **2012**, *6* (8), 511–518. https://doi.org/10.1038/nphoton.2012.175.

(22) Kärkäs, M. D.; Verho, O.; Johnston, E. V.; Åkermark, B. Artificial Photosynthesis: Molecular Systems for Catalytic Water Oxidation. *Chem. Rev.* **2014**, *114* (24), 11863–12001. https://doi.org/10.1021/cr400572f.

(23) Artificial Photosynthesis and the Splitting of Water to Generate Hydrogen. *Curr. Sci.* **2021**, *106* (4).

(24) Machín, A.; Cotto, M.; Ducongé, J.; Márquez, F. Artificial Photosynthesis: Current Advancements and Future Prospects. *Biomimetics* **2023**, *8* (3), 298. https://doi.org/10.3390/biomimetics8030298.

(25) Meyer, T. J.; Huynh, M. H. V.; Thorp, H. H. The Possible Role of Proton-Coupled Electron Transfer (PCET) in Water Oxidation by Photosystem II. *Angew. Chem. Int. Ed.* **2007**, *46* (28), 5284–5304. https://doi.org/10.1002/anie.200600917.

(26) Huynh, M. H. V.; Meyer, T. J. Proton-Coupled Electron Transfer. *Chem. Rev.* **2007**, *107* (11), 5004–5064. https://doi.org/10.1021/cr0500030.

(27) Wenger, O. S. Proton-Coupled Electron Transfer Originating from Excited States of Luminescent Transition-Metal Complexes. *Chem. – Eur. J.* **2011**, *17* (42), 11692–11702. https://doi.org/10.1002/chem.201102011.

(28) Gust, D.; Moore, T. A.; Moore, A. L. Solar Fuels via Artificial Photosynthesis. *Acc. Chem. Res.* **2009**, *42* (12), 1890–1898. https://doi.org/10.1021/ar900209b.

(29) Concepcion, J. J.; House, R. L.; Papanikolas, J. M.; Meyer, T. J. Chemical Approaches to Artificial Photosynthesis. *Proc. Natl. Acad. Sci.* **2012**, *109* (39), 15560–15564. https://doi.org/10.1073/pnas.1212254109.

(30) Fujishima, A.; Honda, K. Electrochemical Photolysis of Water at a Semiconductor Electrode. *Nature* **1972**, *238* (5358), 37–38. https://doi.org/10.1038/238037a0.

(31) Walter, M. G.; Warren, E. L.; McKone, J. R.; Boettcher, S. W.; Mi, Q.; Santori, E. A.; Lewis, N. S. Solar Water Splitting Cells. *Chem. Rev.* **2010**, *110* (11), 6446–6473. https://doi.org/10.1021/cr1002326.

(32) Maeda, K.; Higashi, M.; Lu, D.; Abe, R.; Domen, K. Efficient Nonsacrificial Water Splitting through Two-Step Photoexcitation by Visible Light Using a Modified Oxynitride as a Hydrogen Evolution Photocatalyst. *J. Am. Chem. Soc.* **2010**, *132* (16), 5858–5868. https://doi.org/10.1021/ja1009025.

(33) Abe, R. Recent Progress on Photocatalytic and Photoelectrochemical Water Splitting under Visible Light Irradiation. *J. Photochem. Photobiol. C Photochem. Rev.* **2010**, *11* (4), 179–209. https://doi.org/10.1016/j.jphotochemrev.2011.02.003.

(34) Tada, H.; Mitsui, T.; Kiyonaga, T.; Akita, T.; Tanaka, K. All-Solid-State Z-Scheme in CdS–Au–TiO2 Three-Component Nanojunction System. *Nat. Mater.* **2006**, *5* (10), 782–786. https://doi.org/10.1038/nmat1734.

(35) Sasaki, Y.; Nemoto, H.; Saito, K.; Kudo, A. Solar Water Splitting Using Powdered Photocatalysts Driven by Z-Schematic Interparticle Electron Transfer without an Electron Mediator. *J. Phys. Chem. C* **2009**, *113* (40), 17536–17542. https://doi.org/10.1021/jp907128k.

(36) Grätzel, M. Photoelectrochemical Cells. **2001**, *414*.

(37) Smith, P. T.; Nichols, E. M.; Cao, Z.; Chang, C. J. Hybrid Catalysts for Artificial Photosynthesis: Merging Approaches from Molecular, Materials, and Biological Catalysis. *Acc. Chem. Res.* **2020**, *53* (3), 575–587. https://doi.org/10.1021/acs.accounts.9b00619.

(38) Pu, Z.; Amiinu, I. S.; Cheng, R.; Wang, P.; Zhang, C.; Mu, S.; Zhao, W.; Su, F.; Zhang, G.; Liao, S.; Sun, S. Single-Atom Catalysts for Electrochemical Hydrogen Evolution Reaction: Recent Advances and Future Perspectives. *Nano-Micro Lett.* **2020**, *12* (1), 21. https://doi.org/10.1007/s40820-019-0349-y.

(39) Anjum, M. A. R.; Jeong, H. Y.; Lee, M. H.; Shin, H. S.; Lee, J. S. Efficient Hydrogen Evolution Reaction Catalysis in Alkaline Media by All-in-One MoS_2 with Multifunctional Active Sites. *Adv. Mater.* **2018**, *30* (20), 1707105. https://doi.org/10.1002/adma.201707105.

(40) Murthy, A. P.; Madhavan, J.; Murugan, K. Recent Advances in Hydrogen Evolution Reaction Catalysts on Carbon/Carbon-Based Supports in Acid Media. *J. Power Sources* **2018**, *398*, 9–26. https://doi.org/10.1016/j.jpowsour.2018.07.040.

(41) Zhu, K.; Shi, F.; Zhu, X.; Yang, W. The Roles of Oxygen Vacancies in Electrocatalytic Oxygen Evolution Reaction. *Nano Energy* **2020**, *73*, 104761. https://doi.org/10.1016/j.nanoen.2020.104761.

(42) Blakemore, J. D.; Crabtree, R. H.; Brudvig, G. W. Molecular Catalysts for Water Oxidation. *Chem. Rev.* **2015**, *115* (23), 12974–13005. https://doi.org/10.1021/acs.chemrev.5b00122.

(43) Harriman, A.; Pickering, I. J.; Thomas, J. M.; Christensen, P. A. Metal Oxides as Heterogeneous Catalysts for Oxygen Evolution under Photochemical Conditions. *J. Chem. Soc. Faraday Trans. 1 Phys. Chem. Condens. Phases* **1988**, *84* (8), 2795. https://doi.org/10.1039/f19888402795.

(44) Gersten, S. W.; Samuels, G. J.; Meyer, T. J. Catalytic Oxidation of Water by an Oxo-Bridged Ruthenium Dimer. *J. Am. Chem. Soc.* **1982**, *104* (14), 4029–4030. https://doi.org/10.1021/ja00378a053.

(45) Gilbert, J. A.; Eggleston, D. S.; Murphy Jr., W. R.; Geselowitz, D. A.; Gersten, S. W.; Hodgson, D. J.; Meyer, T. J. Structure and Redox Properties of the Water-Oxidation Catalyst [(Bpy)2(OH2)RuORu(OH2)(Bpy)2]4+. *J. Am. Chem. Soc.* **1985**, *107* (13), 3855–3864. https://doi.org/10.1021/ja00299a017.

(46) Mola, J.; Rodríguez, M.; Romero, I.; Llobet, A.; Parella, T.; Poater, A.; Duran, M.; Solà, M.; Benet-Buchholz, J. New Ru Complexes Containing the N-Tridentate Bpea and Phosphine Ligands: Consequences of Meridional vs Facial Geometry. *Inorg. Chem.* **2006**, *45* (26), 10520–10529. https://doi.org/10.1021/ic061126l.

(47) Rodríguez, M.; Romero, I.; Llobet, A.; Deronzier, A.; Biner, M.; Parella, T.; Stoeckli-Evans, H. Synthesis, Structure, and Redox and Catalytic Properties of a New Family of Ruthenium Complexes Containing the Tridentate Bpea Ligand. *Inorg. Chem.* **2001**, *40* (17), 4150–4156. https://doi.org/10.1021/ic010064q.

(48) Sens, C.; Romero, I.; Rodríguez, M.; Llobet, A.; Parella, T.; Benet-Buchholz, J. A New Ru Complex Capable of Catalytically Oxidizing Water to Molecular Dioxygen. *J. Am. Chem. Soc.* **2004**, *126* (25), 7798–7799. https://doi.org/10.1021/ja0486824.

(49) Zong, R.; Thummel, R. P. A New Family of Ru Complexes for Water Oxidation. *J. Am. Chem. Soc.* **2005**, *127* (37), 12802–12803. https://doi.org/10.1021/ja054791m.

(50) Wasylenko, D. J.; Ganesamoorthy, C.; Koivisto, B. D.; Berlinguette, C. P. Examination of Water Oxidation by Catalysts Containing Cofacial Metal Sites. *Eur. J. Inorg. Chem.* **2010**, *2010* (20), 3135–3142. https://doi.org/10.1002/ejic.201000099.

(51) Marelius, D. C.; Bhagan, S.; Charboneau, D. J.; Schroeder, K. M.; Kamdar, J. M.; McGettigan, A. R.; Freeman, B. J.; Moore, C. E.; Rheingold, A. L.; Cooksy, A. L.; Smith, D. K.; Paul, J. J.; Papish, E. T.; Grotjahn, D. B. How Do Proximal Hydroxy or Methoxy Groups on the Bidentate Ligand Affect [(2,2′;6′,2"-Terpyridine)Ru(N,N)X] Water-Oxidation Catalysts? Synthesis, Characterization, and Reactivity at Acidic and Near-Neutral pH. *Eur. J. Inorg. Chem.* **2014**, *2014* (4), 676–689. https://doi.org/10.1002/ejic.201300826.

(52) Duan, L.; Xu, Y.; Tong, L.; Sun, L. Ce^{IV} - and Light-Driven Water Oxidation by $[Ru(Terpy)(Pic)_3]^{2+}$ Analogues: Catalytic and Mechanistic Studies. *ChemSusChem* **2011**, *4* (2), 238–244. https://doi.org/10.1002/cssc.201000313.

(53) Ruettinger, W. F.; Campana, C.; Dismukes, G. C. Synthesis and Characterization of $Mn_4O_4L_6$ Complexes with Cubane-like Core Structure: A New Class of Models of the Active Site of the Photosynthetic Water Oxidase. *J. Am. Chem. Soc.* **1997**, *119* (28), 6670–6671. https://doi.org/10.1021/ja9639022.

(54) Blakemore, J. D.; Crabtree, R. H.; Brudvig, G. W. Molecular Catalysts for Water Oxidation. *Chem. Rev.* **2015**, *115* (23), 12974–13005. https://doi.org/10.1021/acs.chemrev.5b00122.

(55) Anderlund, M. F.; Högblom, J.; Shi, W.; Huang, P.; Eriksson, L.; Weihe, H.; Styring, S.; Åkermark, B.; Lomoth, R.; Magnuson, A. Redox Chemistry of a Dimanganese(II,III) Complex with an Unsymmetric Ligand: Water Binding, Deprotonation and Accumulative Light-Induced Oxidation. *Eur. J. Inorg. Chem.* **2006**, *2006* (24), 5033–5047. https://doi.org/10.1002/ejic.200600676.

(56) Naruta, Y.; Sasayama, M.; Sasaki, T. Oxygen Evolution by Oxidation of Water with Manganese Porphyrin Dimers. *Angew. Chem. Int. Ed. Engl.* **1994**, *33* (18), 1839–1841. https://doi.org/10.1002/anie.199418391.

(57) Maayan, G.; Gluz, N.; Christou, G. A Bioinspired Soluble Manganese Cluster as a Water Oxidation Electrocatalyst with Low Overpotential. *Nat. Catal.* **2017**, *1* (1), 48–54. https://doi.org/10.1038/s41929-017-0004-2.

(58) Singh, A.; Spiccia, L. Water Oxidation Catalysts Based on Abundant 1st Row Transition Metals. *Coord. Chem. Rev.* **2013**, *257* (17–18), 2607–2622. https://doi.org/10.1016/j.ccr.2013.02.027.

(59) Ellis, W. C.; McDaniel, N. D.; Bernhard, S.; Collins, T. J. Fast Water Oxidation Using Iron. *J. Am. Chem. Soc.* **2010**, *132* (32), 10990–10991. https://doi.org/10.1021/ja104766z.

(60) Abe, T.; Nagai, K.; Kabutomori, S.; Kaneko, M.; Tajiri, A.; Norimatsu, T. An Organic Photoelectrode Working in the Water Phase: Visible-Light-Induced Dioxygen Evolution by a Perylene Derivative/Cobalt Phthalocyanine Bilayer. *Angew. Chem. Int. Ed.* **2006**, *45* (17), 2778–2781. https://doi.org/10.1002/anie.200504454.

(61) Dogutan, D. K.; McGuire, R.; Nocera, D. G. Electocatalytic Water Oxidation by Cobalt(III) Hangman β-Octafluoro Corroles. *J. Am. Chem. Soc.* **2011**, *133* (24), 9178–9180. https://doi.org/10.1021/ja202138m.

(62) Nakazono, T.; Parent, A. R.; Sakai, K. Cobalt Porphyrins as Homogeneous Catalysts for Water Oxidation. *Chem. Commun.* **2013**, *49* (56), 6325. https://doi.org/10.1039/c3cc43031f.

(63) Yin, Q.; Tan, J. M.; Besson, C.; Geletii, Y. V.; Musaev, D. G.; Kuznetsov, A. E.; Luo, Z.; Hardcastle, K. I.; Hill, C. L. A Fast Soluble Carbon-Free Molecular Water Oxidation Catalyst Based on Abundant Metals. *Science* **2010**, *328* (5976), 342–345. https://doi.org/10.1126/science.1185372.

(64) Wasylenko, D. J.; Ganesamoorthy, C.; Borau-Garcia, J.; Berlinguette, C. P. Electrochemical Evidence for Catalytic Water Oxidation Mediated by a High-Valent Cobalt Complex. *Chem. Commun.* **2011**, *47* (14), 4249. https://doi.org/10.1039/c0cc05522k.

(65) McDaniel, N. D.; Coughlin, F. J.; Tinker, L. L.; Bernhard, S. Cyclometalated Iridium(III) Aquo Complexes: Efficient and Tunable Catalysts for the Homogeneous Oxidation of Water. *J. Am. Chem. Soc.* **2008**, *130* (1), 210–217. https://doi.org/10.1021/ja074478f.

(66) Hull, J. F.; Balcells, D.; Blakemore, J. D.; Incarvito, C. D.; Eisenstein, O.; Brudvig, G. W.; Crabtree, R. H. Highly Active and Robust Cp* Iridium Complexes for Catalytic Water Oxidation. *J. Am. Chem. Soc.* **2009**, *131* (25), 8730–8731. https://doi.org/10.1021/ja901270f.

(67) Shen, S.; Shi, J.; Guo, P.; Guo, L. Visible-Light-Driven Photocatalytic Water Splitting on Nanostructured Semiconducting Materials. *Int. J. Nanotechnol.* **2011**, *8* (6/7), 523. https://doi.org/10.1504/IJNT.2011.040192.

(68) Valdés, Á.; Brillet, J.; Grätzel, M.; Gudmundsdóttir, H.; Hansen, H. A.; Jónsson, H.; Klüpfel, P.; Kroes, G.-J.; Le Formal, F.; Man, I. C.; Martins, R. S.; Nørskov, J. K.; Rossmeisl, J.; Sivula, K.; Vojvodic, A.; Zäch, M. Solar Hydrogen Production with Semiconductor Metal Oxides: New Directions in Experiment and Theory. *Phys Chem Chem Phys* **2012**, *14* (1), 49–70. https://doi.org/10.1039/C1CP23212F.

(69) Kudo, A.; Miseki, Y. Heterogeneous Photocatalyst Materials for Water Splitting. *Chem Soc Rev* **2009**, *38* (1), 253–278. https://doi.org/10.1039/B800489G.

(70) Mamiyev, Z.; Balayeva, N. O. Metal Sulfide Photocatalysts for Hydrogen Generation: A Review of Recent Advances. *Catalysts* **2022**, *12* (11), 1316. https://doi.org/10.3390/catal12111316.

(71) Jafari, T.; Moharreri, E.; Amin, A.; Miao, R.; Song, W.; Suib, S. Photocatalytic Water Splitting—The Untamed Dream: A Review of Recent Advances. *Molecules* **2016**, *21* (7), 900. https://doi.org/10.3390/molecules21070900.

(72) Chong, W.-K.; Ng, B.-J.; Tan, L.-L.; Chai, S.-P. Recent Advances in Nanoscale Engineering of Ternary Metal Sulfide-Based Heterostructures for Photocatalytic Water Splitting Applications. *Energy Fuels* **2022**, *36* (8), 4250–4267. https://doi.org/10.1021/acs.energyfuels.2c00291.

(73) Inoue, Y. Photocatalytic Water Splitting by RuO2-Loaded Metal Oxides and Nitrides with D0- and D10 -Related Electronic Configurations. *Energy Environ. Sci.* **2009**, *2* (4), 364. https://doi.org/10.1039/b816677n.

(74) Nguyen, H. L. Metal–Organic Frameworks for Photocatalytic Water Splitting. *Sol. RRL* **2021**, *5* (7), 2100198. https://doi.org/10.1002/solr.202100198.

(75) Zhang, Y.; Phipps, J.; Ma, S. Artificial Enzymes for Artificial Photosynthesis. *Nat. Catal.* **2022**, *5* (11), 973–974. https://doi.org/10.1038/s41929-022-00873-5.

(76) Peters, J. W.; Schut, G. J.; Boyd, E. S.; Mulder, D. W.; Shepard, E. M.; Broderick, J. B.; King, P. W.; Adams, M. W. W. [FeFe]- and [NiFe]-Hydrogenase Diversity, Mechanism, and Maturation. *Biochim. Biophys. Acta BBA - Mol. Cell Res.* **2015**, *1853* (6), 1350–1369. https://doi.org/10.1016/j.bbamcr.2014.11.021.

(77) Fontecilla-Camps, J. C.; Volbeda, A.; Cavazza, C.; Nicolet, Y. Structure/Function Relationships of [NiFe]- and [FeFe]-Hydrogenases. *Chem. Rev.* **2007**, *107* (10), 4273–4303. https://doi.org/10.1021/cr050195z.

(78) Andreiadis, E. S.; Chavarot-Kerlidou, M.; Fontecave, M.; Artero, V. Artificial Photosynthesis: From Molecular Catalysts for Light-driven Water Splitting to Photoelectrochemical Cells. *Photochem. Photobiol.* **2011**, *87* (5), 946–964. https://doi.org/10.1111/j.1751-1097.2011.00966.x.

(79) Ihara, M.; Nishihara, H.; Yoon, K.; Lenz, O.; Friedrich, B.; Nakamoto, H.; Kojima, K.; Honma, D.; Kamachi, T.; Okura, I. Light-driven Hydrogen Production by a Hybrid Complex of a [NiFe]-Hydrogenase and the Cyanobacterial Photosystem I. *Photochem. Photobiol.* **2006**, *82* (3), 676–682. https://doi.org/10.1562/2006-01-16-RA-778.

(80) Lubner, C. E.; Knörzer, P.; Silva, P. J. N.; Vincent, K. A.; Happe, T.; Bryant, D. A.; Golbeck, J. H. Wiring an [FeFe]-Hydrogenase with Photosystem I for Light-Induced Hydrogen Production. *Biochemistry* **2010**, *49* (48), 10264–10266. https://doi.org/10.1021/bi1016167.

(81) Lubner, C. E.; Grimme, R.; Bryant, D. A.; Golbeck, J. H. Wiring Photosystem I for Direct Solar Hydrogen Production. *Biochemistry* **2010**, *49* (3), 404–414. https://doi.org/10.1021/bi901704v.

(82) Kim, M.; Lee, S. Catalytic Water Oxidation by Iridium-Modified Carbonic Anhydrase. *Chem. – Asian J.* **2018**, *13* (3), 334–341. https://doi.org/10.1002/asia.201701543.

(83) Håkansson, K.; Carlsson, M.; Svensson, L. A.; Liljas, A. Structure of Native and Apo Carbonic Anhydrase II and Structure of Some of Its Anion-Ligand Complexes. *J. Mol. Biol.* **1992**, *227* (4), 1192–1204. https://doi.org/10.1016/0022-2836(92)90531-N.

Chapter 2

Identification and characterization of an additional Zn^{2+}-binding site in hCA2

2.1 Introduction: Zinc-dependent enzymes

Zinc-dependent enzymes are a group of metalloproteins that play essential roles in various metabolic functions. They mediate catalytic processes or contribute to maintaining the structure and activity of proteins. Zinc is a crucial element found in over 300 enzymes from all six fundamental classes defined by the International Union of Biochemistry. These include oxidoreductases (*i.e.,* alcohol dehydrogenase and superoxide dismutase), transferases (*e.g.* RNA polymerase and aspartate transcarboxylase), hydrolases (*e.g.,* carboxypeptidase A and thermolysin), lyases (*e.g.,* carbonic anhydrase and fructose-1,6-bisphosphate aldolase), and isomerases (*e.g.,* phosphomannose isomerase).[1]

2.1.1 Overview of Zn^{2+}-based sites with hydrolase activity

Zinc is a metal cofactor with high electron affinity, making it ideal for reactions that require a redox-stable ion acting as a Lewis acid-type catalyst. Its divalent ion Zn^{2+} has a full *d* electron shell (d^{10} configuration), which results in low ligand stabilization energy.[2]

Among the possible coordination geometries, Zn^{2+} is mainly found in tetrahedral and octahedral configurations.[3] Zinc ions can promote acid-base catalysis in hydrolytic reactions by coordinating a nucleophilic water molecule thereby decreasing its *pKa* (Zn-OH mechanism). Alternatively, they can coordinate a carbonyl or phosphate group of a substrate, polarizing it and allowing the nucleophilic attack (Zn-carbonyl mechanism).[4]

Some Zn^{2}-dependent enzymes display co-catalytic sites, within which two or more metal ions (at least one being Zn) are located close to each other and share at least one common ligand (water molecule or a bridging carboxylate group).[4] In some cases, the ligand also plays an important role in the catalytic activity of the enzyme. Examples of enzymes belonging to this group are alkaline phosphatase (two Zn^{2+} and one Mg^{2+}), phospholipase C and nuclease P1 (three Zn^{2+}), and leucine aminopeptidase (two Zn^{2+}).[5]

A typical catalytic Zn^{2+} coordination site consists of at least one water molecule and three coordinating amino-acids, usually His, and to a lesser extent Asp and Glu.[6] This coordination is required to hold Zn^{2+} in place to mediate the deprotonation of the catalytic water, and to position the resulting OH^{-} for the subsequent nucleophilic attack a carbonyl group (Figure 2.1). An additional role is that of electrophilic catalysts, which can stabilize negative charges within the transition states.[7]

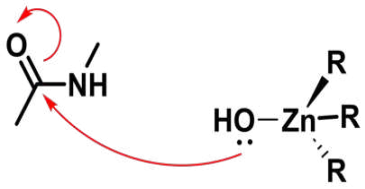

Figure 2.1: Zn-hydroxide hydrolysis mechanism.

2.1.2 Carbonic anhydrase (CA)

Carbonic anhydrases (CA, EC 4.2.1.1) are ubiquitous metalloenzymes which catalyse the reversible Zn^{2+}-dependent hydrolysis of carbon dioxide (CO_2) to bicarbonate (HCO_3^-) and H^+. A form of human CA was first isolated from erythrocytes in 1933.[7] Since then, eight distinct carbonic anhydrase families (α-, β-, γ-, δ-, ζ-,η- θ, and ι) have been identified across *Archaea*, bacteria, and eukaryotes.[8,9,10] They group non-homologous but isofunctional enzymes, which developed in different biological contexts while catalysing the same CO_2 hydration reaction.[8,11] The members of the α-CAs are the most studied and have been identified in vertebrates,[12] protozoa,[13] algae,[14] and in the cytoplasm of green plants,[15] and Gram-negative bacteria.[16] The β-CAs are present in Gram-negative and Gram-positive bacteria,[16] algae,[15] chloroplasts,[15] fungi,[17] and *Archaea.*[18] The γ-CAs are found in *Archaea*, cyanobacteria, and various other bacteria.[19] The δ-, ζ-, θ-, and ι-CAs are present only in marine diatoms,[19] while the η-CAs are found in protozoa.[20]

Given the biological relevance of the reaction catalysed, CAs are crucial in several physiological processes, including pH regulation and fluid balance across different body regions.[8] They are involved in the transport and respiration of carbon dioxide and bicarbonate, as well as in various biosynthetic reactions such as gluconeogenesis, lipogenesis, and ureagenesis.[21] Additionally, CAs contribute to bone resorption, calcification, tumorigenesis, and many other physiological and pathological processes.[21,22,23]

2.1.3 Human Carbonic anhydrase II (hCA2)

In humans, the class of α-CAs includes 14 isozymes (hCA I–XIV) with peculiar catalytic activities and localization.[24,25] Among those, human carbonic anhydrase II (hCA2) is the most studied isoform. hCA2 is a single-domain globular protein, constituted by twisted β-sheet core surrounded by α-helical structures.[26] The active site is a conical cavity, approximately 15 Å deep, which binds a Zn^{2+} in its innermost region. The Zn^{2+} essential cofactor is anchored to the

enzyme by three histidines (His94, His96, and His119) which guarantee the correct alignment through a system of H-bonded moieties (Gln92 Asn243, and Glu117).[27]

The fourth position in the tetrahedral coordination system is occupied by a water molecule (conventionally identified as "Water Zn" or "W_{Zn}"). This constitutes the catalytic water, which is deprotonated upon binding to Zn^{2+}. The leaving proton is transferred via a chain of water molecules (W1 and W2) connected to a flexible His64 sidechain. The activated OH^- is ready to perform the nucleophilic attack on the substrate (Figure 2.2).

Two main areas characterize the hCA2 active site: a hydrophobic region (Ile91, Val121, Phe131, Val135, Leu141, Val143, Leu198, Pro202, Leu204, Val207, and Trp209) and the hydrolytic side (Asp62, His64, Asp67, Gln92, Thr199, and Thr200). The former stabilises the binding of the CO_2 substrate,[27] while the latter contributes to the formation of a network of water molecules to ensure a rapid catalytic turnover.[28] Former studies on hCA2 showed that the hydroxyl group of Thr199 establishes a hydrogen bond with the hydroxide anion coordinated to Zn^{2+}, stabilizing the activated nucleophile and promoting the catalysis.[29,30]

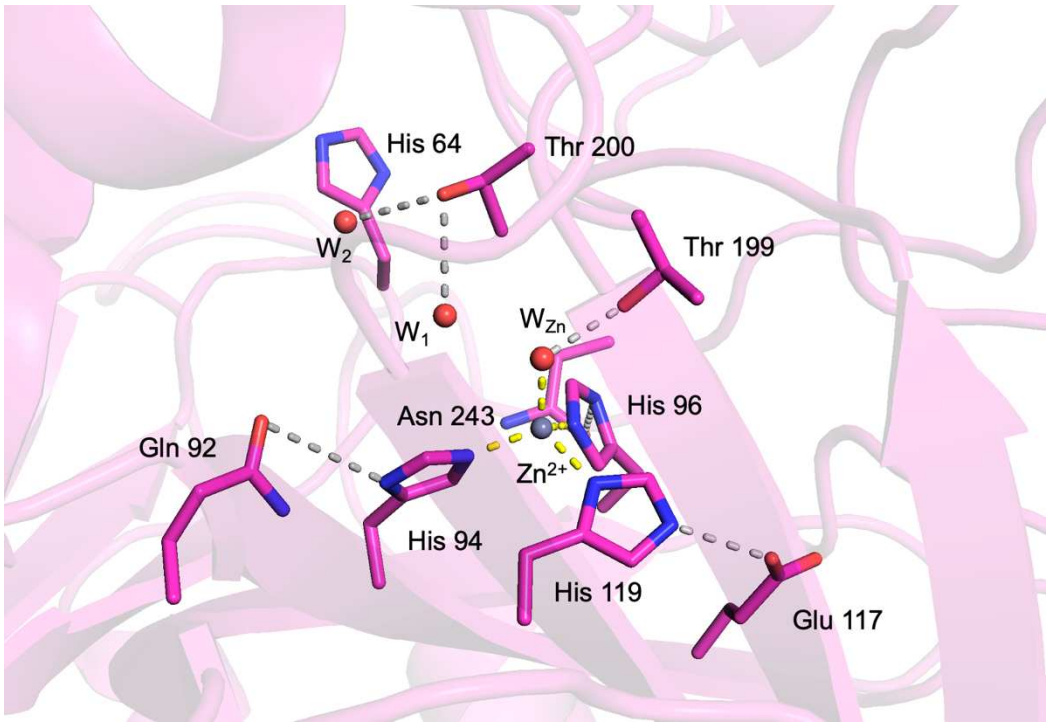

Figure 2.2: Active site of human carbonic anhydrase II. The interacting residues are shown in stick representation, with the two zinc ions depicted as grey spheres and the key water molecules represented as red spheres. Coordination bonds are illustrated as yellow dashed lines and the hydrogen bond in grey.

The proposed catalytic mechanism of hCA2 is described by two-step ping-pong reaction.[21] The first stage sees the hydroxyl nucleophile performing a nucleophilic attack the CO_2 substrate. The Zn^{2+}-bicarbonate complex is then displaced by a water molecule (W_{dw}), to release the

bicarbonate reaction product and regenerate the Zn^{2+}/water couple. In this process, the bicarbonate engages an H-bond with Thr199, thus weakening the interaction with the Zn^{2+} and promoting the rapid product dissociation.[31]

The other crucial amino acid is His64, usually referred to as the proton shuttle, since it regulates the proton transfer through W1 and W2. Former structural studies performed at different pHs revealed that His64 can occupy two alternate conformations: 'in' (pointing toward the metal centre) and 'out' (directed to the solvent exposed surface). These two orientations are associated to distinct functional states of the enzyme: while in the His64-in takes a proton from W2 molecule, it then flips to His64-out to release the proton to the bulk solvent[32,33] (Figure 2.3). Functional studies have demonstrated the pivotal role of His64 in maintaining a high catalytic efficiency.[34,35]

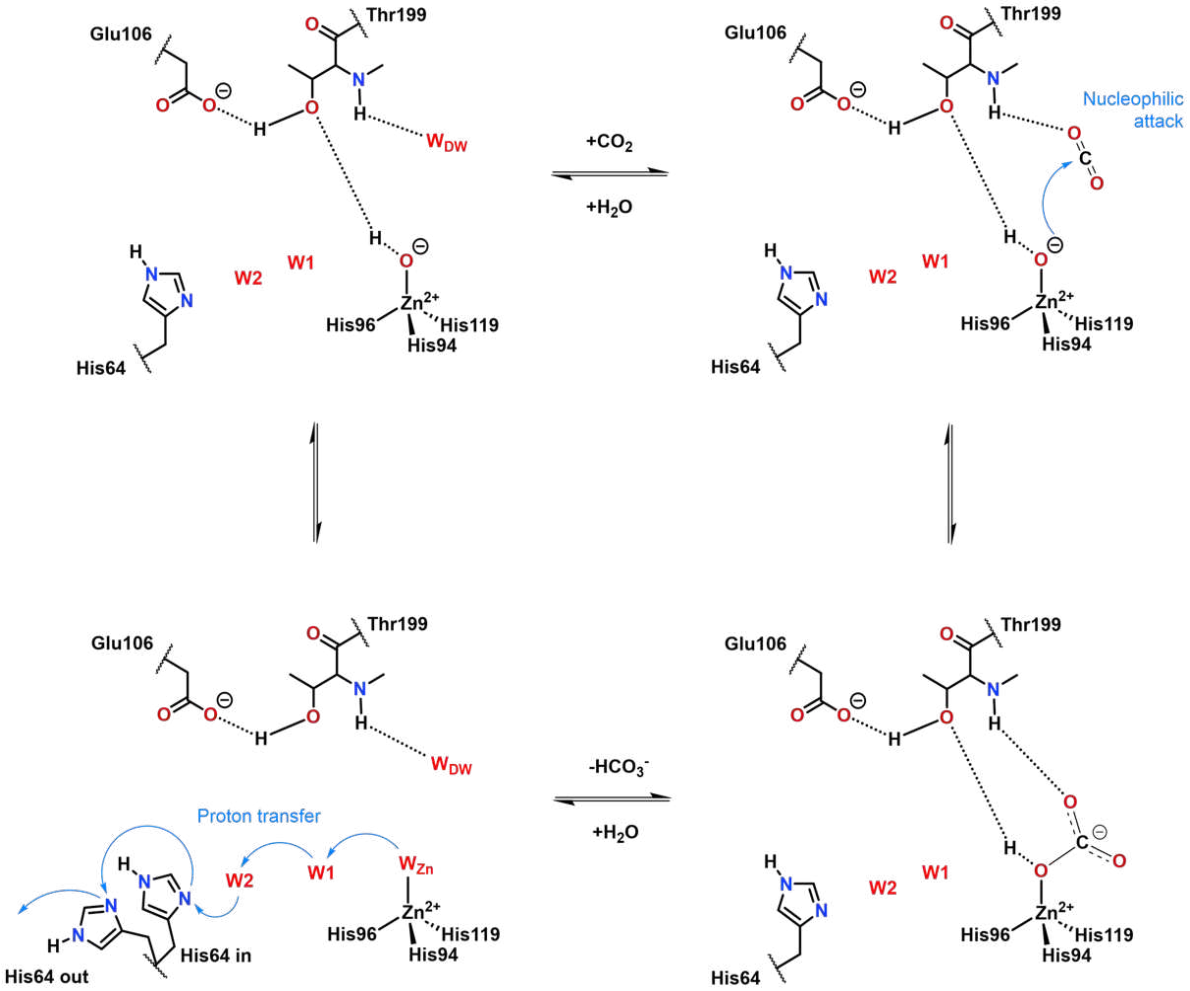

Figure 2.3: The catalytic mechanism of hCA. Reproduced from ref.[31]

2.2 Material and methods

2.2.1 Molecular cloning and site-direct mutagenesis

The synthetic gene encoding for hCA2 (residues 1-260), optimized for Escherichia coli expression, was purchased from GenScript (Piscataway, NJ). The target gene was cloned in the pET28a(+) vector between the *NdeI* and *XhoI* restriction sites (Figure 2.4). The vector also encodes for a TEV-cleavable exa-histidine-tag (His^6-tag) fused at the N-terminal of hCA2 (HT-hCA2).

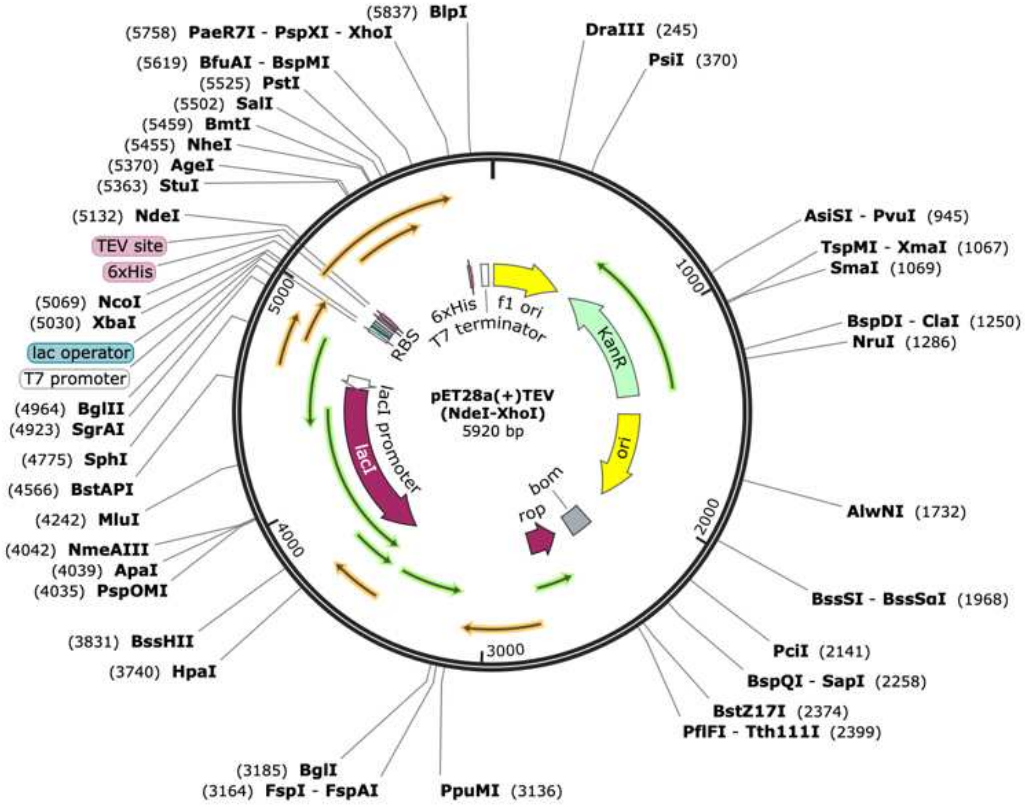

Figure 2.4: Map of pET-28a(+)-hCA2 expression plasmid (5920bp) showing its main features, including the coding regions for hCA2 (preceded by the His^6-tag and the TEV site) and the kanamycin resistance (KanR). Restriction sites (with their positions in parenthesis) are also displayed.

The pET-28a(+)-hCA2 plasmid was used as a template for the generation of five alanine mutants, namely the single variants H4A, H94A, H96A, and H119A, and the double variant H94A-H96A. All mutants were obtained by site-directed mutagenesis using partially overlapping primers (Table 2.1), and the AccuPrime Taq DNA Polymerase (High Fidelity polymerase from Thermo Fisher Scientific). The polymerase chain reaction (PCR) mixture (50 µL) consisted of template DNA (pET-28a(+)-hCA2 plasmid, 1 µL), the primer pair (2 µl), AccuPrime Taq DNA Polymerase (1 unit), and the AccuPrime PCR Buffer I. The reaction

protocol relied on an initial denaturation step (94 °C, 5 minutes), followed by 25 cycles of denaturation (94 °C, 2 minutes), annealing (55 °C, 30 seconds), and extension (68 °C, 6 minutes). Afterward, 10 µL of the reaction products were incubated with 1 µL of Fast Digest DpnI (Thermo Fisher Scientific) for 1 hour at 37 °C and then used to heat-shock transform E. coli TOP10 cells. Positive transformants were selected on LB-Agar plates supplemented with kanamycin (50 mg L^{-1}) and then cultured overnight in LB medium (supplemented with the same antibiotic) at 37 °C, under vigorous aeration (220 rpm). The plasmids were extracted using the E.Z.N.A.® DNA extraction Kit I (Omega Bio-Tek), and the mutagenesis confirmed by DNA sequencing (Eurofins Genomics).

Primers	Sequence (5'→ 3')	Mutation(s)
Fw:H4A	CACAC**GCG**TGGGGATATGGGAAAC	H4A
Rv:H4A	CCCCA**CGC**GTGTGACATCATATG	
Fw:H94A	CAGTTT**GCC**TTCCACTGGGGTTC	H94A
Rv:H94A	GGAAG**GCA**AACTGAATCAGTC	
Fw:H96A	CACTTC**GCC**TGGGGTTCTTTGG	H96A
Rv:H96A	CCCCAG**GCG**AAGTGAAACTG	
Fw:H119A	GAACT**GGC**CCTGGTTCATTGG	H119A
Rv:H119A	CCAGG**GCC**AGTTCGGCAGCGTAC	
Fw:H94-96A	CAGTTT**GCC**TTC**GCC**TGGGGTTCTTTGG	H94A-H96A
Rv:H94-96A	CCCCAG**GCG**AAG**GCA**AACTGAATCAGTC	

Table 2.1: Partial overlapping forward and reverse primers for generating the H4A, H94A, H96A, H119A and, H94A-H96A mutants.

2.2.2 Protein expression and purification

The pET-28a(+)-hCA2 expression plasmid was introduced by thermal shock in chemically competent *E. Coli* BL21(DE3) cells and positive transformants were selected on LB-agar plates added by kanamycin (50 mg L^{-1}). The target protein was produced in *E. Coli* BL21(DE3) bacterial cells by testing a small set of expression conditions, combining different culture media (ZYP-5052, SB, LB), incubation temperatures, and times (24, 48 hours). Then, bacterial cells were cultured in 6 L of ZYP-5052 auto-induction medium,[36] supplemented with kanamycin (50 mg L^{-1}), at 20 °C for 48 hours, under vigorous aeration (220 rpm). Cells, harvested by centrifugation (3500 x g, 15 min, 8 °C), were resuspended in 25 mL of buffer A (50 mM potassium phosphate pH 7.4) for 0.5 L, supplemented with lysozyme (0.5 mg mL^{-1}), and

disrupted by sonication after 1-hour incubation on ice. The lysed cell supernatant, separated by centrifugation (12000 xg, 60 min, 8°C), was purified using nickel affinity chromatography (HisTrap FF 5 mL column, GE Healthcare). The protein was purified by a three step-gradient protocol, relying on imidazole concentrations of 50 mM, 250 mM, and 500 mM (in buffer A). Fractions containing the target protein were identified by SDS PAGE analysis (NuPAGE 4-12% Bis-Tris protein gels; Thermo Fisher Scientific), pooled and dialyzed overnight in buffer A (membrane MW-cutoff 10 kDa). The His6-tag removal was performed during the dialysis by adding the HT-TEV protease (0.05 mg/mg target protein), supplemented with 2 mM DTT, directly in the membrane. Subsequently, a second stage of affinity chromatography was performed to separate the mature protein from the protease and the residual uncleaved HT-hCA2. The zinc removal to produce the apo- hCA2 was performed by chelation with pyridine-2,6-dicarboxylic acid (100 mM) in buffer A for 2 hours at 8°C.[36] The apo-hCA2 was concentrated using a centrifugal concentrator (Vivaspin 20, MW cutoff 10 kDa, Sartorius) and then purified by size-exclusion chromatography on a HiLoad 16/600 Superdex 75 pg column (GE Healthcare), using 50 mM TRIS, pH 7.8 as elution buffer. Protein purity was verified by SDS-PAGE analysis (NuPAGE 4-12% Bis-Tris protein gels; Thermo Fisher Scientific) and MALDI-TOF mass spectrometry (Toscana Life Sciences, Siena, Italy). The variants were purified following the same procedures described for the wild-type enzyme. All proteins were concentrated to final concentrations of 11 mg mL^{-1} (H4A) 20 mg mL^{-1} (H94A) 19 mg mL^{-1} (H96A) 16 mg mL^{-1} (H119A) 10 mg mL^{-1} (H94A-H96A) using centrifugal concentrators (Vivaspin 6, MW cutoff 10 kDa, Sartorius) and stored at -80 °C until required.

2.2.3 Differential scanning fluorimetry (DSF) optimization

To perform DSF assays, 10 µl of the Durham pH and salt screens were transferred into a 96-well PCR plate. Subsequently, 10 µl of a mixture containing 4 µl of 5,000X SYPRO Orange in DMSO and 1 ml of purified apo-hCA2 and Zn-hCA2 (1 mg ml^{-1}) were added to each well. The PCR plates were sealed with Optical-Adhesive Covers (biosystems) and heated in a Stratagene Mx3005P RT-QPCR system (Agilent Technologies, La Jolla, CA, USA), with a linear temperature gradient from 25 °C to 95 °C using 1°C step increments. The excitation and emission wavelengths for SYPRO Orange were set to 517 nm and 538 nm, respectively. The data was analysed using the MxPro version 4.10 QPCR software and the melting temperature (Tm) was derived from the experimental curve.

2.2.4 Isothermal titration calorimetry (ITC) analysis

ITC experiments were conducted on a MicroCal VP-ITC calorimeter at 25°C. The concentration of apo-hCA2 was determined by UV absorption at 280 nm (ε_{280} = 52,300 M^{-1} cm^{-1}). The experiment involved titrating apo-hCA2 (300 µl, 110 µM) with a 1.10 mM solution of zinc acetate. The alanine variants were also 110 µM, but the titrating Zn^{2+} salt chosen was zinc chloride 2.20 mM to optimize the response of the instrument. The solutions were all buffered in 25 mM MOPS pH 7.4. The titration was performed with 17 injections, each with 2.4 µl volume in 4.8 s followed by 150 s re-equilibration time after each step. Control runs were performed for each assay by titrating metal in the buffer (25 mM MOPS pH 7.4) and used for background subtraction. ITC data were analysed using the MicroCal Origin software and used to obtain best-fit values for the stoichiometry (n), enthalpy (ΔH), and dissociation constant (K_d). Each experiment was performed in duplicate, and the best results are reported here.

2.2.5 Protein crystallization

Apo-hCA2 crystals were grown using the sitting drop vapor-diffusion method at 20 °C in a Swissci MRC3 (RCAH) plate. Drops containing three different proteins precipitant ratios (1:1, 2:1 and 1:2) were automatically dispensed using the Mosquito robot (STP Labtech). Crystallization of apo-hCA2 was optimized by testing different protein concentrations (3-10 mg/ml) and precipitant solutions, either 1-1.6 M sodium citrate tribasic dihydrate, 50 mM TRIS pH 7.8 [24,26], or 2-3 M ammonium sulphate,[37] 50 mM TRIS pH 7.8. Crystal growth was monitored over the following days using the Formulatrix automatic imager. For apo-hCA2 and its alanine-mutants, crystals suitable for diffraction were obtained in drops prepared by mixing equal volumes (2 µl) of protein (10 mg ml^{-1}) and precipitant (1.4–1.5 M sodium citrate tribasic dihydrate, 50 mM TRIS pH 7.8) solutions, equilibrated over a 200 µL reservoir. The same conditions were also used to crystallize the holo-enzyme, obtained by exposing the apo protein to five equivalents of Zn^{2+} ions. The holo-enzyme state was also characterized through soaking experiments, by adding 1 µl of a 10 mM $ZnCl_2$ solution to the drops containing preformed apo-enzyme crystals and incubating them for 1-2 hours at room temperature. Before flash-freezing in liquid nitrogen, the crystals were washed in the cryoprotectant solution, consisting of 20% glycerol added to the precipitant solution.

2.2.6 X-ray data collection, structure solution, and refinement

X-ray diffraction data were collected at 100 K, using synchrotron radiation at the Diamond Light Source (DLS, Didcot, UK) beamline I04, equipped with an Eiger 2X 16M, the European Synchrotron Radiation Facility (ESRF, Grenoble, France) beamline ID30B on an EIGER2 9M detector, and the Petra III (Hamburg, Germany) beamline P13 on an EIGER 16M detector. Data were integrated with XDS[38] and scaled using AIMLESS[39] from the CCP4i2 suite.[40] Data collection and reduction statistics are shown in Table 2.3-2.6-2.7. The crystals of hCA2 and its variants belong to the monoclinic space group $P2_1$. The structures were solved by molecular replacement with Molrep[41], using the structure of hCA2 (PDB code 2CBA)[37] as the search model (metal ions and water molecules were preventively removed). The structures were refined using REFMAC[42] from the CCP4i2 suite. The molecular graphic software Coot[43] was used for visual inspection and manual modelling of the structures and to add water molecules. To demonstrate the presence of Zn^{2+} ions in the structures of holo-hCA2 and its mutants, MAD collections were performed at three wavelengths (remote high energy, 13000-13500 eV, and above and immediately before the Zn K-edge, 7750 eV and 7550 eV, respectively). The positions of Zn^{2+} ions were determined by calculating the anomalous difference Fourier maps from the data collected at 7750 eV and 7550 eV, using the program FFT from the CCP4 suite.[44] Anomalous signals ranging between 5 and 30 σ were detected in all structures. The occupancies of Zn^{2+} ions were adjusted to keep their atomic displacement parameters close to those of nearby protein atoms in fully occupied sites. Final structural models were validated and checked with the software Molprobity.[45] Data collection and processing and structure refinement statistics are reported in Tables 2.3-2.6-2.7. Figures were prepared using the molecular graphics software PyMol.[46]

2.2.7 Esterase kinetic assays

Esterase kinetic assays were performed on wild type hCA2 and the alanine variants. The conversion of 4-nitrophenyl acetate (4-NPA) to 4-nitrophenol (4-NP) mediated by the esterase catalytic activity of hCA2 was evaluated spectrophotometrically (UV-visible spectro-photometer mySPEC, VWR, version 2.1.0.0). The 4-NPA is hydrolysed by hCA2 producing 4-NP (ε_{400} = 18 400 M^{-1} cm^{-1}),[47,48] a compound that exhibits strong absorbance at 348-400 nm in the UV-visible spectrum.[31,49] Reaction mixtures made of 1 mL assay buffer (2.4 mM 4-NPA, 3% acetone, 10 mM TRIS pH 7.8) and 0.2 mL of the enzyme. Reactions were performed at

room temperature by monitoring at 400 nm for 2 min (data pitch of 10 seconds). Initial reaction rates were measured on the apo and holo-states of hCA2 and its variants, using 2.4 mM 4-NPA and 0.02 mg ml^{-1} enzyme (and its variants). The holo-state of hCA2 and its variants were obtained by incubating the enzyme solution with five equivalents of Zn^{2+} ions for one hour.
For *km* determination, the substrate concentration varied in the range of 0.1-2.4 mM, keeping an enzyme concentration of 0.1 mg ml^{-1}. Instead, for k_{cat} determination, the 4-NPA concentration was kept fixed at 2.4 mM and the enzyme concentration was varied in the range of 0.012-0.005 mg ml^{-1}. All kinetic assays were performed in duplicate.

2.3 Results and Discussion

2.3.1 Expression and purification of hCA2

For the production of recombinant hCA2, we acquired the pET-28a(+)-hCA2 expression plasmid purchased from GenScript. The plasmid includes the gene coding sequence for hCA2 optimized for *E. coli* expression, cloned within the *NdeI* and *XhoI* restriction sites, in-frame with the TEV-cleavable His^6-tag, allowing the production of His^6-tag hCA2 (HT-hCA2). The target protein was produced in *E. coli* BL21(DE3) bacterial cells by testing a small set of expression conditions, combining different culture media (ZYP-5052, SB, LB), incubation temperatures and times (24, 48 hours). Although hCA2 is readily expressed in the soluble cellular fraction under various conditions, the best turned out to be by culturing bacterial cells in ZYP-5052 autoinduction medium at 20 °C for 48 hours (Figure 2.5).

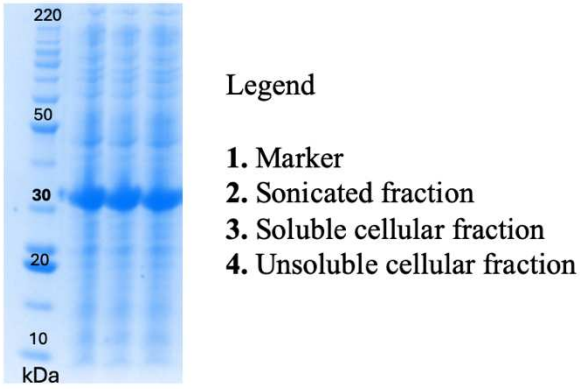

Figure 2.5: SDS-PAGE Analysis of hCA2 Expression in ZYP-5052 Medium ($MW_{HT\text{-}hCA2}$: 31782 Da).

The purification procedures took advantage of the N-terminal His^6-tag, leading to the obtainment of almost pure protein samples after a single stage of immobilized metal-affinity chromatography (IMAC), performed by means of HisTrap column. The purification protocol relied on a three-step gradient with increasing imidazole concentrations. HT-hCA2 was eluted from the matrix by applying a 250 mM imidazole concentration, as indicated by the purification chromatogram (UV_{280nm} monitoring) and the subsequent SDS-PAGE analysis of the separated fractions (Figure 2.6).

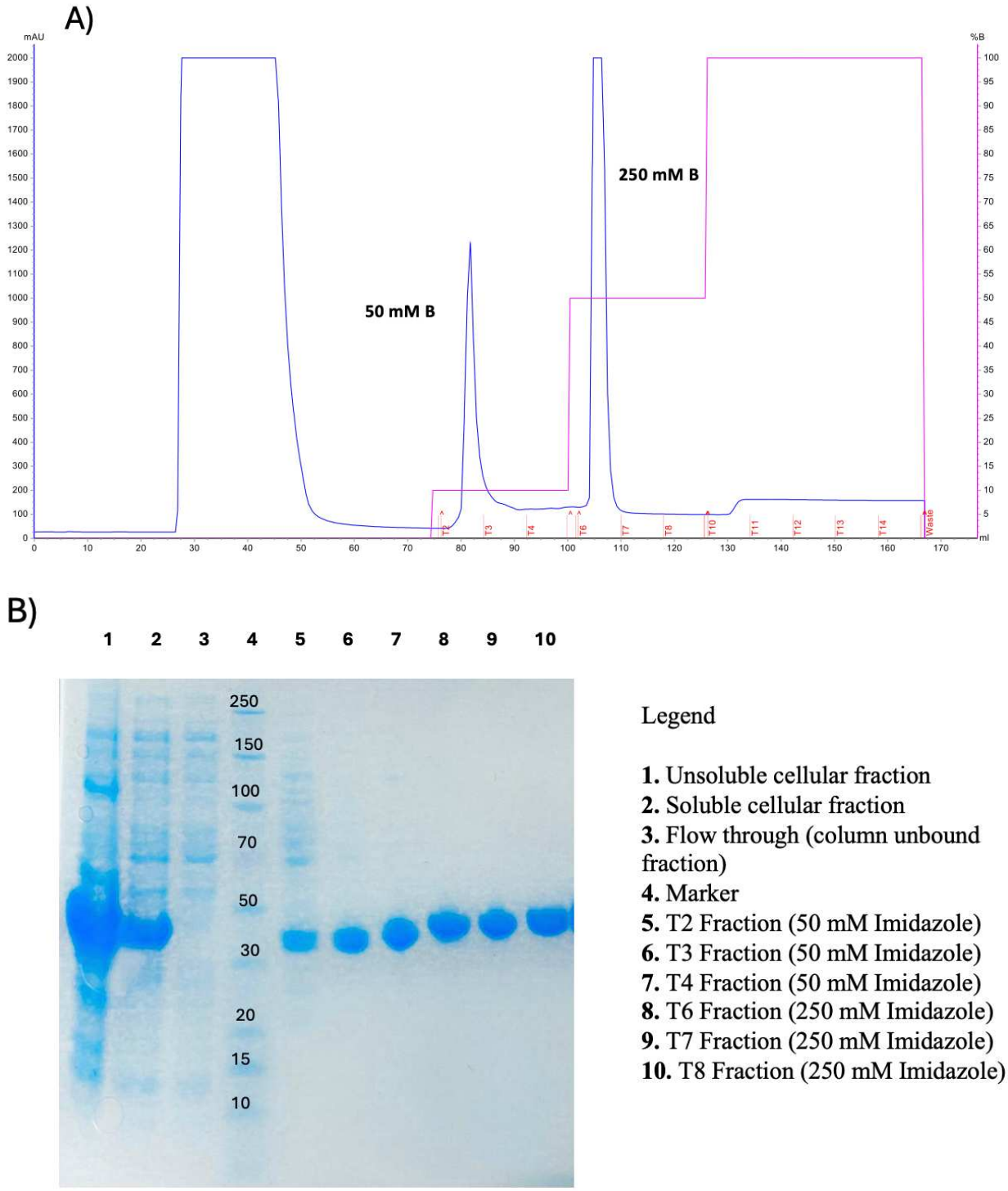

Figure 2.6: (A) HT-hCA2 purification chromatogram obtained by the HisTrap FF 5 mL column (GE Healthcare). The monitoring of the UV absorbance at 280 nm is shown as a blue line, while the imidazole concentration is in magenta. The eluted fractions are indicated on the x-axis by red marks. (B) SDS-PAGE analysis of the fractions collected from affinity chromatography ($MW_{HT\text{-}hCA2}$:31782 Da).

After the proteolytic cleavage of the histidine tail by the HT-TEV protease, a second stage of affinity chromatography was performed to separate the mature protein from the protease and any residual HT-hCA2 (Figure 2.7). As shown by the chromatogram and the following

SDS-PAGE analysis of the separated fractions, the mature hCA2 binds weakly to the column, eluting at a 40 mM imidazole concentration.

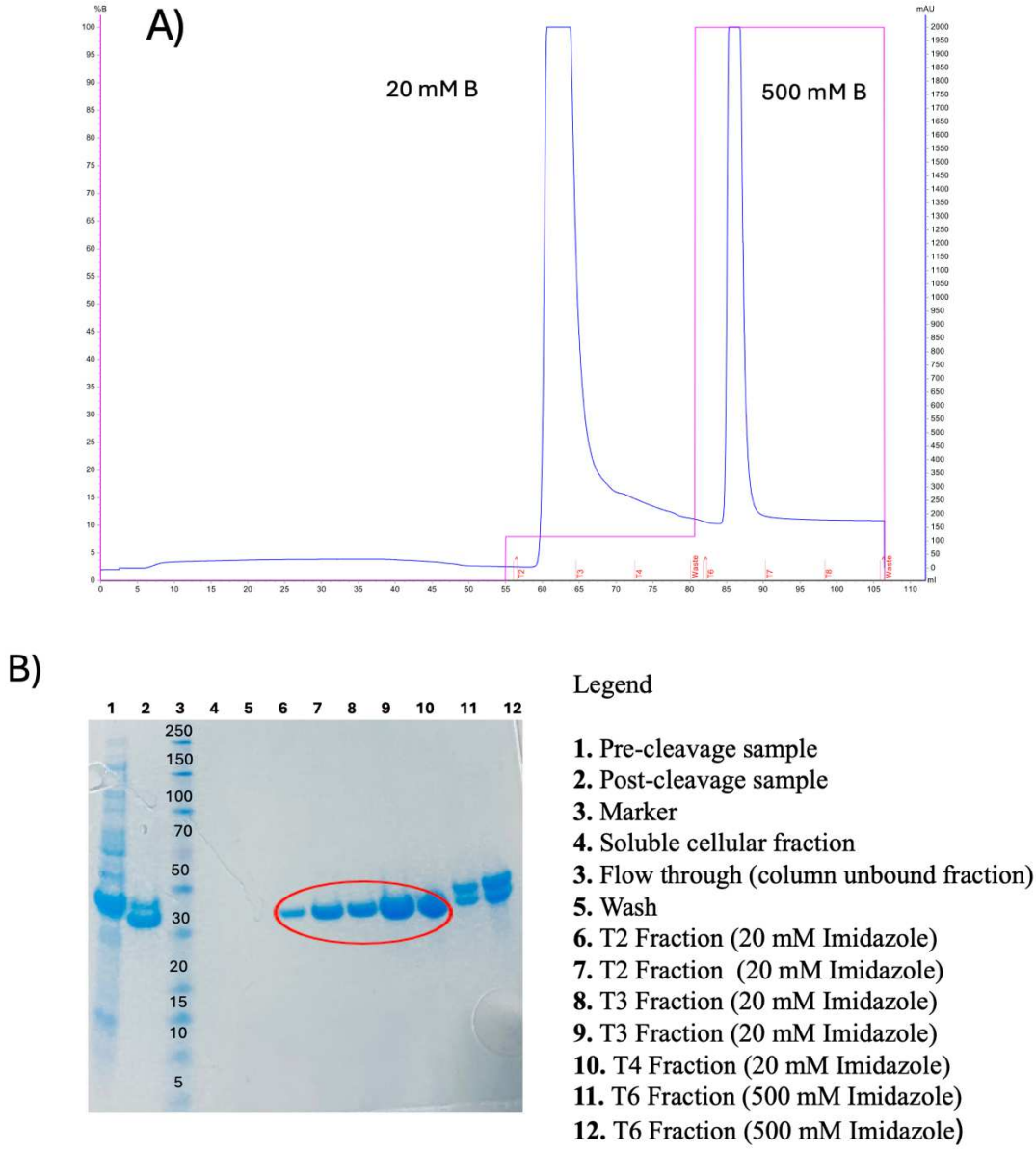

Figure 2.7: (A) Chromatogram of mature-hCA2.The UV absorbance at 280$_{nm}$ is shown as a blue line, while the step-gradient concentration of imidazole is represented in purple. Elution fractions are indicated on the x-axis by red marks. (B) SDS-PAGE analysis of the fractions collected from reverse affinity chromatography (MW$_{HT\text{-}hCA2}$: 31782 Da, MW$_{hCA2}$: 29571 Da).

The mature protein was then subjected to Zn^{2+} removal, using pyridine-2,6-dicarboxylic acid (100 mM) as chelating agent.[32] The apo-protein was then purified by size exclusion chromatography using a HiLoad 16/600 Superdex 75pg column (Figure 2.8 A). The high-purity of the final sample was confirmed by SDS-PAGE analysis (Figure 2.8 B) and MALDI-TOF

mass-spectrometry (hCA2: theoretical MW: 29571.4 Da, determined MW: 29611.9 Da; Figure 2.9).

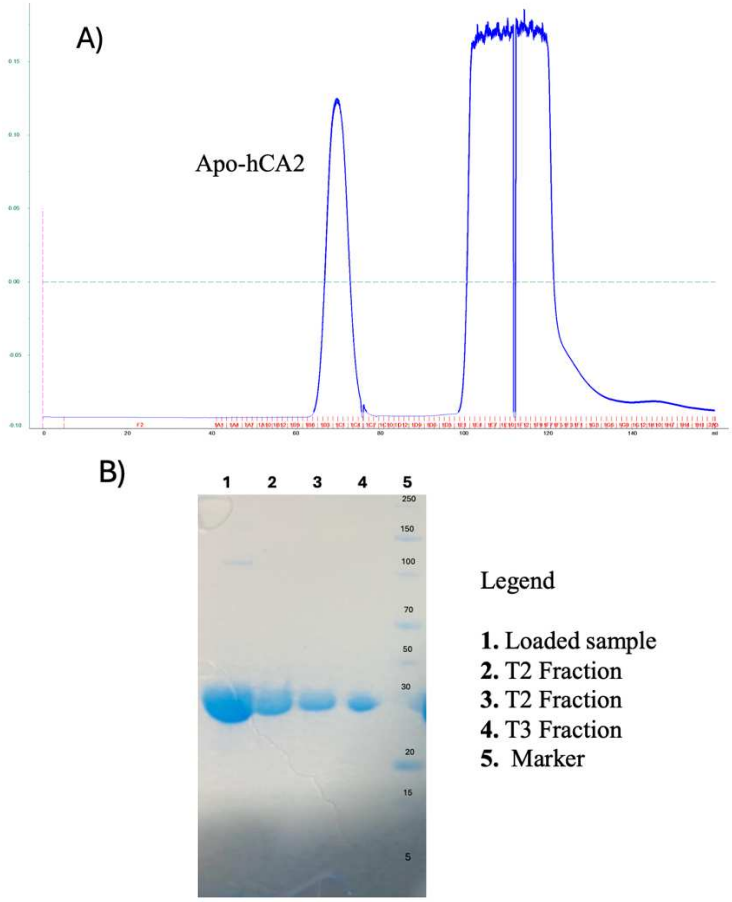

Figure 2.8. (A) Gel filtration chromatogram of protein purification using a HiLoad 16/600 Superdex 75 pg column (GE Healthcare). The UV absorbance at 280 $_{nm}$ is shown as a blue line. Elution fractions are indicated on the x-axis by red marks. (B) SDS-PAGE analysis of the fractions collected from size-exclusion chromatography (SEC).

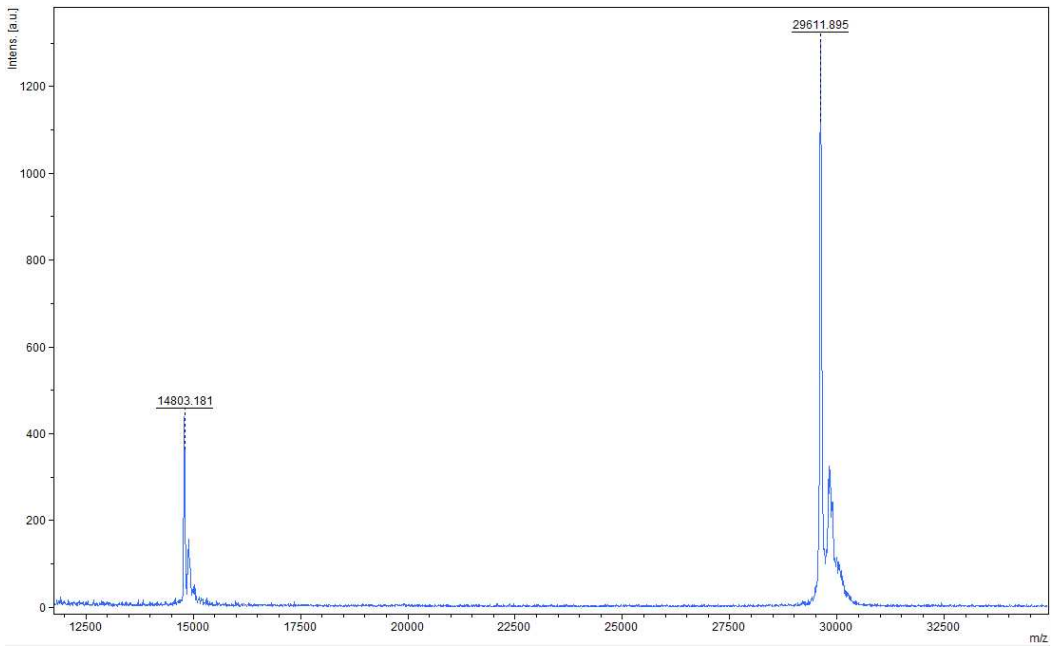

Figure 2.9: MALDI-TOF mass spectrum of mature hCA2 (theoretical MW: 29571.4 Da, determined MW: 29611.9 Da).

2.3.2 hCA2 Characterization: thermal stability and binding assays

Differential scanning fluorimetry (DSF, also known as "Thermofluor"), was used to describe the thermal stability profile of hCA2. Two screens, the Durham pH and the Durham Salt Screen, were employed to rapidly evaluate how buffers (compositions and pHs) and salts (types and concentrations) respectively, affect different biophysical properties (e.g., solubility, isothermal stability, and thermal denaturation point) of a target protein. The results of the Durham pH Screen performed on the apo and holo-hCA2 (Figures 2.10 and 2.11, respectively), showed that the enzyme is more stable under neutral-alkaline conditions (specifically with 0.1M ADA pH 6.1, 0.1 M phosphate, pH 6.3, 0.1 M citric acid, pH 6.5, 0.1 M bicine, pH 7.7, 0.1 M tricine, pH 8.0,and 0.1 M glycine, pH 9.2). The profiles recorded on both states of the protein highlight the increased stability of the holo-enzyme, characterized by higher-temperature melting point (Tm).

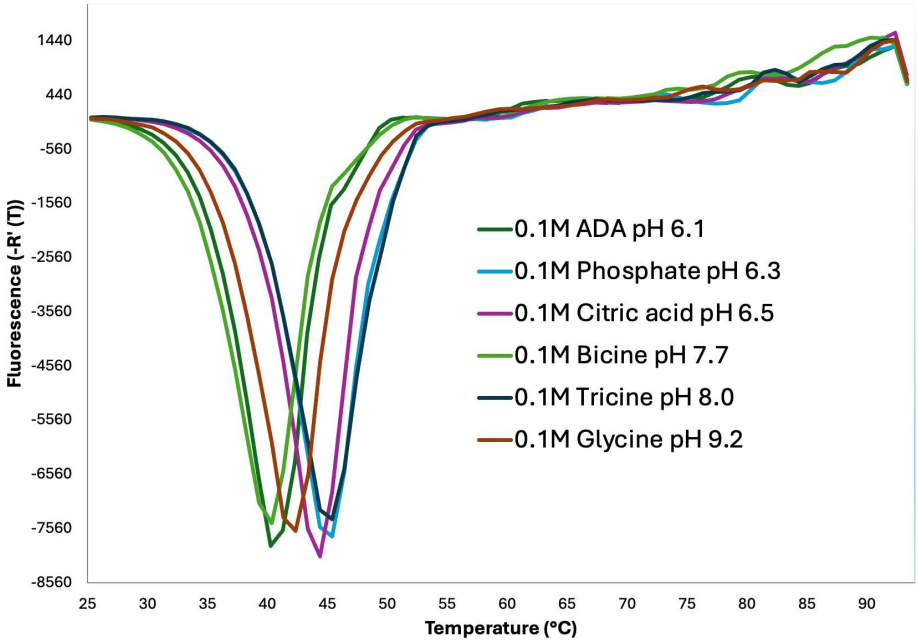

Figure 2.10: Apo-hCA2 pH dissociation curves recorded using the Durham pH Screen.

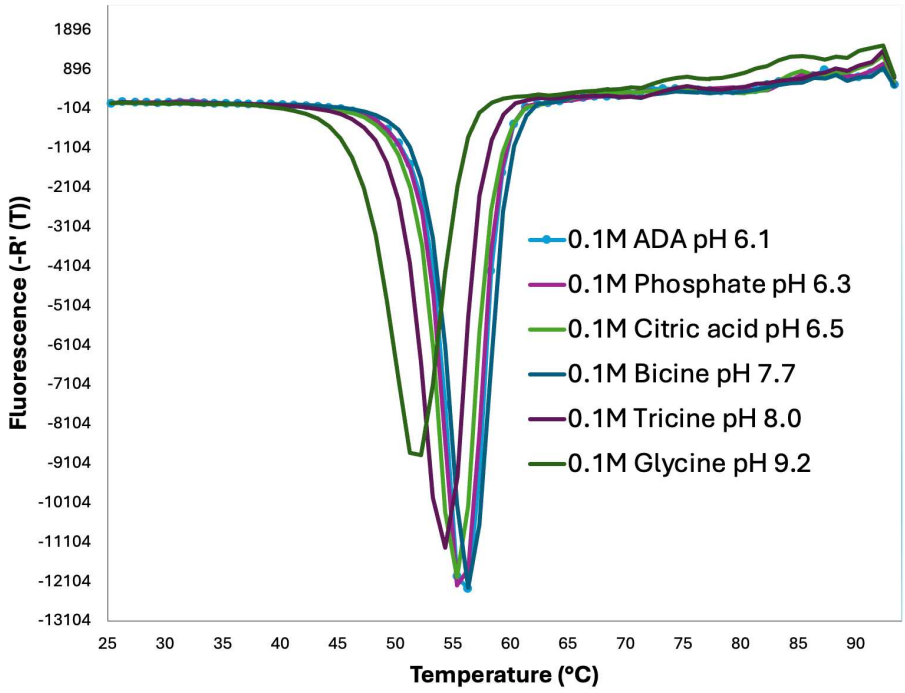

Figure 2.11: Zn-hCA2 pH dissociation curves recorded using the Durham pH Screen.

The results of the Durham Salt Screen performed on the holo-hCA2, showed the greatest stabilization effect (Tm ~50 °C) in presence of 1 M sodium citrate tribasic dihydrate (Figure 2.12). This confirms the ability of this type of salt to stabilize the structure of the protein, indicating it is a possible additive to precipitating agent for crystallization. High stabilization

effects were also determined in the presence of 3 M sodium malonate dibasic monohydrate, 0.01 M sodium phosphate dibasic, and 0.01 M EDTA (data not shown).

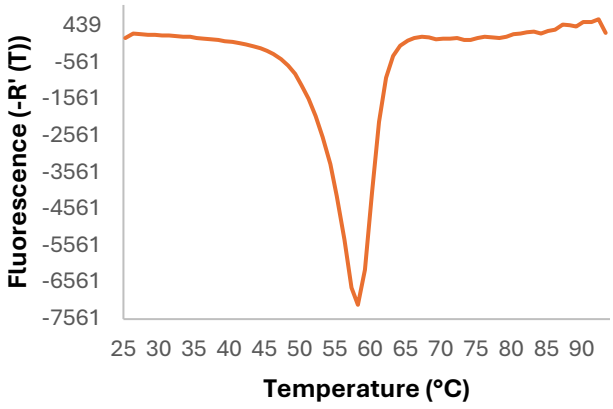

Figure 2.12: Zn-hCA2 dissociation curve recorded in presence of 1 M sodium citrate tribasic dihydrate, belonging to the Durham Salt Screen.

The biophysical properties of Zn^{2+} binding to hCA2 were further characterized by Isothermal Titration Calorimetry (ITC), to determine the association constant (K_{ITC}), the enthalpy change (ΔH_{ITC}), and the binding stoichiometry (n_{ITC}). The titration of apo-hCA2 was performed with a solution of Zn^{2+} acetate • $2H_2O$ in three different buffering solutions, 50 mM TRIS buffer pH 7.8, 50 mM HEPES buffer pH 7.8, and 25 mM MOPS pH 7.4. Among those, the results obtained using the MOPS buffering solution were consistent with data formerly reported in the literature under the same experimental conditions.[46] A representative ITC curve for Zn^{2+} binding to apo-hCA2 in MOPS buffer is shown in Figure 2.13, along with the corresponding integrated data and a one-site binding model fit. Slightly different parameters were determined using the TRIS buffer, whereas in HEPES Zn^{2+} precipitated, generating artifacts that impeded the data analysis.

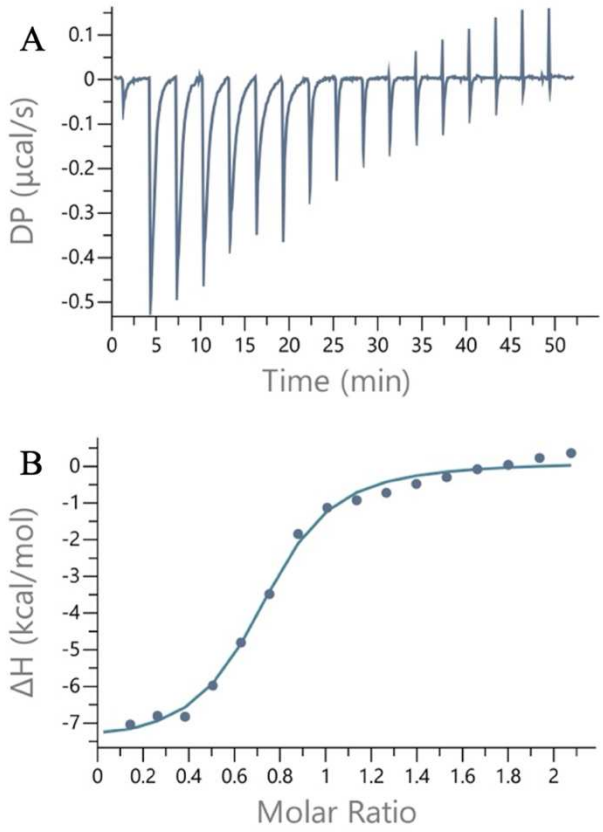

Figure 2.13: (A) ITC data obtained by titrating apo-hCA2 (110 µM, 300 µl with 17 injections of CH_3COO_2 Zn 10 mM, 2.4 µl each) in 25 mM MOPS, pH 7.4. (B) Integrated isotherm and best associated fit for a one site binding model.

The titration curve, characterized by a sigmoidal shape, shows the exothermic nature of Zn^{2+} binding, reaching a plateau around a molar ratio of approximately 2. Although the curve appears to be bimodal, the second transition is very mild and the current fitting models did not give satisfactory results. A fit with a single-site equation, approximating to a stoichiometric ratio of 2:1, albeit simplistic, still shows the presence of two Zn^{2+}-binding sites. The second part of the curve is compatible with a weaker site, possibly the accessory site discussed in more structural detail in this chapter, and this could explain the failure to reach the plateau in the curve. The thermodynamic parameters calculated for Zn^{2+} binding to the apo-hCA2 are reported in Table 2.2, providing insight into the binding affinity, enthalpic, and entropic contributions to the overall process. The data were compared with those reported in the work of Song et al.[50]

Protein	[Syr] (M)	[Cell] (M)	*n* (sites)	K_d (M)	ΔH (kcal/mol)	ΔG (kcal/mol)	$-T\Delta S$ (kcal/mol)
Zn-hCA2	$1.10e^{-3}$	$1.1e^{-04}$	0.7	$3.88e^{-6}$	-7.76	-7.38	0.38
Zn-hCA2 (Song *et al*)[50]	$1.85e^{-3}$	$8\text{-}0e^{-05}$	0.97	$4.55e^{-6}$	-8.1	-8.6	-0.6

Table 2.2: Biophysical values obtained upon titration of apo-hCA2 with Zn^{2+} using the one site binding model. Data were compared with those reported in the study by Song et al.[50]

2.3.3 Apo and Zn-hCA2 structural characterization

The apo-enzyme was crystallized using two precipitants, sodium citrate tribasic dihydrate and ammonium sulphate, according to former reports.[24,26,37] In both conditions, crystals appeared overnight, but they showed slightly different morphologies. Parallelepiped-shaped crystals grew in presence of sodium citrate (Figure 2.14), whereas those originating in ammonium sulphate are clusters of thin plates (Figure 2.15). Any attempts to improve the morphology of the latter (e.g., seeding, grid optimization, change in crystallization temperature) did not give satisfactory results. However, as at the extremities they can be regarded as single crystals, we used them in some of the experiments described in this work.

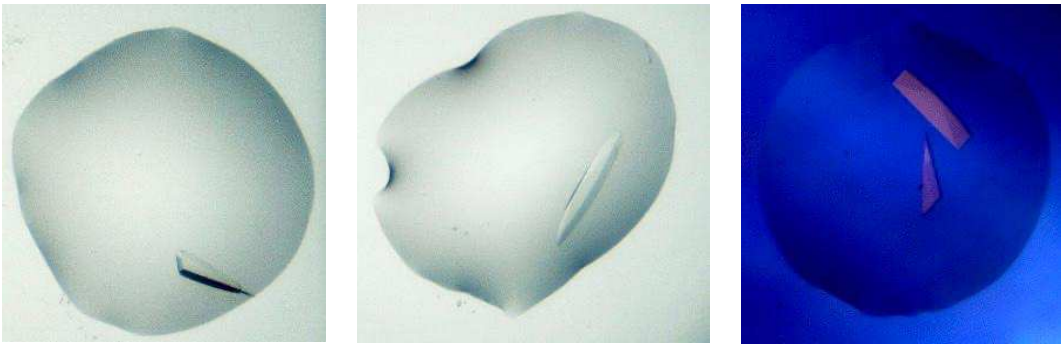

Figure 2.14: Apo-hCA2 in 1.5 M Sodium citrate tribasic dihydrate, 50 mM Tris pH 7.8.

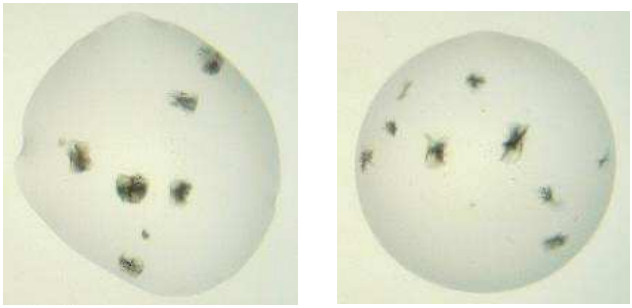

Figure 2.15: Apo-hCA2 in 2.7M ammonium sulphate, 50 mM Tris pH 7.8.

To obtain the Zn^{2+}-bound structures from the apo-hCA2, two techniques were considered: *1)* soaking apo-hCA2 crystals for 2 hours with a solution of 2.5 mM Zn^{2+} and *2)* directly co-crystallizing the apo-enzyme previously incubated the Zn^{2+} solution for 1 hour before setting up the crystallization experiment.

While the apo-enzyme crystallized in both described precipitants, Zn^{2+}-hCA2 co-crystals only formed in the presence of citrate: a summary of the best diffracting crystals can be found in Table 2.3. Despite the different morphology, all crystals belong to the monoclinic space group $P2_1$, with a single chain in their asymmetric unit (ASU). Crystals grown in sodium citrate showed stronger diffracting power than those grown in ammonium sulphate (maximum resolutions of 1.29 Å and 2.00 Å, respectively; Table 2.3), as expected for thicker samples.

Analogous trends were also obtained for the crystals exposed to Zn^{2+} ions (maximum resolutions of 1.75 Å and 1.95 Å, respectively; Table 3). The Zn^{2+} -soaking procedure seemed to slightly decrease the crystal quality: higher resolution diffraction (approximately 1.50 Å) was observed in samples prepared with the co-crystallization approach. All final models for apo-hCA2 and Zn-hCA2 are of good quality, as indicated by their processing and refinement statistics (Table 2.3).

	Apo-hCA2	**Apo-hCA2**	**Zn-hCA2-(COXX)**	**Zn-hCA2-(Soak2h)**	**Zn-hCA2-(Soak2h)**
Precipitant	1.4 M Na_3 citrate *$2H_2O$, 50 mM TRIS pH 7.8	2.6 M ammonium sulphate, 50 mM TRIS pH 7.8	1.4 M Na_3 citrate *$2H_2O$, 50 mM TRIS pH 7.8	1.4 M Na_3 citrate *$2H_2O$, 50 mM TRIS pH 7.8	2.6 M ammonium sulphate, 50 mM TRIS pH 7.8
DATA COLLECTION STATISTICS					
Diffraction source	I04 (DLS)	I24 (DLS)	I30B (ESRF)	I04 (DLS)	I04 (DLS)
Wavelength (Å)	0.9537	0.9537	0.9668	0.9537	0.9537
Temperature (K)	100	100	100	100	100
Detector	Eiger2 XE 16M	Eiger2 XE 16M	EIGER2, 9M	Eiger2 XE 16M	Eiger2 XE 16M
Crystal-detector distance (mm)	168.9	168.9	137.8	189.5	189.5
Space group	$P2_1$	$P2_1$	$P2_1$	$P2_1$	$P2_1$
No. of subunits in ASU	1	1	1	1	1
a, b, c (Å)	42.16, 41.28, 72.05	42.18 41.45 72.19	42.24 41.43 72.42	42.49 41.63 73.14	42.29 41.48 72.71
β (°)	104.23	104.18	104.48	104.52	104.45
Resolution range (Å)	69.84-1.29 (1.31-1.29)	69.99-2.00 (2.05-2.00)	41.43 - 1.50 (1.53 - 1.50)	41.63- 1.75 (1.78-1.75)	70.41-1.95 (2.00-1.95)
Total no. of reflections	118561 (5853)	104739 (1271)	264266 (12535)	164007 (9690)	121886 (8543)
No. of unique reflections	60694 (2973)	1659(213)	39123 (1922)	24824 (1373)	18063 (1275)
Completeness (%)	100 (100)	100.0 (100.0)	100.0(100.0)	98.4(100.0)	99.9 (100.0)
Multiplicity	2.0 (2.0)	6.3 (6.4)	6.8 (6.5)	6.6 (7.1)	6.7 (6.7)

(I / σ(I))	12.3 (1.3)	6.4 (1.8)	8.7 (1.6)	10.4 (2.2)	6.6 (1.6)
CC1/2	0.99 (0.72)	0.99 (0.66)	0.99 (7.1)	6.6 (7.1)	0.98 (0.62)
R_{meas}	0.042 (0.502)	0.23 (1.33)	0.131 (1.349)	0.115 (0.639)	0.218 (1.33)
Overall B factor from Wilson plot ($Å^2$)	11.9	21.3	12.4	18.4	21.5
REFINEMENT STATISTICS					
Resolution range (Å)	69.84-1.29 (1.32-1.29)	69.99-2.00 (2.05-2.00)	40.93-1.50 (1.53-1.50)	41.16-1.75 (1.79-1.75)	70.41-2.00 (2.05-2.00)
Completeness (%)	100.0 (100.0)	99.99 (100.0)	99.91 (99.79)	98.06 (99.9)	99.4 (100.0)
No. of reflections, working set	57669 (4232)	15755 (1157)	37026 (2712)	23394 (1743)	15837 (1170)
No. of reflections, test set	3007 (225)	835 (52)	2048 (138)	1345 (89)	838 (52)
Final R_{cryst}	0.1873 (0.285)	0.1859 (0.293)	0.1738 (0.264)	0.1944 (0.373)	0.2080 (0.154)
Final R_{free}	0.2111 (0.316)	0.2550 (0.369)	0.1995 (0.278)	0.2389 (0.249)	0.2910 (0.287)
No. of non-H atoms					
Protein	260	260	260	260	260
Ligand	-	-	1	0	-
Ion	-	-	2	2	2
Water	295	116	283	243	273
Total	584	376	545	305	535
R.m.s. deviations bonds (Å)	0.003	0.008	0.005	0.005	0.007
Angles (°)	1.095	1.570	1.071	1.336	1.590
Average B factor ($Å^2$)	15.14	27.9	15.82	23.6	24.12
Estimate error on coor. based on R value (Å)	0.054	0.21	0.306	0.140	0.254
Ramachandran plot					
Most favored (%)	96.1	97,3	95.7	97.3	95.3
Allowed (%)	2.9	2.7	4.3	2.7	4.7

Table 2.3: Data collection, processing, and refinement statistics of structure Apo-hCA2 in 1.4M Na_3 citrate • $2H_2O$, 50 mM TRIS pH 7.8; Apo-hCA2 in 2.6 M ammonium sulphate, 50 mM TRIS pH 7.8, hCA2; Zn-hCA2-(COXX) and Zn-hCA2-(Soak2h). Values in parentheses refer to the high-resolution shell.

Although at different resolutions, the two apo-structures are almost identical (rmsd upon Cα matching of 0.148Å). The same structural homology was also observed by comparing the two Zn-hCA2 obtained through the soaking procedure (rmsd upon Cα matching of 0.132Å). These results validate the application of both crystallization conditions for structural investigations of metal binding to hCA2. Indeed, no structural changes are induced by the different crystallization environments. To further validate the methods applied for characterizing the holo-enzyme, the Zn-hCA2 structures obtained by the soaking and co-crystallization methods were compared, showing almost identical models (rmsd upon Cα matching of 0.134 Å). On this basis, the highest resolution structural models for apo-hCA2 and Zn-hCA2 are used in the discussion.

As formerly reported in the literature, the structure of hCA2 is very rigid and no major rearrangements are induced upon Zn^{2+} binding (rmsd upon Cα matching of 0.147 Å). A closer view of the active site area shows conserved networks of water molecules in the apo and holo-states of the enzyme, including W_{Zn}, the deep water and those interacting with Thr200. This suggests that zinc binding plays a minor role in forming and/or stabilizing the solvent network inside the catalytic cavity.[21,33] In the structure of the apo-enzyme, the proton shuttle residue His64 adopts two alternative conformations. The 'out' conformation, pointing outside the catalytic cavity, is slightly more represented than the 'in' orientation, exposing the imidazole ring in the active site (estimated occupancies of 60% and 40%, respectively). These two alternative orientations were consistently observed in former models of apo-hCA2 (PDB id 6LUU.[31] Notably, they were also described in the structures of holo-enzyme PDB id 2ILI,[24] 6LUW,[31] by contributing to shine light on the mechanism of action displayed in Figure 2.16.

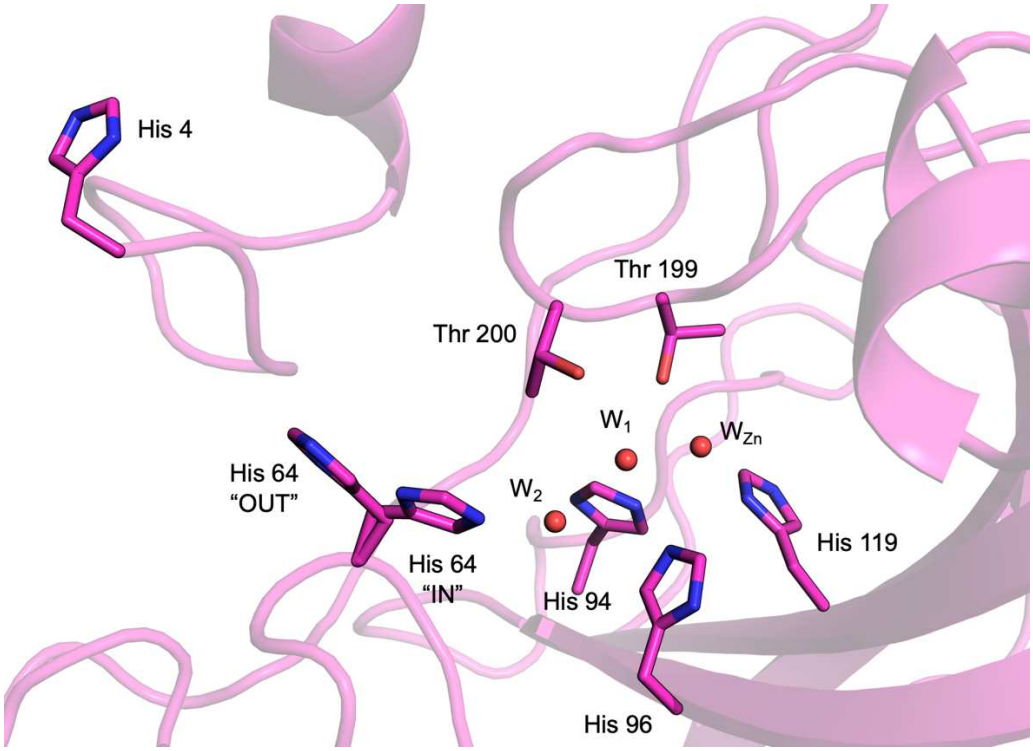

Figure 2.16: Interface view of APO-hCA2 in cartoon, and the interacting residues in sticks. The key water molecules are depicted as red spheres.

On the other hand, in our structure of Zn-hCA2, His64 is only observed in the 'out' conformation where it coordinates a second Zn^{2+} ion together with His4, on the N-terminal tail (Figure 2.17). Zn^{2+} ions populate this site, named Zn2 site, to 35-40% extent, showing a tetrahedral coordination geometry (only one water molecule is observed, reasonably because of the partial occupancy). The population of this secondary site by a Zn^{2+} ion is validated by the anomalous data collected at the Zn K-edge. Indeed, a positive signal (> 7σ) is observed in

the map calculated from the data collected above the edge that disappears in the map derived from the data obtained below the edge (Figure 2.17). The population of the Zn2 site by Zn^{2+} ions was repeatedly observed by us in all Zn-hCA2 structures (obtained by soaking in both precipitants, and by co-crystallization), with estimated occupancies up to 40%. To our knowledge, this is the first report of Zn^{2+} binding on this site of hCA2. The population of this accessory Zn2 site does not affect the binding of the catalytic Zn^{2+} ion (Zn1 site), whose position and coordination is fully retained with respect to formerly reported models (e.g., PDB ID: 2ILI).[24] Indeed, in the Zn1 site, the Zn^{2+} ion is tetrahedrally coordinated by the His94, His96, and His119, and the nucleophilic water/hydroxide species, W_{Zn}. In our Zn-hCA2 structure, also the population of the Zn1 site was validated by the anomalous data collected at the Zn K-edge, resulting in strong anomalous signals (> 20σ) in the map calculated from the data collected above the edge (disappearing in the map derived from the data obtained below the edge; Figure 2.17. To better characterize this accessory site, five mutants, having histidine residues of the Zn1 and Zn2 sites changed to alanine, were generated and investigated (vide infra).

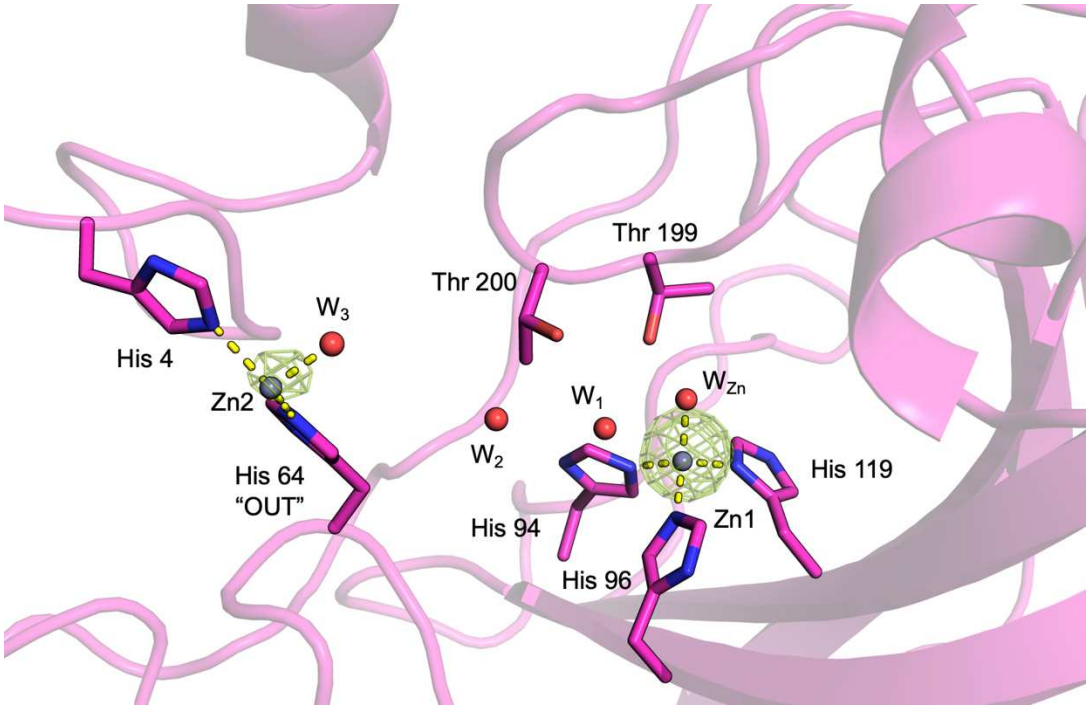

Figure 2.17: Interface view of Zn-hCA2 in cartoon. The interacting residues are shown in stick representation, with the two zinc ions depicted as grey spheres and the key water molecules represented as red spheres. Zinc ions are surrounded by anomalous difference map (smudge mesh) contoured at 5.0 σ.

The Zn-hCA2 structure determined by soaking the apo-enzyme crystals grown using sodium citrate as precipitant displayed an additional feature. In the active site area, an additional electron density was observed having shape and size compatible with a molecule of pyridine-

2-carboxylic acid (ligand id 6PC; Figure 2.18). This molecule originates from the chelation buffer where it was present as a contaminant of the chelating agent, the pyridine-2,6-dicarboxylic acid. This adventitious ligand is bound in the active site where it is H-bonded to the water/hydroxide species, Thr199 and Thr200 (Figure 2.18). The pyridine ring is stabilized by the hydrophobic wall lined by Val121, Phe130, Val134, Leu140, Leu197, Pro201, and Leu203. Moreover, it forms water-mediated interactions with Asn67 and Gln 92.

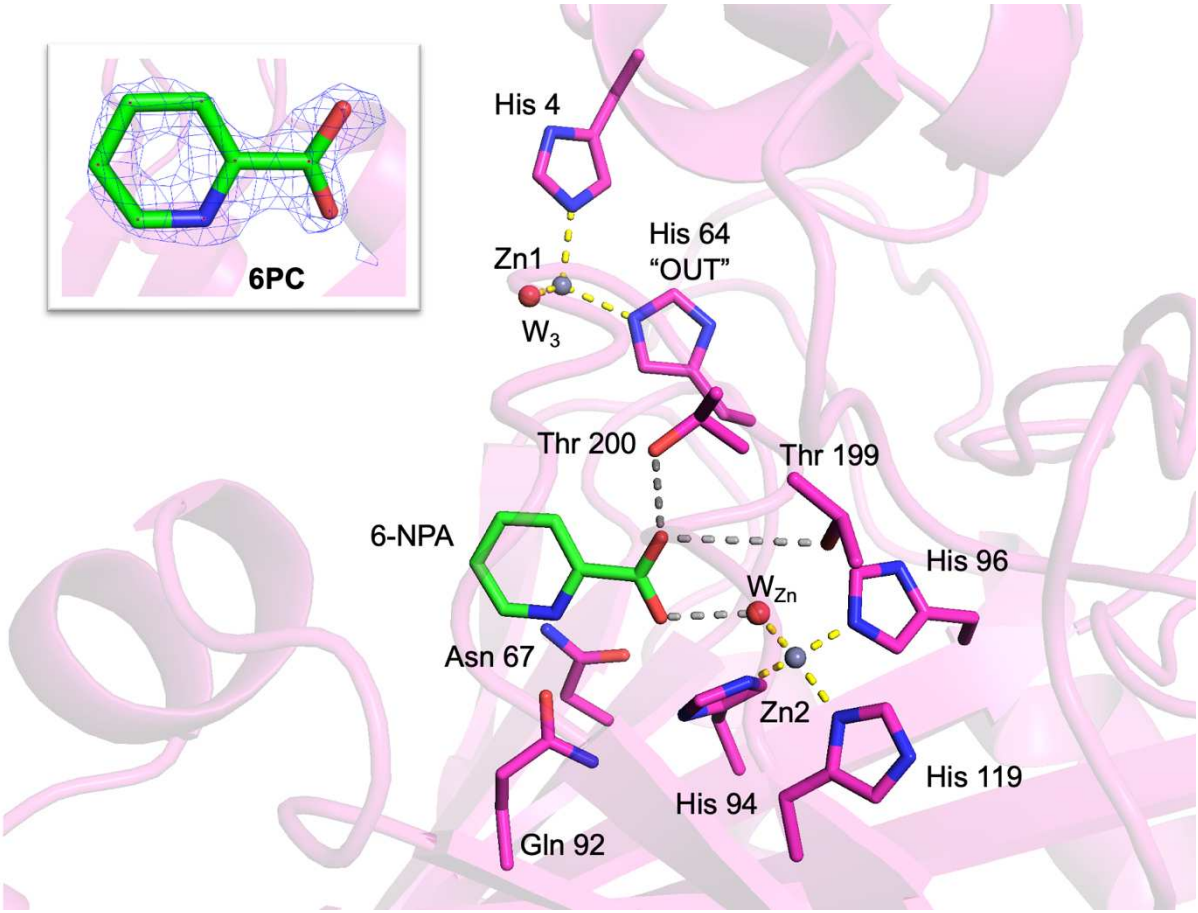

Figure 2.18: *Interface view of Zn-hCA2 in cartoon. The interacting residues are shown in stick representation, with the two zinc ions depicted as grey spheres and the key water molecules represented as red spheres. Coordination bonds are illustrated as yellow dashed lines. Hydrogen bonds are illustrated as grey dashed lines. The ligand 6PC is shown in stick representation, as visible in the 2Fo-fc electron density map (blue mesh) contoured at the 1.5 σ level.*

2.3.4 Expression and purification of the five Ala-scan mutants of hCA2

The hCA2 variants were generated by site-directed mutagenesis using partially overlapping primers and the plasmid encoding for the wild-type enzyme as a template for the PCR reaction. Following the PCR amplifications and the plasmid extractions (Figure 2.19), the variants were verified by gene sequencing (also confirming the lack of any unwanted mutations).

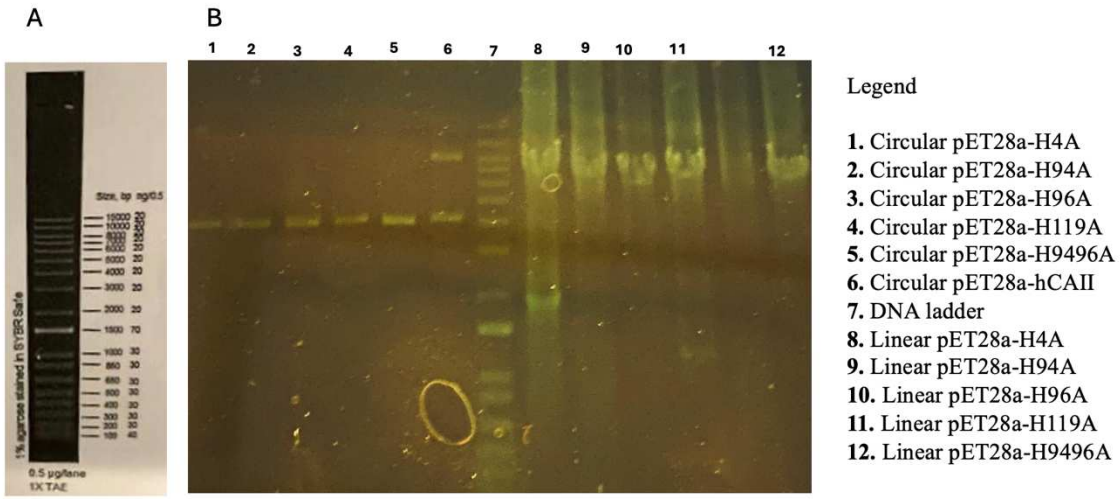

Figure 2.19: (A) Invitrogen marker (Kb plus DNA ladder) scheme. (B) DNA electrophoresis analysis of variants. In lanes 1-6, pET28a H4A, H94A, H96A, H119A, H94A-H96A, and WT (3900 bp) in a circular form; in lane 7 DNA ladder; and in lanes 8-12 the linearized variants DNA (5920 bp).

All variants were produced in *E. coli* BL21(DE3) cells and purified by affinity and size-exclusion chromatography using the same procedures described for the wild-type enzyme. The chromatograms and SDS-PAGE analyses for main purification steps of the five variants are shown in Figures 2.20-2.24. All variants were produced and purified in yields similar to the wild-type enzyme (Ranging from ≈250 mg L^{-1} to ≈ 150 mg L^{-1}).

2.3.4.1 Purification of H4A

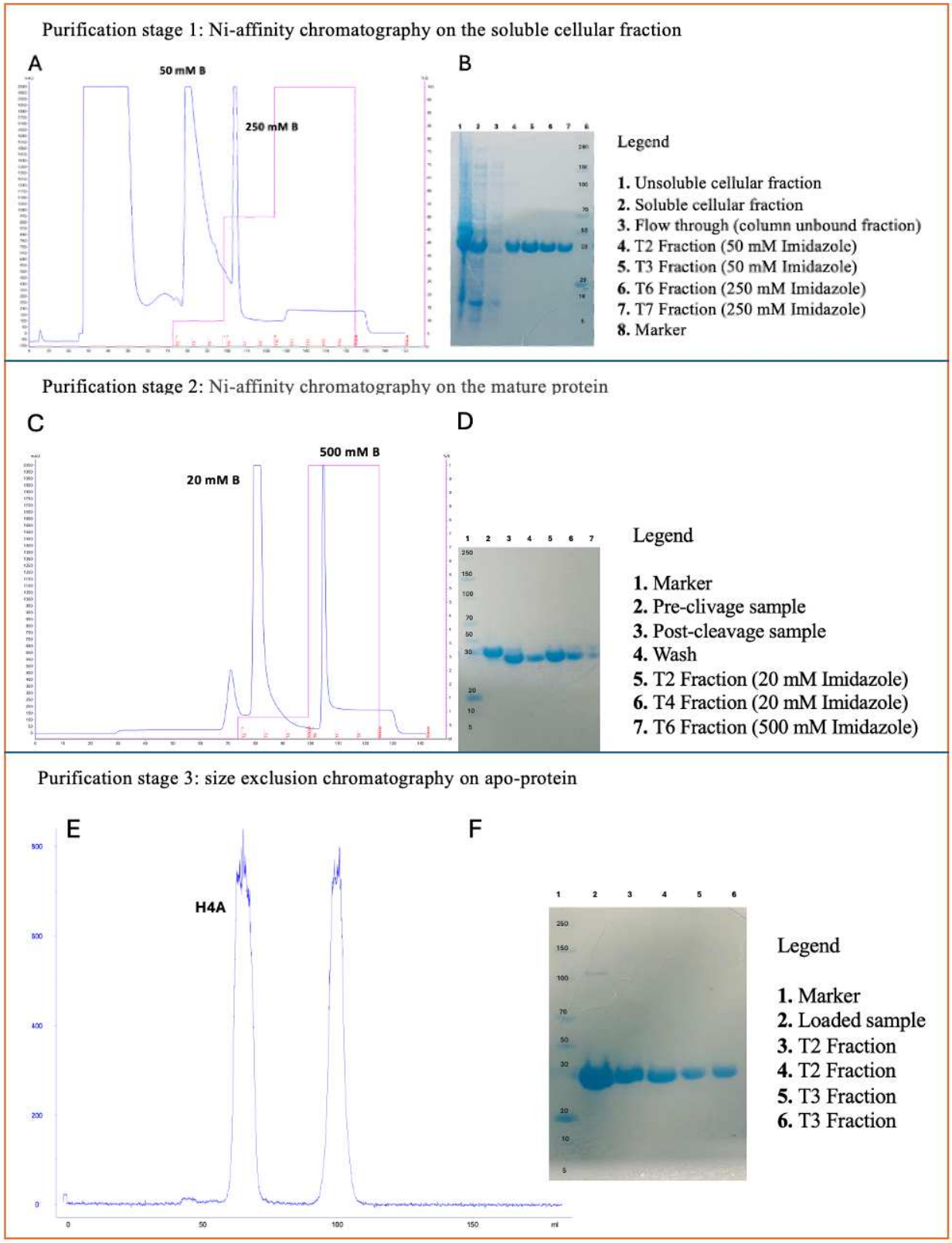

Figure 2.20: (A) Affinity chromatography of H4A-hCA2 obtained using a HisTrap FF 5 mL column (GE Healthcare). (B) SDS-PAGE analysis of the fractions collected (MW_{hCA2}: 31782 Da. (C) Chromatogram of mature H4A-hCA2 (D) SDS-PAGE analysis of the fractions collected (MW_{hCA2}: 29571 Da) (E) Gel filtration chromatogram of protein purification using a HiLoad 16/600 Superdex 75 pg column (GE Healthcare). (F) SDS-PAGE analysis of the fractions collected from SEC.

2.3.4.2 Purification of H94A

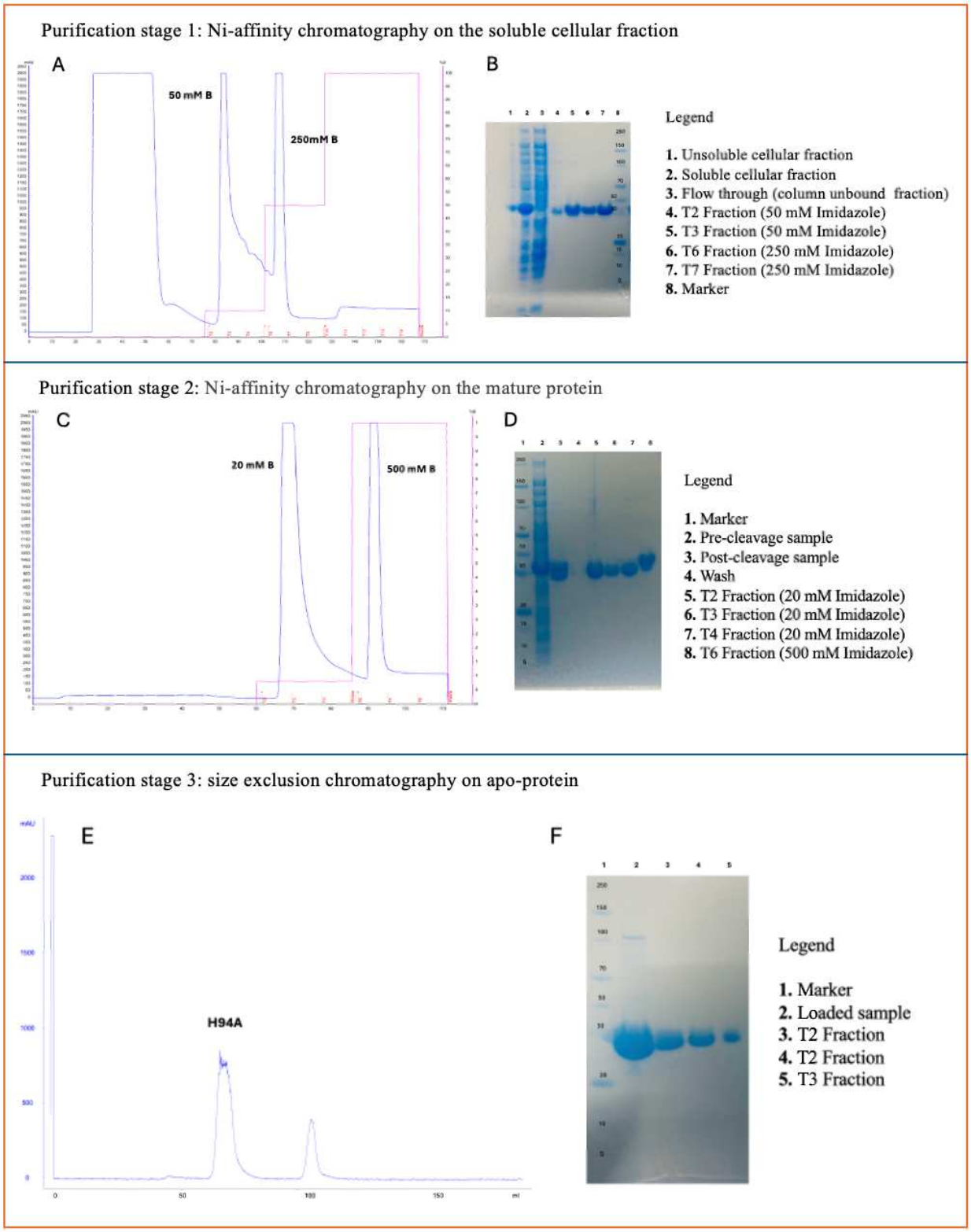

Figure 2.21: (A) Affinity chromatography of H94A-hCA2 obtained using a HisTrap FF 5 mL column (GE Healthcare). (B) SDS-PAGE analysis of the fractions collected (MW_{hCA2}: 31782 Da. (C) Chromatogram of mature H94A-hCA2 (D) SDS-PAGE analysis of the fractions collected (MW_{hCA2}: 29571 Da) (E) Gel filtration chromatogram of protein purification using a HiLoad 16/600 Superdex 75 pg column (GE Healthcare). (F) SDS-PAGE analysis of the fractions collected from SEC.

2.3.4.3 Purification of H96A

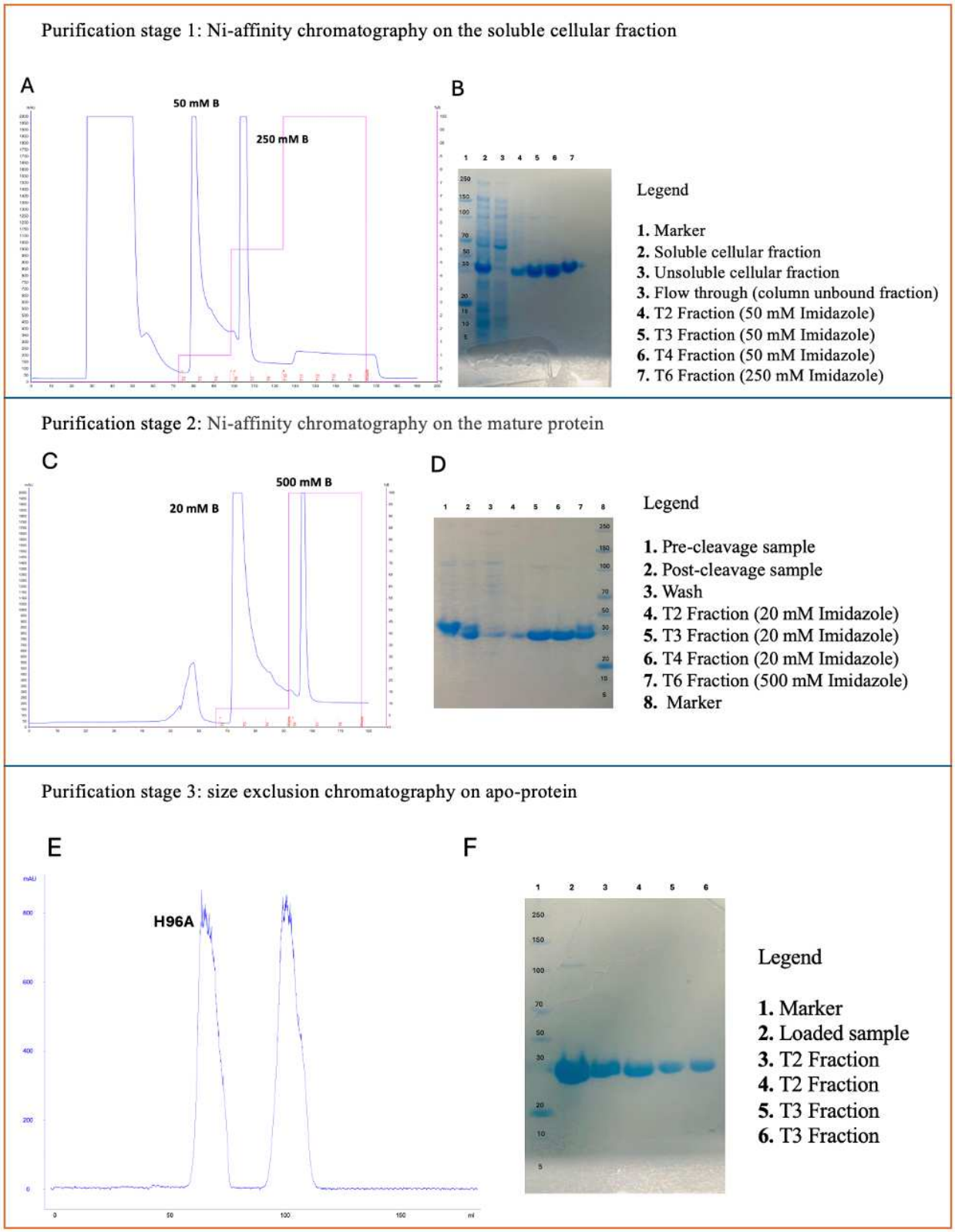

Figure 2.22: (A) Affinity chromatography of H96A-hCA2 obtained using a HisTrap FF 5 mL column (GE Healthcare). (B) SDS-PAGE analysis of the fractions collected (MW_{hCA2}: 31782 Da. (C) Chromatogram of mature H96A-hCA2 (D) SDS-PAGE analysis of the fractions collected (MW_{hCA2}: 29571 Da) (E) Gel filtration chromatogram of protein purification using a HiLoad 16/600 Superdex 75 pg column (GE Healthcare). (F) SDS-PAGE analysis of the fractions collected from SEC.

2.3.4.4 Purification of H119A

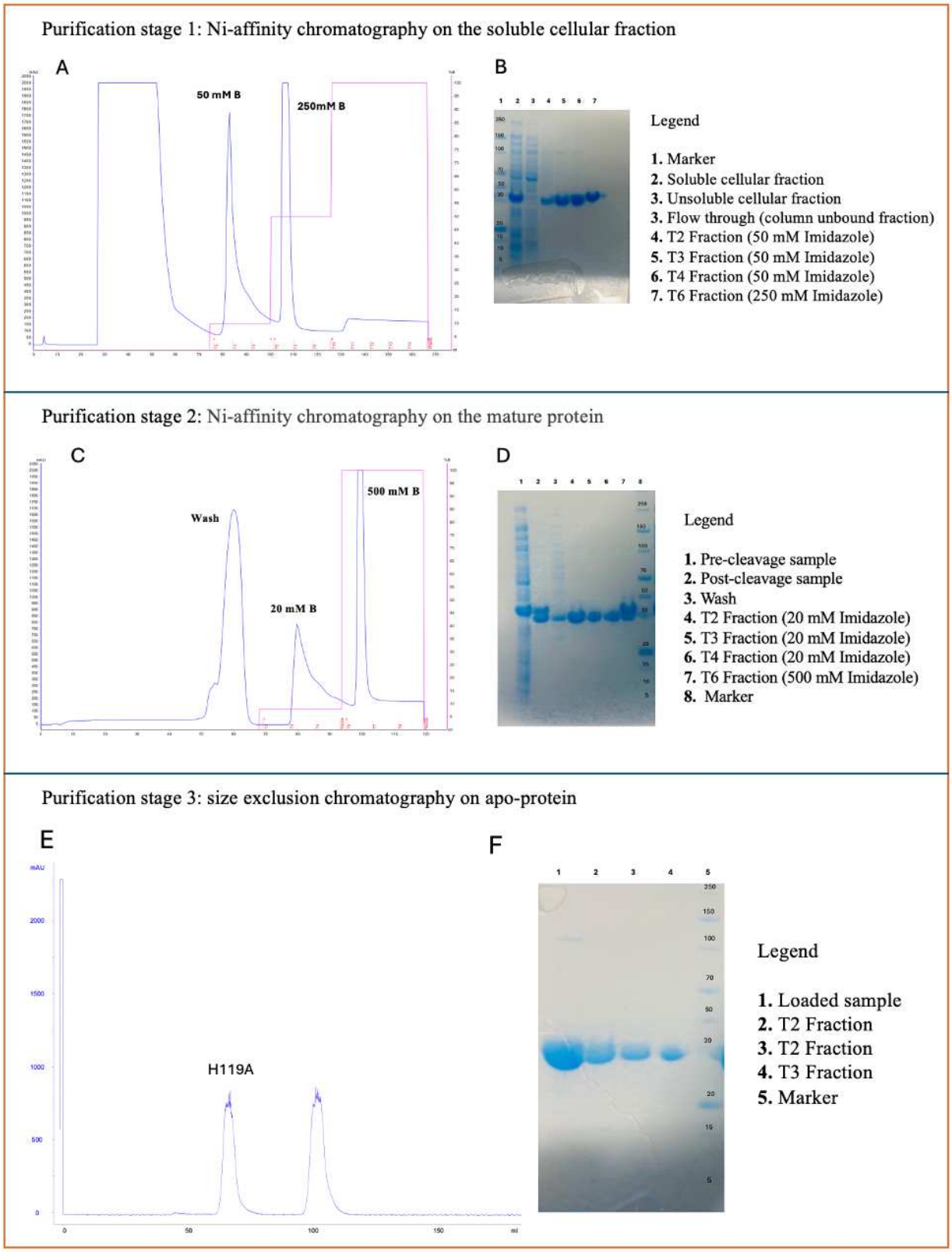

Figure 2.23: (A) Affinity chromatography of H119A-hCA2 obtained using a HisTrap FF 5 mL column (GE Healthcare). (B) SDS-PAGE analysis of the fractions collected (MW_{hCA2}: 31782 Da. (C) Chromatogram of mature H119A-hCA2 (D) SDS-PAGE analysis of the fractions collected (MW_{hCA2}: 29571 Da) (E) Gel filtration chromatogram of protein purification using a HiLoad 16/600 Superdex 75 pg column (GE Healthcare). (F) SDS-PAGE analysis of the fractions collected from SEC.

2.3.4.5 Purification of H94A-H96A

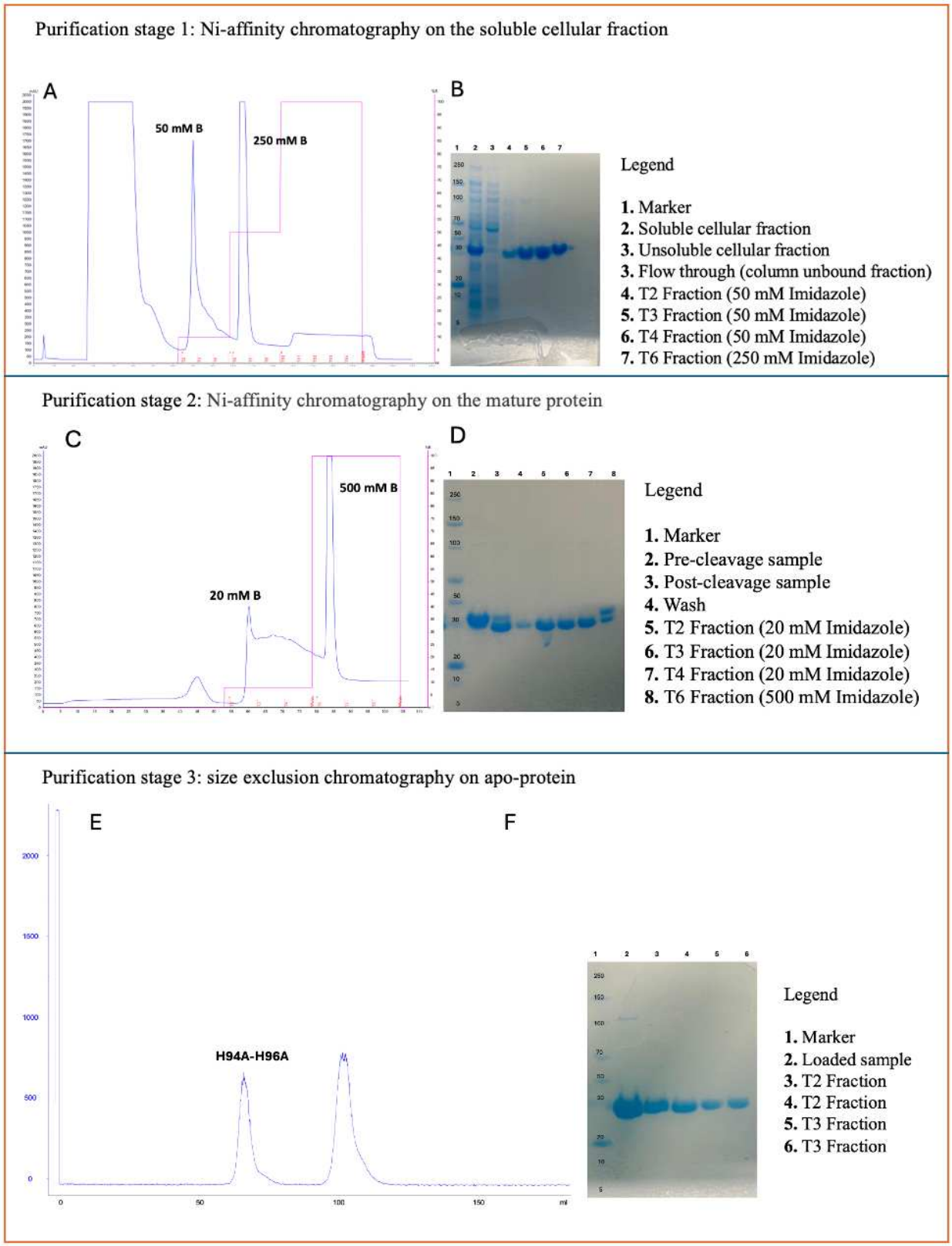

Figure 2.24: (A) Affinity chromatography of H94A-H96A-hCA2 obtained using a HisTrap FF 5 mL column (GE Healthcare). (B) SDS-PAGE analysis of the fractions collected (MW_{hCA2}: 31782 Da. (C) Chromatogram of mature H94A-H96A-hCA2 (D) SDS-PAGE analysis of the fractions collected (MW_{hCA2}: 29571 Da) (E) Gel filtration chromatogram of protein purification using a HiLoad 16/600 Superdex 75 pg column (GE Healthcare). (F) SDS-PAGE analysis of the fractions collected from SEC.

2.3.5 hCA2 and Variants Kinetic Characterization

Monitoring the reversible hydration of carbon dioxide to bicarbonate catalysed by hCA2 is challenging because of the very high reaction rates. As an alternative, the catalytic activity of hCA2 can be monitored by following the conversion of pNPA into pNP and acetic acid using UV-vis spectroscopy[51] The esterase kinetic assays performed on hCA2, and its variants allowed to evaluate the contribution of each residue to the catalysed reaction. All mutations introduced at the Zn1 site drastically compromised the catalytic activity of the enzyme (Table 2.4). At variance with the H96A and H119A mutants that were completely inactive, a detectable residual activity was measured for the H94A variant. The effects of the mutations concerned both the affinity for the substrate and the turnover rate, resulting in slightly increased k_M and lower k_{cat} values with respect to the wild-type enzyme (hCA2: k_M = 2.85 mM, k_{cat} = 107.6 s^{-1}; H94A: k_M = 8.60 mM, k_{cat} = 4.4 s^{-1}). The additional contributions of the H94A and H96A mutations occurring in the double variant resulted in the complete loss of catalytic activity as well. On the other hand, the mutation introduced at the Zn2 site seemed not affecting the catalytic activity of the enzyme. The same kinetic parameters were measured for the wild-type enzyme and the H4A mutant (H4A*:* k_M = 3.28 mM, k_{cat} = 120.2 s^{-1}), suggesting that this residue has a minor impact on the catalysed reaction.

	V_{max} (µM/s)	k_m (µM)	k_{cat} (s^{-1})	k_{cat}/k_m ($\mu M^{-1}\ s^{-1}$)
hCA2	1.26	2851	107.57	0.03722
H4A-hCA2	1.54	3276	120.17	0.06677
H94A-hCA2	1.06	8596	4.44	0.00055

Table 2.4: Kinetic characterization of hCA2 and its variants H4A-hCA2 and, H94A-hCA2.

2.3.6 hCA2 alanine mutants' characterization: binding assays

Each mutant was characterized thermodynamically, structurally, and kinetically. Isothermal calorimetry (ITC) analysis was conducted to determine the association constant (K_{ITC}), enthalpy change (ΔH_{ITC}), and binding stoichiometry (n_{ITC}). H4A-hCA2, H94A-hCA2, H96A-hCA2, H119A-hCA2, and H94A-H96A-hCA2 were titrated in the $(CH_3COO)_2$ Zn • $2H_2O$ in 25 mM MOPS pH 7.4 under the same condition described for the WT-hCA2. Several

isothermal titration curves representative of Zn^{2+} binding to the mutants were obtained, and the resulting data were analysed using one site and two site binding models.

2.3.6.1 Isothermal calorimetry (ITC)

The experiments described above for the titration of the holo-enzyme with Zn^{2+} have been repeated for the mutants. The H4A-hCA2 titration curve, similar to that of the wild-type protein, displays a clear upward sigmoidal shape representative of a strong exothermic interaction between the ligand and the target (Figure 2.25). Differently from the first case, however, the 1:1 stoichiometry indicates only one Zn^{2+} site, compatible with the ablation of the accessory/adventitious Zn2 site. Enthalpy change (*ΔH*) is strongly negative, indicating a strong release of heat in interaction and a favourable binding process. The thermodynamic parameters associated with Zn^{2+}binding to the H4A-hCA2 are reported in Table 2.5, providing insight into the binding affinity, enthalpic, and entropic contributions to the overall process.

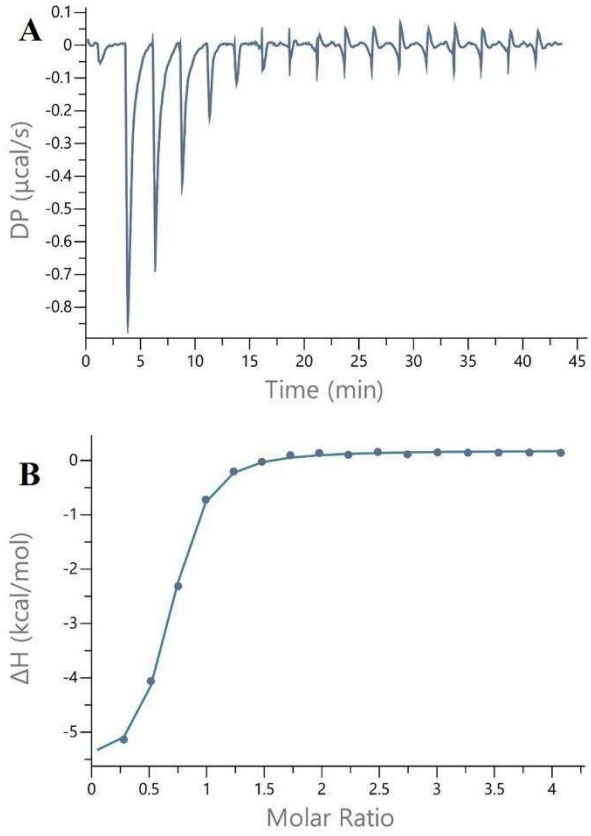

Figure 2.25: (A) Isothermal titration calorimetry data involved titrating 110 µM, apo-H4A (300 µl) with 17 injections × 2.4 µl of 10 mM of $CH_3COO)_2$ Zn (70µl) in 25 mM MOPS at pH 7.4. (B) Integrated isotherm and best associate fit for a one site binding model.

The shape of the H94A-hCA2 titration curve is significantly different from those described previously. A first exothermic section with a 1:1 stoichiometry, is followed by an endothermic

one, indicating strong and 'competing' behaviours for the different Zn^{2+}sites (Figure 2.26). The stoichiometry of this latter part is higher than 1:1, possibly indicating the co-existence of multiple states linked to the second process. This complex interaction originates by a combination of high- and low-affinity interactions, and the deconvolution of states is way more complex than for the wild-type and H4A mutant. A site model fitting was used to obtain the thermodynamic parameters reported in Table 2.5.

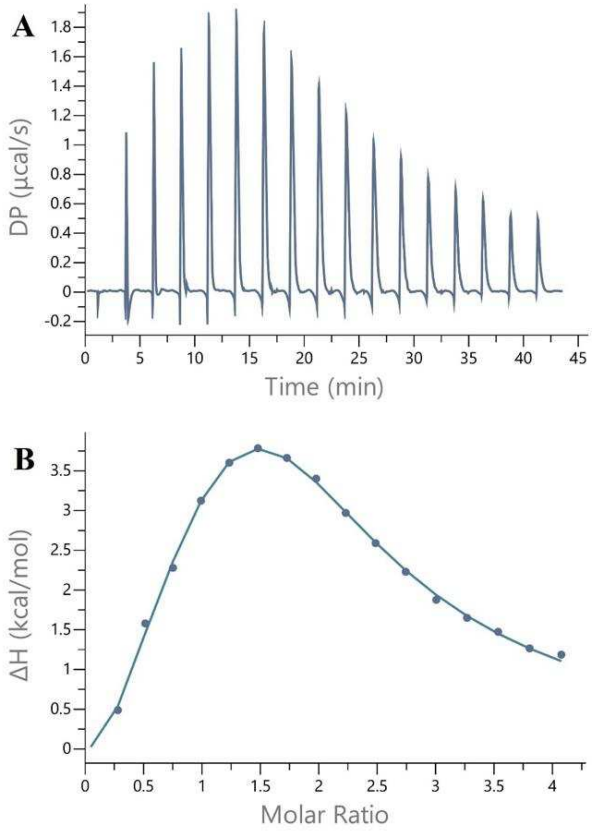

Figure 2.26: (A) Isothermal titration calorimetry data involved titrating 110 µM, apo-H94A (300 µl) with 17 injections × 2.4 µl of 10 mM of $CH_3COO)_2$ Zn (70µl) in 25 mM MOPS at pH 7.4. (B) Integrated isotherm and best associate fit for a two site binding model.

The titration curve for H96A-hCA2 was more complex to fit using either a one site or two site binding model. The initial differential power (DP) peaks seem to indicate an endothermic interaction, with a partial heat absorption at stoichiometry of approximately 1:1 (inflection at n<1), gradually moving to an exothermic curve for a second 1:1 site (inflection at n=2). Analysing the normalized heat (ΔH) as a function of the molar ratio with the closest fitting model (1 set of sites) reveals a binding enthalpy of approximately −2.5 kcal/mol.

However, as stated above, the binding mode seems to be more complex and would require a dedicated study of fitting functions (Figure 2.27). Based on the structural data obtained, the presence of two binding sites is expected, so further experiments will be needed to validate

these results. The thermodynamic parameters associated with zinc binding to the H96A-hCA2 are reported in Table 2.5.

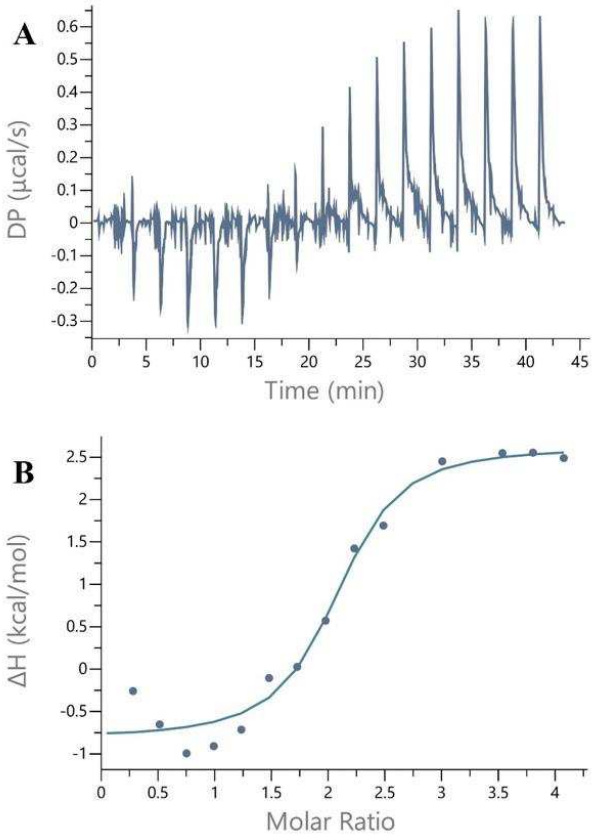

Figure 2.27: (A) Isothermal titration calorimetry data involved titrating 110 µM, apo-H96A (300 µl) with 17 injections × 2.4 µl of 10 mM of $(CH_3COO)_2$ Zn (70µl) in 25 mM MOPS at pH 7.4. (B) Integrated isotherm and best associated fit for a one site binding model.

In the H119A-hCA2 ITC curve, the DP trace displays an initial exothermic trend, followed by absorption of heat in the second part of the titration (Figure 2.28). The normalized heat (ΔH) as a function of the molar ratio reveals a bell-shaped curve, similar to that observed for the H94A variant, suggesting a complex binding mechanism involving two distinct events with differing stoichiometries and affinities. This behaviour suggests the presence of additional/transient interactions, potentially involving weaker or secondary binding sites. The thermodynamic parameters associated with zinc binding to the H119A-hCA2 are reported in Table 2.5.

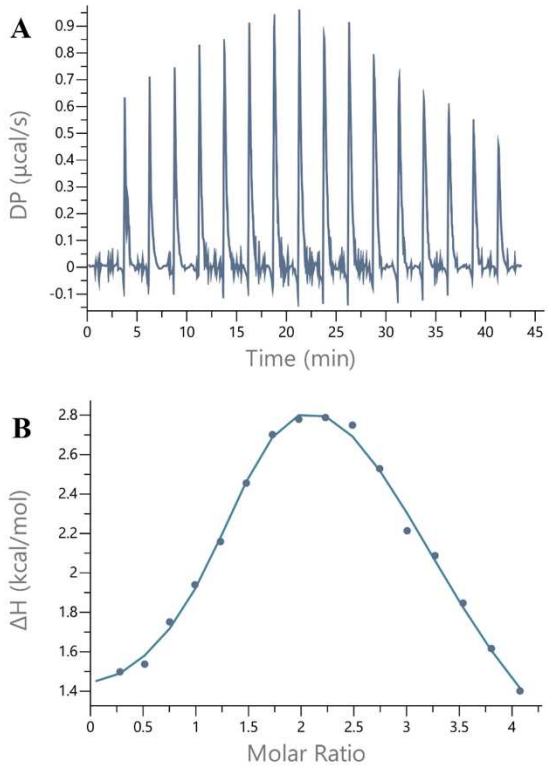

Figure 2.28: (A) Isothermal titration calorimetry data involved titrating 110 µM, apo-H119A (300 µl) with 17 injections × 2.4 µl of 10 mM of $(CH_3COO)_2$ Zn (70µl) in 25 mM MOPS at pH 7.4.
(B) Integrated isotherm and best associated fit for a two-site binding model.

The calorimetric titration curve for the double mutant H94A-H96A reveals an overall exothermal interaction between the protein and Zn^{2+} (Figure 2.29). Despite an initial upward trend, the curve is mostly sigmoidal with a stoichiometry of 1:2. This seems to indicate that the complexity of H96A and the heat inversion (*i.e.* the change from exothermic to endothermic) displayed for H94A is now mitigated. Our fitting using a single set of sites is characterized by an overall favourable ΔG for the two sites. This seems to indicate that the double mutation, as well as H119A, is still not sufficient to ablate the primary Zn^{2+} site. Although the interaction might be weakened, Zn^{2+} would still be able to coordinate the primary site, albeit modifying the catalytic properties of the metallic site.

While this might imply a stoichiometry of two ligands for each target molecule, structural evidence contradicts this interpretation (section 2.4.3.2). Another possible interpretation for the apparent 1:2 stoichiometry could also indicate secondary effects, such as non-specific or transient interactions between the ligand and other accessible surfaces of the target. These interactions might provide additional calorimetric signals that skew the observed binding behaviour. The thermodynamic parameters related to zinc binding to the H94A-H96A-hCA2 are detailed in Table 2.5.

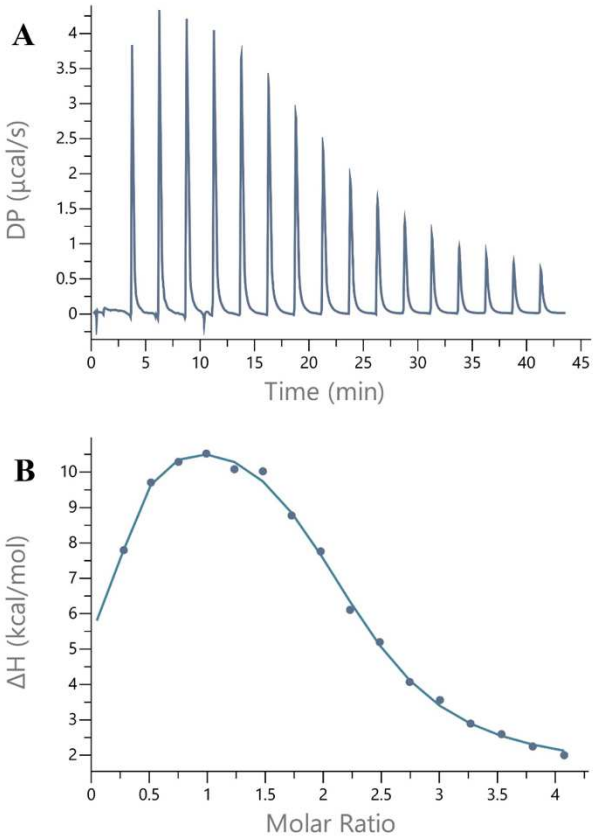

Figure 2.29: (A) Isothermal titration calorimetry data involved titrating 110 µM, apo-H94A-H96A (300 µl) with 17 injections × 2.4 µl of 10 mM of $(CH_3COO)_2$ Zn (70µl) in 25 mM MOPS at pH 7.4. (B) Integrated isotherm and best associated fit for a two-site binding model.

Protein	**[Syr] (M)**	**[Cell] (M)**	***n* (sites)**	***Kd* (M)**	**Δ*H*** **(kcal/mol)**	**Δ*G*** **(kcal/mol)**	**-*T*Δ*S*** **(kcal/mol)**
Zn-hCAII	$1.10e^{-3}$	$1.1e^{-4}$	0.7	$3.88e^{-6}$	-7.76	-7.38	0.38
Zn-H4A	$2.20e^{-3}$	$1.1e^{-4}$	0.605	$4.37e^{-6}$	-5.90	-7.31	-1.42
Zn-H94A	$3.00e^{-3}$	$1.5e^{-4}$	0.675	$46.8e^{-6}$	-10.8	-5.91	-4.89
			1.91	$1.41e^{-4}$	11.3	-5.25	-16.6
Zn-H96A	$2.20e^{-3}$	$1.1e^{-4}$	2.00	$4.17e^{-6}$	-3.44	-7.34	-3.90
Zn-H119A	$2.20e^{-3}$	$1.1e^{-4}$	1.31	$2.08e^{-6}$	0.73	-7.55	-8.48
			2.47	$40.0e^{-4}$	3.06	-6.00	-9.06
Zn-H9496A	$2.20e^{-3}$	$1.1e^{-4}$	$4.3e^{-2}$	$2.23e^{-6}$	-52.6	-7.71	44.9
			2.22	$13.2e^{-6}$	10.6	-6.66	-17.2

Table 2.5: *Fit values obtained to titration of Zn^{2+}in apo-hCA2 apo H4A-hCA2, apo H94A-hCA2, apo-H96A-hCA2, apo-H119A-hCA2, and apo-H94A-H96A-hCA2.*

2.3.7 Structural characterization of H4A-hCA2, H94A-hCA2, H96A-hCA2, H119A-hCA2, and H94A-H96A-hCA2

The apo-forms of all alanine variants were crystallized under the same conditions formerly described for the wild-type enzyme. Different crystal morphologies were observed using sodium citrate (Figure 2.30) and ammonium sulphate as precipitating agents. Since the crystals grown under ammonium sulphate conditions displayed poorer diffraction patterns, Zn^{2+} loading experiments were performed on the crystals obtained using sodium citrate precipitants. Indeed, the holo-state of the variants was characterized by soaking preformed apo-protein crystals with Zn^{2+} ions for 2 hours.

Figure 2.30: Apo-H4A, APO-H94A, Apo-H96A, Apo-H119A, and Apo-H94A-H96A - in 1.5 M sodium citrate tribasic dihydrate, 50 mM Tris pH 7.8.

As formerly reported for wild type hCA2, all crystals of the alanine variants belong to the monoclinic space group $P2_1$, with a single protein chain in the ASU; data collection and processing statistics are reported in Tables 2.6 and 2.7. The final models obtained for the variants in both apo and holo-state are of good quality, as indicated by their processing and refinement statistics (Tables 2.6 and 2.7).

	Apo-H4A	Apo-H94A	Apo-H96A	Apo-H119A	Apo-H94A-H96A
Precipitant	1.4 M Na_3 citrate *2H_2O, 50 mM TRIS pH 7.8	1.4 M Na_3 citrate *2H_2O, 50 mM TRIS pH 7.8	1.4 M Na_3 citrate *2H_2O, 50 mM TRIS pH 7.8	1.4 M Na_3 citrate *2H_2O, 50 mM TRIS pH 7.8	1.4 M Na_3 citrate *2H_2O, 50 mM TRIS pH 7.8
DATA COLLECTION STATISTICS					
Diffraction source	I04 (DLS)	I30B (ESRF)	I04 (DLS)	I04 (DLS)	I30B (ESRF)
Wavelength (Å)	0.9537	0.8731	0.9537	0.9537	0.976
Temperature (K)	100	100	100	100	100
Detector	Eiger2 XE 16M	EIGER2 9M	Eiger2 XE 16M	Eiger2 XE 16M	EIGER2 9M
Crystal-detector distance (mm)	168	80.9	169	169	80.9
Space group	$P2_1$	$P2_1$	$P2_1$	$P2_1$	$P2_1$
No. of subunits in ASU	1	1	1	1	1
a, b, c (Å)	42.03, 41.29, 72.12	42.39 41.46 72.39	42.32 41.42 72.16	42.34 41.53 73.41	42.49 41.69 72.59
β (°)	104.28	104.11	104.43	104.50	104.56
Resolution range (Å)	41.29-1.30 (1.32-1.30)	41.47-1.80 (1.84-1.80)	69.88 -1.25 (1.27 -1.25	70.11- 1.30 (1.32-1.30)	70.26-1.50 (1.53-1.50)
Total no. of reflections	400198 (19729)	153959 (8651)	454066(18487)	407209 (20942)	159143 (7990)
No. of unique reflections	57447 (2802)	22671 (1310)	67188 (3202)	60144 (3091)	39391 (1970)
Completeness (%)	97.3 (95.3)	99.2 (99.4)	100.0 (100.0)	100.0 (100.0)	99.4 (100.0)
Multiplicity	7.0 (7.0)	6.8 (6.6)	6.8 (5.6)	6.8 (6.8)	4.0 (4.1)
(I / σ(I))	29.1 (5.9)	9.6 (2.7)	14.4 (1.8)	9.3 (1.5)	8.0 (1.6)
CC(1/2)	0.99 (0.97)	0.99 (0.34)	1.0 (0.7)	0.99 (0.58)	0.99 (4.1)
R_{meas}	0.036 (0.23)	0.16 (1.55)	0.059 (0.952)	0.121 (1.415)	0.131 (1.109)
Overall B factor from Wilson plot ($Å^2$)	18.5	19.4	12.4	9.1	11.1
REFINEMENT STATISTICS					
Resolution range (Å)	40.77-1.30 (1.33-1.30)	41.14-1.68 (1.72-1.68)	69.88-1.25 (1.28-1.25)	70.11-1.30 (1.33-1.30)	41.16-1.50 (1.53-1.50)
Completeness (%)	97.0 (95.1)	98.66 (93.55)	100.0 (100.0)	99.9 (99.8)	99.26 (99.97)
No. of reflections, working set	54676 (2913)	26384 (1838)	63812 (4717)	57223 (4156)	37312 (2763)
No. of reflections, test set	2750 (222)	1478 (105)	3358 (243)	2863 (227)	2062 (138)
Final R_{cryst}	0.1909 (0.237)	0.1673 (0.269)	0.1808 (0.265)	0.1880 (0.270)	0.1817 (0.278)
Final R_{free}	0.2105 (0.258)	0.2077 (0.272)	0.2060 (0.272)	0.2124 (0.268)	0.2045 (0.293)
No. of non-H atoms					
Protein	260	260	261	260	260
Ligand	-	-	-	-	-
Ion	-	-	-	-	
Water	352	185	337	367	249
Total	612	445	598	627	509
R.m.s. deviations bonds (Å)	0.003	0.004	0.003	0.003	0.003
Angles (°)	1.071	1.176	1.067	1.081	1.109

Average B factor ($Å^2$)	12.25	21.9	14.26	11.68	13.65
Estimate error on coordinates based on R value (Å)	0.059	0.103	0.048	0.056	0.079
Ramachandran plot					
Most favored (%)	96.5	97.3	97.3	96.9	96.0
Allowed (%)	3.5	2.7	2.7	3.1	3.1

Table 2.6: Data collection, processing, and refinement statistic of structure Apo-H4A, Apo-H94A, Apo-H96A, Apo-H119A, and Apo-H94A-H96A. Values in parentheses are for the highest-resolution shell.

	Zn-H4A	**Zn-H94A**	**Zn-H96A**	**Zn-H119A**	**Zn-H94A-H96A**
Precipitant	1.4 M Na_3 citrate *$2H_2O$, 50 mM TRIS pH 7.8	1.4 M Na_3 citrate *$2H_2O$, 50 mM TRIS pH 7.8	1.4 M Na_3 citrate *$2H_2O$, 50 mM TRIS pH 7.8	1.4 M Na_3 citrate *$2H_2O$, 50 mM TRIS pH 7.8	1.4 M Na_3 citrate *$2H_2O$, 50 mM TRIS pH 7.8
DATA COLLECTION STATISTICS					
Diffraction source	I04 (DLS)	I04 (DLS)	P13 (PETRA III)	P13 (PETRA III)	P13 (PETRA III)
Wavelength (Å)	0.9537	0.9537	0.976	0.976	0.976
Temperature (K)	100	100	100	100	100
Detector	Eiger2 XE 16M	Eiger2 XE 16M	Eiger 16M	Eiger 16M	Eiger 16M
Crystal-detector distance (Å)	168.9	189.5	160.03	139.7	160.03
Space group	$P2_1$	$P2_1$	$P2_1$	$P2_1$	$P2_1$
No. of subunits in ASU	1	1	1	1	1
a, b, c (Å) β (°)	42.14, 41.23, 72.02 104.36	42.12 41.38 72.50 104.58	42.26 41.53 72.39 104.58	42.45 41.65 72.88 104.50	42.24 41.56 72.49 104.61
Resolution range (Å)	69.77-1.32 (1.32-1.30)	19.84-1.60 (1.63-1.60)	41.53 -1.50 (1.53 - 1.50	41.65- 1.50 (1.53-1.50)	70.14-1.37 (1.39-1.37)
Total no. of reflections	406758 (19319)	209612 (10510)	266231 (13292)	153173 (7937)	322012 (15639)
No. of unique reflections	59149 (1909)	30460 (1588)	37553 (1838)	38150 (1955)	50884 (2489)
Completeness (%)	100.0 (100.0)	94.6 (100.0)	96.2 (95.7)	96.1 (98.7)	99.2 (99.3)
Multiplicity	6.9 (6.06)	6.9 (6.6)	7.1 (7.2)	4.0 (4.1)	6.3 (6.3)
(I / σ(I))	15.7 (2.2)	14.1 (2.0)	11.7 (2.5)	7.2 (2.1)	8.3 (2.4)
CC (!/2)	1.0 (0.75)	0.99 (0.71)	0.99 (0.74)	0.99 (0.70)	0.99 (0.43)
R_{meas}	0.055 (0.959)	0.080 (1.01)	0.101 (0.906)	0.127 (0.701)	0.145 (0.785)
Overall B factor from Wilson plot ($Å^2$)	13.6	18.3	14.5	13.3	7.54
REFINEMENT STATISTICS					
Resolution range (Å)	69.77-1.30 (1.33-1.30)	19.85-1.60 (1.64-1.60)	35.75-1.50 (1.54-1.50)	35.89-1.50 (1.54-1.50)	70.14-1.37 (1.40-1.37)
Completeness (%)	99.9 (100.0)	94.6 (99.9)	95.7 (95.4)	95.88 (98.9)	98.8 (99.1)
No. of reflections, working set	56320 (4117)	28884 (2249)	35559 (2618)	36102 (2713)	49228 (3723)
No. of reflections, test set	2809 (217)	1563 (120)	1953 (136)	2008 (146)	1563 (0)
Final R_{cryst}	0.1767 (0.257)	0.1759 (0.248)	0.1704(0.238)	0.1748(0.270)	0.2083 (0.283)
Final R_{free}	0.1973 (0.269)	0.2108 (0.268)	0.1946(0.272)	0.1981(0.303)	0.2321 (0.00)

No. of non-H atoms					
Protein	260	260	260	260	260
Ligand	-	-	-	-	-
Ion	1	2	2	2	1
Water	278	232	234	225	305
Total	539	494	496	487	566
R.m.s. deviations bonds (Å)	0.003	0.006	0.003	0.005	0.005
Angles (°)	1.067	1.153	1.080	1.118	1.191
Average B factor (Å^2)	16.17	19.7	16.7	16.5	11.3
Estimate error on coordinates based on R value (Å)	0.053	0.099	0.078	0.079	0.070
Ramachandran plot					
Most favored (%)	96.9	96.5	97.7	96.9	96.5
Allowed (%)	3.1	3.5	2.3	3.1	3.5

Table 2.7: Data collection, processing, and refinement statistics of structure Zn-H4A, Zn-H94A, Zn-H96A, Zn-H119A, and Zn-H94A-H96A. Values in parentheses are for the highest-resolution shell.

2.3.4.1 Structural characterization of the alanine variants in the Apo-state

The structures of the alanine variants were solved at medium-high resolutions (ranging from 1.25Å to 1.80 Å, Table 2.6), providing detailed views of the active site configuration and the modifications induced upon mutations at the Zn1 and Zn2 sites. The comparison with the structure of the wild-type enzyme shows that the variants retain the same folding, as indicated by the low values of the rmds upon Cα matching, ranging from 0.08 to 0.10 Å. Thus, mutations at either the Zn1 or the Zn2 site do not affect the protein folding. Minor changes are observed in the active site area, mainly involving the solvent network. Even so, the position of the water molecules meaningful for catalysis, W_{Zn}, the deep water and those close to Thr199 (also referred to as "W1" and "W2"), are almost perfectly overlapping in the structures of wild type hCA2 and the alanine variants. The main difference in the active site area concerns the 'in'/'out' orientation of the side chain of the proton shuttling residue, His64. In the apo-state of hCA2, His64 is flexible and both the 'in' and 'out' confirmations are observed, with the latter slightly more represented than the former (occupancy of 40% and 60%, respectively). On the other hand, the mutation of a histidine into an alanine at the Zn1 site favours the 'out' orientation of His64 (Figure 2.31A). Indeed, in the structures of the H94A, H96A, and H119A variants, His64 is fully rotated outside the catalytic cavity (Figure 2.31 B, C, D). The same configuration is also observed in the structure of the apo-state of the double variant H94A-H96A (Figure 2.31E). In all structures, the 'out' orientation of His64 is stabilized by a water-mediated interaction with His4 on the N-terminal tail of the enzyme. It is worth noting that this water

mediated interaction is not pivotal to keeping His64 in the ‘out’ orientation. Indeed, the same ‘out’ configuration of His64 is also observed in the structure of the H4A variant. The replacement of His4 with an alanine residue at the Zn2 site does not affect the orientation of His64 but it allows the opening of the N-terminal tail that becomes more flexible (Figure 2.31 F).

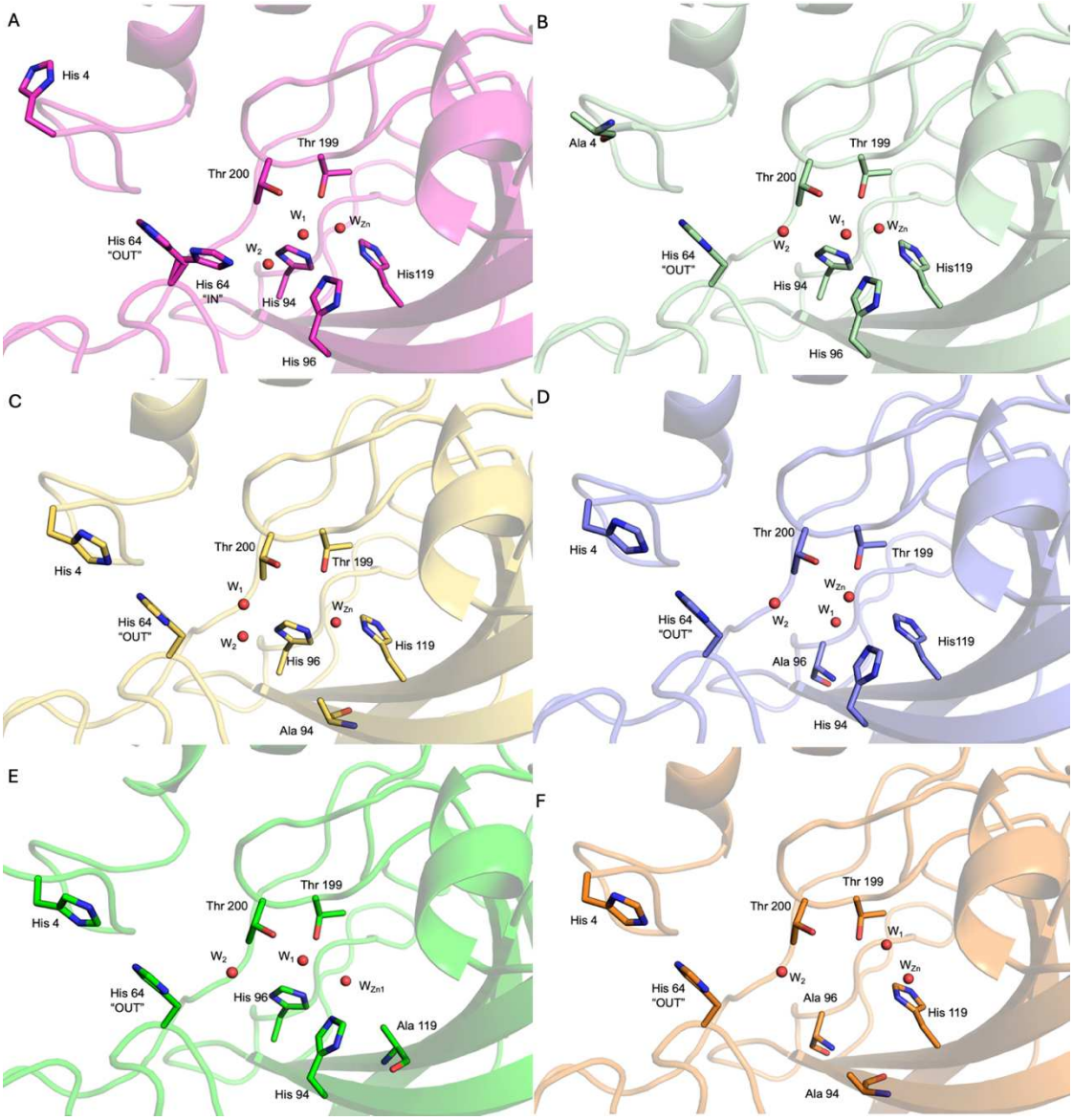

Figure 2.31: (A) Interface view of APO-hCA2 variant in cartoon, and the interacting residues in sticks in magenta. (B) Interface view of APO- H4A variant in cartoon, and the interacting residues in sticks in tints. (C) Interface view of APO-H94A variant in cartoon, and the interacting residues in sticks in yellow. (D) Interface view of APO-H96A variant in cartoon, and the interacting residues in sticks in violet. (E) Interface view of APO-H96A variant in cartoon, and the interacting residues in sticks in green. (F) Interface view of APO-H94A-H96A variant in cartoon, and the interacting residues in sticks in orange. The key water molecules are represented as red spheres.

2.3.4.2. Structural characterization of the alanine variants in the holo-state with Zn^{2+} ions

Former investigations performed on wild type hCA2, validated the application of both soaking and co-crystallization approaches for characterizing the holo-state of the enzyme; indeed, the same structural results were obtained with both methods (section 2.3.3). The holo-state of the alanine variants was investigated by exposing the apo-enzyme to an excess of Zn^{2+} ions, to allow populating all metal binding sites. The structures of the variants were characterized at medium-high resolution (ranging from 1.30Å to 1.60 Å, Tables 2.7.), showing detailed views of the changes occurring in the catalytic cavity upon each mutation.

The single variants at the Zn1 site displayed peculiar behaviours since each specific His to Ala replacement differently affected the ability of the enzyme to retain zinc binding at this site. In the H96A variant (Figure 2.32 C), the Zn^{2+} ion was observed to bind at the Zn1 site to a 60% occupancy in nearly the same position as Zn1 in hCA2; the comparison between the structures shows a shift of ~1.1 Å in the Zn^{2+} position. Therefore, the position of the water/hydroxide species shifts in the cavity, being positioned ~2.3 Å away from its original site. Upon mutation of His96 into an alanine, a water molecule occupies the vacancy in the metal coordination sphere that retains a tetrahedral geometry. Despite these changes, the metal binding distances with His94 and His119 and the water/hydroxide species are retained (within experimental errors). The shift of the water/hydroxide nucleophile from its original position together with the modification of the Zn1 coordination sphere, explains the reduced catalytic activity of the variant. Similar changes at the Zn1 site were also observed in the H119A variant, where the Zn^{2+} ion keeps its tetrahedral coordination sphere, being coordinated by His94, His96 the water/hydroxide species, and a water molecule. As formerly described for the H96A variant, a water molecule replaces the vacancy in the Zn^{2+} coordination sphere produced by the His to Ala mutation at residue 119. In the H119A variant (Figure 2.32 E) the Zn1 ion moves from its original position by ~0.8 Å, together with the water/hydroxide species shifting by ~1.7 Å. The population of Zn1 has slightly increased in the H119A mutant, reaching an occupancy of 80-90%. As for the H96A variant, the displacement of the metal and nucleophile species and the modification of the Zn1 coordination sphere resulted in a lower catalytic activity measured for the variant. The third single mutant at the Zn1 site is the H94A variant. In this variant (Figure 2.32 C), the binding of the Zn1 ion is more labile, and the population of this site is estimated to only 30-40%. Nonetheless, the position of the metal ion matches the Zn1 site observed in the wild-type enzyme. As formerly described for the other variants, a water molecule replaces

the His94 imidazole nitrogen, coordinating the metal ion together with His96 and His119. The increased lability of this modified site reasonably explains the lack of the water/hydroxide species, which is not observed in the structure of the H94A variant. Even so the variant retains a detectable residual activity, being able to perform the esterase reaction to a very low extent (2.3.4). To fully prevent zinc binding at the Zn1 site, the double variant H94A-H96A (Figure 2.32 F) was generated and investigated, demonstrating that upon mutation of both metal-anchoring residues the enzyme completely loses the ability to coordinate Zn^{2+} ions.

All variants at the Zn1 site share the same ability to bind Zn^{2+} ions at the accessory Zn2 site. Despite the meaningful differences at the catalytic centre, the external area of the active site is fully conserved, showing the Zn^{2+} ion coordinated by His4, His64, and two water molecules. The position of the Zn^{2+} ion perfectly matches the site observed in the wild-type enzyme, but the population is slightly increased in all variants, reaching a 50-70% occupancy. The increased population of the Zn2 site is accompanied by a stable orientation of His64 whose side chain points in the 'out' direction in all variant structures.

To deeply investigate the Zn2 site, the H4A variant (Figure 2.32 B) was further studied. The configuration of the catalytic cavity and the Zn1 site were not perturbed by the mutation. In fact, the structure of the H4A mutant perfectly matches that of the wild-type enzyme at this site. Upon replacement of His4 by an Ala, the Zn^{2+} ion is no longer bound at the accessory site, increasing the flexibility of His64 which is observed in both 'in' and 'out' configurations (60% and 40% occupancy, respectively). The catalytic activity of the variant is not affected by the mutation, indeed the variant resulted in having catalytic rates comparable to the wild-type enzyme.

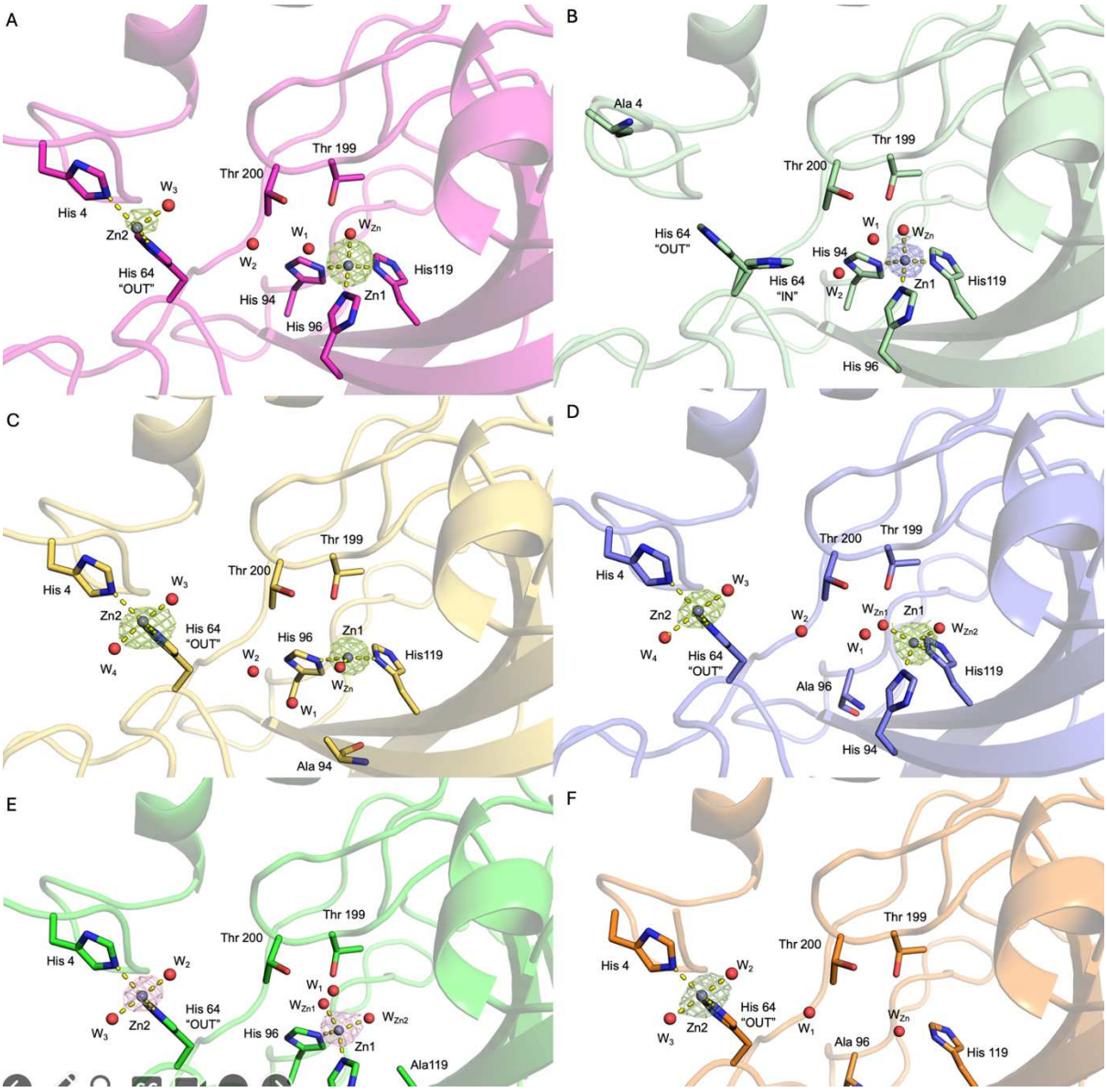

Figure 2.32: (A) Interface view of Zn-hCA2 variant in cartoon, and the interacting residues in sticks in magenta. (B) Interface view of Zn- H4A variant in cartoon, and the interacting residues in sticks in tints. (C) Interface view of Zn-H94A variant in cartoon, and the interacting residues in sticks in yellow. (D) Interface view of Zn-H96A variant in cartoon, and the interacting residues in sticks in violet. (E) Interface view of Zn-H96A variant in cartoon, and the interacting residues in sticks in green. (F) Interface view of Zn-H94A-H96A variant in cartoon, and the interacting residues in sticks in orange. The key water molecules are represented as red spheres. Zinc ions (grey spheres) are surrounded by the anomalous difference map) contoured at 5.0 σ. Coordination bonds are illustrated as yellow dashed lines.

2.4 Conclusions

This study has provided new insights into the regulation of the catalytic site of human Carbonic Anhydrase II (hCA2) and the crucial role of its two zinc-binding sites. By combining site-directed mutagenesis, X-ray crystallography, enzymatic kinetics, and calorimetric titration, we have characterized the structural and functional consequences of mutations at key residues within the catalytic site.

The generated variants, carrying mutations at the Zn1 coordination residues (H94A, H96A, H119A, and the double mutant H94A-H96A), exhibited a significant impairment in their ability to bind and retain the Zn^{2+} ion. This loss of coordination resulted in alterations in the active site geometry and a drastic reduction in catalytic activity, leading to complete inactivation in the H96A and H119A mutants. In particular, the H94A variant, despite displaying a less stable zinc coordination, retained residual enzymatic activity, suggesting a partial maintenance of catalytic function. The double H94A-H96A mutation confirmed the essential role of these two residues in Zn^{2+} coordination and enzyme catalysis, leading to a complete loss of function. On the other hand, mutations at the Zn2 site (such as H4A) did not significantly affect the enzyme's catalytic efficiency, indicating that this secondary zinc site plays a minor role in catalysis. However, calorimetric titration experiments revealed complex and distinct thermodynamic behaviours for each variant, particularly in the H94A, H96A, and H119A mutants, which displayed multiple binding events and altered heat exchange patterns. These findings suggest that while the primary Zn1 site is essential for enzymatic function, the secondary Zn2 site may still contribute to structural stability or allosteric regulation. Overall, this study highlights the intricate relationship between zinc coordination and enzymatic activity in hCA2.

Understanding these mechanisms at the molecular level could provide valuable information for the development of new artificial enzymes based on the model of carbonic anhydrase. Kinetic assays revealed that H96 and H119 could be indispensable for catalysis, while H94 may play an essential role in substrate binding and active site stability, as evidenced by the significant loss of catalytic efficiency in the H94A variant. These findings underscore the intricate interplay between zinc coordination, substrate binding, and enzymatic catalysis.

The results provide valuable insights into the functional dynamics of hCA2 and lay a foundation for further studies on the mechanisms of substrate binding and zinc coordination. They also offer promising avenues for the design and engineering of molecules with enhanced affinity and specificity for carbonic anhydrases in different fields.

2.5 References

(1) Crichton, R. R. Zinc – Lewis Acid and Gene Regulator. In *Biological Inorganic Chemistry*; Elsevier, 2012; pp 229–246. https://doi.org/10.1016/B978-0-444-53782-9.00012-7.

(2) McCall, K. A.; Huang, C.; Fierke, C. A. Function and Mechanism of Zinc Metalloenzymes. *J. Nutr.* **2000**, *130* (5), 1437S-1446S. https://doi.org/10.1093/jn/130.5.1437S.

(3) Holm, R. H.; Kennepohl, P.; Solomon, E. I. Structural and Functional Aspects of Metal Sites in Biology. *Chem. Rev.* **1996**, *96* (7), 2239–2314. https://doi.org/10.1021/cr9500390.

(4) Hernick, M.; Fierke, C. A. Zinc Hydrolases: The Mechanisms of Zinc-Dependent Deacetylases. *Arch. Biochem. Biophys.* **2005**, *433* (1), 71–84. https://doi.org/10.1016/j.abb.2004.08.006.

(5) Vallee, B. L.; Auld, D. S. New Perspective on Zinc Biochemistry: Cocatalytic Sites in Multi-Zinc Enzymes. *Biochemistry* **1993**, *32* (26), 6493–6500. https://doi.org/10.1021/bi00077a001.

(6) Auld, D. Auld, D.S. Zinc Coordination Sphere in Biochemical Zinc Sites. Biometals 14, 271-313. *Biometals Int. J. Role Met. Ions Biol. Biochem. Med.* **2001**, *14*, 271–313. https://doi.org/10.1023/A:1012976615056.

(7) Meldrum NU, R. FJ. Carbonic Anhydrase. Its Preparation and Properties. *J Physiol* **1993**, *80* (2), 113–219. https://doi.org/doi: 10.1113/jphysiol.1933.sp003077.

(8) Supuran, C. T. Structure and Function of Carbonic Anhydrases. *Biochem. J.* **2016**, *473* (14), 2023–2032. https://doi.org/10.1042/BCJ20160115.

(9) Supuran, C. T. Carbonic Anhydrase Inhibitors. *Bioorg. Med. Chem. Lett.* **2010**, *20* (12), 3467–3474. https://doi.org/10.1016/j.bmcl.2010.05.009.

(10) Nocentini, A.; Supuran, C. T.; Capasso, C. An Overview on the Recently Discovered Iota-Carbonic Anhydrases. *J. Enzyme Inhib. Med. Chem.* **2021**, *36* (1), 1988–1995. https://doi.org/10.1080/14756366.2021.1972995.

(11) Ozensoy Guler, O.; Capasso, C.; Supuran, C. T. A Magnificent Enzyme Superfamily: Carbonic Anhydrases, Their Purification and Characterization. *J. Enzyme Inhib. Med. Chem.* **2016**, *31* (5), 689–694. https://doi.org/10.3109/14756366.2015.1059333.

(12) Frost, S. C. Physiological Functions of the Alpha Class of Carbonic Anhydrases. In *Carbonic Anhydrase: Mechanism, Regulation, Links to Disease, and Industrial Applications*; Frost, S. C., McKenna, R., Eds.; Subcellular Biochemistry; Springer

Netherlands: Dordrecht, 2014; Vol. 75, pp 9–30. https://doi.org/10.1007/978-94-007-7359-2_2.

(13) Krungkrai, J.; Supuran, C. The Alpha-Carbonic Anhydrase from the Malaria Parasite and Its Inhibition. *Curr. Pharm. Des.* **2008**, *14* (7), 631–640. https://doi.org/10.2174/138161208783877901.

(14) Terentyev, V. V.; Trubitsina, L. I.; Shukshina, A. K.; Trubitsin, I. V.; Rudenko, N. N. Highly Active Carbonic Anhydrase of the Thylakoid Lumen of Chlamydomonas Reinhardtii. *Plants* **2024**, *14* (1), 55. https://doi.org/10.3390/plants14010055.

(15) Moroney, J. V.; Bartlett, S. G.; Samuelsson, G. Carbonic Anhydrases in Plants and Algae. *Plant Cell Environ.* **2001**, *24* (2), 141–153. https://doi.org/10.1111/j.1365-3040.2001.00669.x.

(16) Capasso, C.; Supuran, C. T. An Overview of the Alpha-, Beta- and Gamma-Carbonic Anhydrases from *Bacteria* : Can Bacterial Carbonic Anhydrases Shed New Light on Evolution of Bacteria? *J. Enzyme Inhib. Med. Chem.* **2015**, *30* (2), 325–332. https://doi.org/10.3109/14756366.2014.910202.

(17) Del Prete, S.; Vullo, D.; Ghobril, C.; Hitce, J.; Clavaud, C.; Marat, X.; Capasso, C.; Supuran, C. T. Cloning, Purification, and Characterization of a β-Carbonic Anhydrase from Malassezia Restricta, an Opportunistic Pathogen Involved in Dandruff and Seborrheic Dermatitis. *Int. J. Mol. Sci.* **2019**, *20* (10), 2447. https://doi.org/10.3390/ijms20102447.

(18) Syrjänen, L.; Tolvanen, M.; Hilvo, M.; Olatubosun, A.; Innocenti, A.; Scozzafava, A.; Leppiniemi, J.; Niederhauser, B.; Hytönen, V. P.; Gorr, T. A.; Parkkila, S.; Supuran, C. T. Characterization of the First Beta-Class Carbonic Anhydrase from an Arthropod (Drosophila Melanogaster) and Phylogenetic Analysis of Beta-Class Carbonic Anhydrases in Invertebrates. *BMC Biochem.* **2010**, *11* (1), 28. https://doi.org/10.1186/1471-2091-11-28.

(19) Del Prete, S.; Vullo, D.; De Luca, V.; Supuran, C. T.; Capasso, C. Biochemical Characterization of the δ-Carbonic Anhydrase from the Marine Diatom *Thalassiosira Weissflogii* , TweCA. *J. Enzyme Inhib. Med. Chem.* **2014**, *29* (6), 906–911. https://doi.org/10.3109/14756366.2013.868599.

(20) Del Prete, S.; Vullo, D.; Fisher, G. M.; Andrews, K. T.; Poulsen, S.-A.; Capasso, C.; Supuran, C. T. Discovery of a New Family of Carbonic Anhydrases in the Malaria Pathogen Plasmodium Falciparum —The η-Carbonic Anhydrases. *Bioorg. Med. Chem. Lett.* **2014**, *24* (18), 4389–4396. https://doi.org/10.1016/j.bmcl.2014.08.015.

(21) Supuran, C. T. Carbonic Anhydrases: Novel Therapeutic Applications for Inhibitors and Activators. *Nat. Rev. Drug Discov.* **2008**, *7* (2), 168–181. https://doi.org/10.1038/nrd2467.

(22) Lehenkari, P.; Hentunen, T. A.; Laitala-Leinonen, T.; Tuukkanen, J. Carbonic Anhydrase II Plays a Major Role in Osteoclast Differentiation and Bone Resorption by Effecting the Steady State Intracellular pH and Ca2*2*.

(23) Vullo, D.; Innocenti, A.; Nishimori, I.; Pastorek, J.; Scozzafava, A.; Pastoreková, S.; Supuran, C. T. Carbonic Anhydrase Inhibitors. Inhibition of the Transmembrane Isozyme XII with Sulfonamides—a New Target for the Design of Antitumor and Antiglaucoma Drugs? *Bioorg. Med. Chem. Lett.* **2005**, *15* (4), 963–969. https://doi.org/10.1016/j.bmcl.2004.12.053.

(24) Fisher, S. Z.; Maupin, C. M.; Budayova-Spano, M.; Govindasamy, L.; Tu, C.; Agbandje-McKenna, M.; Silverman, D. N.; Voth, G. A.; McKenna, R. Atomic Crystal and Molecular Dynamics Simulation Structures of Human Carbonic Anhydrase II: Insights into the Proton Transfer Mechanism ·. *Biochemistry* **2007**, *46* (11), 2930–2937. https://doi.org/10.1021/bi062066y.

(25) Kim, C. U.; Song, H.; Avvaru, B. S.; Gruner, S. M.; Park, S.; McKenna, R. Tracking Solvent and Protein Movement during CO_2 Release in Carbonic Anhydrase II Crystals. *Proc. Natl. Acad. Sci.* **2016**, *113* (19), 5257–5262. https://doi.org/10.1073/pnas.1520786113.

(26) Avvaru, B. S.; Busby, S. A.; Chalmers, M. J.; Griffin, P. R.; Venkatakrishnan, B.; Agbandje-McKenna, M.; Silverman, D. N.; McKenna, R. Apo-Human Carbonic Anhydrase II Revisited: Implications of the Loss of a Metal in Protein Structure, Stability, and Solvent Network ·. *Biochemistry* **2009**, *48* (31), 7365–7372. https://doi.org/10.1021/bi9007512.

(27) Christianson, D. W.; Fierke, C. A. Carbonic Anhydrase: Evolution of the Zinc Binding Site by Nature and by Design. *Acc. Chem. Res.* **1996**, *29* (7), 331–339. https://doi.org/10.1021/ar9501232.

(28) Andring, J. T.; Kim, C. U.; McKenna, R. Structure and Mechanism of Copper–Carbonic Anhydrase II: A Nitrite Reductase. *IUCrJ* **2020**, *7* (2), 287–293. https://doi.org/10.1107/S2052252520000986.

(29) Kiefer, L. L.; Paterno, S. A.; Fierke, C. A. Hydrogen Bond Network in the Metal Binding Site of Carbonic Anhydrase Enhances Zinc Affinity and Catalytic Efficiency. *J. Am. Chem. Soc.* **1995**, *117* (26), 6831–6837. https://doi.org/10.1021/ja00131a004.

(30) Lindskog, S.; COLEMANt, J. E. The Catalytic Mechanism of Carbonic Anhydrase. *Proc Nat Acad Sci USA* **1973**.

(31) Kim, J. K.; Lee, C.; Lim, S. W.; Adhikari, A.; Andring, J. T.; McKenna, R.; Ghim, C.-M.; Kim, C. U. Elucidating the Role of Metal Ions in Carbonic Anhydrase Catalysis. *Nat. Commun.* **2020**, *11* (1), 4557. https://doi.org/10.1038/s41467-020-18425-5.

(32) Fisher, Z.; Hernandez Prada, J. A.; Tu, C.; Duda, D.; Yoshioka, C.; An, H.; Govindasamy, L.; Silverman, D. N.; McKenna, R. Structural and Kinetic Characterization of Active-Site Histidine as a Proton Shuttle in Catalysis by Human Carbonic Anhydrase II. *Biochemistry* **2005**, *44* (4), 1097–1105. https://doi.org/10.1021/bi0480279.

(33) Nair, S. K.; Christianson, D. W. Unexpected pH-Dependent Conformation of His-64, the Proton Shuttle of Carbonic Anhydrase I.

(34) Kiefer, L. L.; Fierke, C. A. Functional Characterization of Human Carbonic Anhydrase II Variants with Altered Zinc Binding Sites.

(35) Ippolito, J. A.; Christianson, D. W. Structural Consequences of Redesigning a Protein-Zinc Binding Site.

(36) Hunt, J. B.; Rhee, M.-J.; Storm, C. B. A Rapid and Convenient Preparation of Apocarbonic Anhydrase. *Anal. Biochem.* **1977**, *79* (1–2), 614–617. https://doi.org/10.1016/0003-2697(77)90444-4.

(37) Håkansson, K.; Carlsson, M.; Svensson, L. A.; Liljas, A. Structure of Native and Apo Carbonic Anhydrase II and Structure of Some of Its Anion-Ligand Complexes. *J. Mol. Biol.* **1992**, *227* (4), 1192–1204. https://doi.org/10.1016/0022-2836(92)90531-N.

(38) Kabsch, W. *XDS*. *Acta Crystallogr. D Biol. Crystallogr.* **2010**, *66* (2), 125–132. https://doi.org/10.1107/S0907444909047337.

(39) Evans, P. Scaling and Assessment of Data Quality. *Acta Crystallogr. D Biol. Crystallogr.* **2006**, *62* (1), 72–82. https://doi.org/10.1107/S0907444905036693.

(40) Potterton, L.; Agirre, J.; Ballard, C.; Cowtan, K.; Dodson, E.; Evans, P. R.; Jenkins, H. T.; Keegan, R.; Krissinel, E.; Stevenson, K.; Lebedev, A.; McNicholas, S. J.; Nicholls, R. A.; Noble, M.; Pannu, N. S.; Roth, C.; Sheldrick, G.; Skubak, P.; Turkenburg, J.; Uski, V.; Von Delft, F.; Waterman, D.; Wilson, K.; Winn, M.; Wojdyr, M. *CCP* 4 *i* 2: The New Graphical User Interface to the *CCP* 4 Program Suite. *Acta Crystallogr. Sect. Struct. Biol.* **2018**, *74* (2), 68–84. https://doi.org/10.1107/S2059798317016035.

(41) Vagin, A.; Teplyakov, A. Molecular Replacement with *MOLREP*. *Acta Crystallogr. D Biol. Crystallogr.* **2010**, *66* (1), 22–25. https://doi.org/10.1107/S0907444909042589.

(42) Murshudov, G. N.; Skubák, P.; Lebedev, A. A.; Pannu, N. S.; Steiner, R. A.; Nicholls, R. A.; Winn, M. D.; Long, F.; Vagin, A. A. *REFMAC* 5 for the Refinement of Macromolecular Crystal Structures. *Acta Crystallogr. D Biol. Crystallogr.* **2011**, *67* (4), 355–367. https://doi.org/10.1107/S0907444911001314.

(43) Emsley, P.; Lohkamp, B.; Scott, W. G.; Cowtan, K. Features and Development of *Coot*. *Acta Crystallogr. D Biol. Crystallogr.* **2010**, *66* (4), 486–501. https://doi.org/10.1107/S0907444910007493.

(44) Winn, M. D.; Ballard, C. C.; Cowtan, K. D.; Dodson, E. J.; Emsley, P.; Evans, P. R.; Keegan, R. M.; Krissinel, E. B.; Leslie, A. G. W.; McCoy, A.; McNicholas, S. J.; Murshudov, G. N.; Pannu, N. S.; Potterton, E. A.; Powell, H. R.; Read, R. J.; Vagin, A.; Wilson, K. S. Overview of the *CCP* 4 Suite and Current Developments. *Acta Crystallogr. D Biol. Crystallogr.* **2011**, *67* (4), 235–242. https://doi.org/10.1107/S0907444910045749.

(45) Williams, C. J.; Headd, J. J.; Moriarty, N. W.; Prisant, M. G.; Videau, L. L.; Deis, L. N.; Verma, V.; Keedy, D. A.; Hintze, B. J.; Chen, V. B.; Jain, S.; Lewis, S. M.; Arendall, W. B.; Snoeyink, J.; Adams, P. D.; Lovell, S. C.; Richardson, J. S.; Richardson, D. C. MolProbity: More and Better Reference Data for Improved All-atom Structure Validation. *Protein Sci.* **2018**, *27* (1), 293–315. https://doi.org/10.1002/pro.3330.

(46) Janson, G.; Zhang, C.; Prado, M. G.; Paiardini, A. PyMod 2.0: Improvements in Protein Sequence-Structure Analysis and Homology Modeling within PyMOL. *Bioinformatics* **2017**, *33* (3), 444–446. https://doi.org/10.1093/bioinformatics/btw638.

(47) Scozzafava, A.; Supuran, C. T. Hydroxyurea Is a Carbonic Anhydrase Inhibitor. *Bioorg. Med. Chem.* **2003**, *11* (10), 2241–2246. https://doi.org/10.1016/S0968-0896(03)00112-3.

(48) Y. Pocket; Meany, J. E. The Catalytic Versatility of Erythrocyte Carbonic Anhydrase. I. Kinetic Studies of the Enzyme-Catalyzed Hydration of Acetaldehyde. *Biochemistry* **1965**, *4* (11), 2535–2541.

(49) Coleman, J. E. Mechanism of Action of Carbonic Anhydrase. *J. Biol. Chem.* **1967**, *242* (22), 5212–5219. https://doi.org/10.1016/S0021-9258(18)99413-5.

(50) Song, H.; Wilson, D. L.; Farquhar, E. R.; Lewis, E. A.; Emerson, J. P. Revisiting Zinc Coordination in Human Carbonic Anhydrase II. *Inorg. Chem.* **2012**, *51* (20), 11098–11105. https://doi.org/10.1021/ic301645j.

(51) Alexander, R. S.; Kiefer, L. L.; Fierke, C. A.; Christianson, D. W. Engineering the Zinc Binding Site of Human Carbonic Anhydrase II: Structure of the His-94.Fwdarw.Cys Apoenzyme in a New Crystalline Form. *Biochemistry* **1993**, *32* (6), 1510–1518. https://doi.org/10.1021/bi00057a015.

Chapter 3

Structural and functional studies on hCA2 derivatives with various transition metals

3.1 Introduction: substituting hCA2 with non-native metals

Metals are essential in a variety of biological processes that are vital for life and exert a fundamental role in the structure and function of metalloproteins (*i.e.*, metalloenzymes and ion channels) as well as other biologically relevant macromolecules (*i.e.*, ribosomes and nucleic acids). Due to their versatile chemical reactivity, metal ions are crucial for catalysing some of the most important biochemical reactions observed in nature, such as hydrolysis and electron transfer in redox processes.[1] In this context, protein-bound metal sites in which one or more metal cations coordinate protein side chains and external ligands are particularly interesting. Their metal binding site, particularly the first coordination sphere of the cation, is finely tuned to exert specific biological functions through a complex system of docking residues and a network of water molecules. The specificity of the metal-binding region determines the protein activity and selectivity, and any modification and perturbation in this region often determine radical changes in the behaviour of metalloproteins.[2]

When metalloenzymes are substituted with non-native metal ions, this can modulate (increasing, decreasing, or abolishing) their natural activity or change radically their function.[3] Even small changes in the nature of the substituted ions (*e.g.,* ionic charge, size, mass, redox potential, electronic configuration, or coordination geometry) can result in significant changes in enzymatic properties.[4,5] Among the various types of metalloenzymes, carbonic anhydrases are particularly amenable to metal substitution. As we saw in the previous chapter, the Zn^{2+} cofactor in the CA active site mediates a complex catalytic mechanism. Thus, a systematic study on replacement of the native metal with other divalent cations can shine a new light on the structure-function relationships of this enzyme. Some examples are discussed later in this chapter. Some biologically relevant transition metals display affinity to the catalytic Zn^{2+} binding site of CA. They could be taken up physiologically, as a consequence of their relative concentrations in a specific environment or displace the native cofactor. In either case, the resulting substitution produces a CA-metal adduct with altered catalytic properties, stability, and activity.[6] The study of these metal adducts provides valuable insights into the functional versatility of CA and the role of metal ion regulation of enzyme activity, with potential implications for both basic enzymology and applied biotechnology.

3.1.1 Acquired function of hCA2 adduct metals substituted

In the catalytic centre of hCA2, Zn^{2+}can be replaced by other transition metal divalent cations (Co^{2+}, Ni^{2+}, Cu^{2+}, Cd^{2+}, Fe^{2+}, and Mn^{2+}).[7] Such substitutions have been shown to alter the native activity of the enzyme,[8] offering valuable insights into the intricate relationship between the properties of metal ions and enzymatic function. Several studies demonstrated how replacing the metallic centre of hCA2, alters the catalytic properties of the enzyme and extends the function to novel reactions (Figure 3.1).[4,9,10,11,12,13]

An example of such metal substitution was provided by Andring *et al.,*[12] who demonstrated that Cu^{2+} could occupy the Zn^{2+} binding site of hCA2 and that the Cu^{2+}–CA2 variant acquires a novel nitrite reductase activity that leads to the conversion of NO_2^- into NO. Such reaction could be the diver of phenomena such as vasodilation and blood pressure regulation, which provide complexity to the physiological function and fine tuning of hCA2 and of CAs in general. The Cu^{2+}–CA2 variant coordinates the nitrite ion within the active site, connected through water molecules to a secondary Cu^{2+} within an N-terminal binding site.[14] This secondary Cu^{2+} is hypothesized to facilitate the electron transfer required for the nitrite reductase activity of Cu^{2+}–CA2.[15]

Another example of metal substitution was presented by Okrasa *et al.,*[11] who presented the biocatalytic reaction mediated by Mn^{2+}–CA2. This variant binds bicarbonate but is a poor catalyst for its dehydration to carbon dioxide. The metal substitution, in this case, converts the enzyme into a bicarbonate-dependent peroxidase which mediates one-electron oxidation using hydrogen peroxide,[16] whose physiological function is still unknown.[11] This adds CAs to the enzymes that can be repurposed to drive redox reactions of industrial relevance.

The peculiar reactivity of the enzyme and its capability to drive specific reactions are thus intimately connected with the electronic and coordination properties of the metal ion and the geometrical arrangement of the active site. Fine tuning of the metallic core and of specific side chains can be tailored to select and modulate enzymatic functions for therapeutic intervention and industrially relevant processes.

METALS	CATALYTIC ACTIVITY
Zn^{2+}	Carbon dioxide hydration 100% activity[4]
Co^{2+}	Carbon dioxide hydration 50% activity[4]
Cu^{2+}	Nitrite reductase[12]
Ni^{2+}	Carbon dioxide hydration 2% activity[4]
Mn^{2+}	Peroxidase activity[11]
Fe^{2+}	Carbon dioxide hydration 4% activity[13]
Hg^{2+}	No Carbon dioxide hydration activity observed[17]
Rh^{2+}	Stereoselective Hydrogenation of Olefins[18]
Cd^{2+}	No Carbon dioxide hydration activity observed[17]

Figure 3.1: The table summarizes catalytic activities, with Zn^{2+} showing the highest activity (100%) and other metals exhibiting reduced or alternative functions.

3.1.2 Metal coordination geometries in hCA2

Prior to this work, structural studies were published that unveiled the different coordination geometries of metals-substituted CAs.[19] In the presence of the native cation (Zn^{2+}), a tetragonal arrangement is provided by the three histidines (His94, His96, His119) and the catalytic water molecule (W_{Zn}), providing the best geometry to favour CO_2 conversion to bicarbonate (Figure 3.2 section A).

Similarly to Zn^{2+} (electronic configuration d^{10}), also Co^{2+} (d^7) has a strong preference for the tetrahedral geometry (Figure 3.2 section B) and, as such the overall structural features in the catalytic cavity of *h*CA2 are conserved, including the water in the first coordination sphere (W_{Co}). Differently, in the Cu^{2+}-substituted enzyme the metal cation (d^9) is coordinated by one additional water.[14,20,21] This distorts the catalytic site to a trigonal bipyramid (Figure 3.2 section C) where the two water molecules, are equidistant from the position naturally occupied by W_{Zn}. In this configuration, the CO_2 site is hindered by one of the waters abolishing the anhydrase catalytic activity. Another different arrangement is found in the presence of Ni^{2+} (d^8), which is highly stabilized by an octahedral geometry (Figure 3.2 section D). This is possible by recruiting a third water molecule in the active site. While in this new position, the water is still far away from the substrate, gas pressurization crystallographic studies demonstrate that the other two waters are replaced by two of oxygens from the bicarbonate ion. This stabilizes the substrate, which is thus unable to leave as part of the octahedral complex with Ni^{2+}.

As each of these metal ions can exert a long-range (~10 Å) electrostatic influence on the restructuring of the water network in the active site, the different coordination properties can impact both the initial proton transfer process or the product displacement at the end of the cycle.[4]

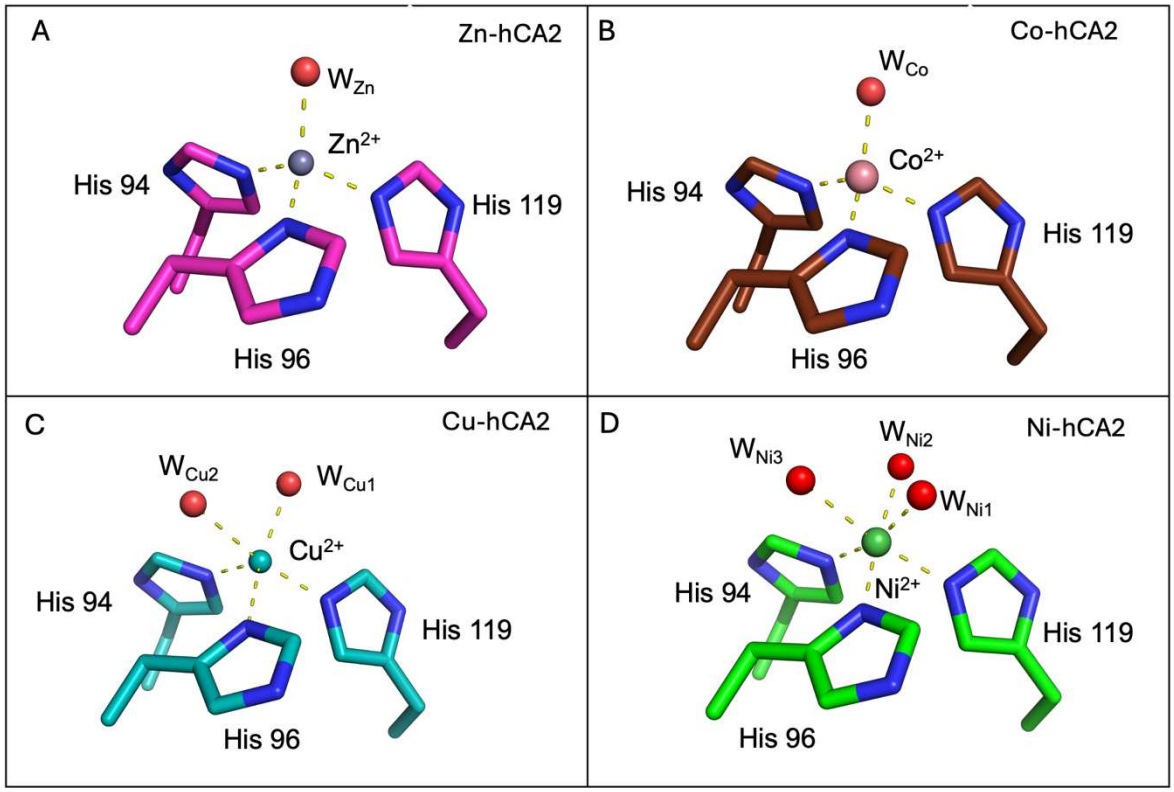

Figure 3.2: The different geometries for Zn^{2+} and Co^{2+}-substituted CA2: tetrahedral (A, B), trigonal bipyramidal for Cu^{2+}-CA2 (C), and octahedral Ni^{2+}-CA2 (D).

3.2 Materials and methods

3.2.1 Protein expression and purification and crystallization

Apo-hCA2 and the five alanine variants were obtained as described in Chapter 2 (sections 2.2.1-2.2.2). The enzyme and the alanine variants were crystallized using the sitting drop vapor-diffusion method at 8 °C. Drops were prepared by mixing equal volumes (2 µl) of protein (3-10 mg/ml, in 50 mM TRIS, pH 7.8) and precipitant solutions, either 1.4-1.5 M sodium citrate tribasic dihydrate, 50 mM TRIS pH 7.8,[19,21] or 2.7-2.8 M ammonium sulphate, 0.3 M NaCl, 50 mM TRIS pH 8-8.5, and equilibrated over a 200 µl reservoir. Crystal growth was observed in 2–3 days. Apo-hCA2 crystals were used for soaking experiments in which 1 µl of a 10 mM metal solution of $CoCl_2$, $CuCl_2$, $NiCl_2$, $MnCl_2$, or $(NH_4)_2Fe(SO_4)_2$ (Mohr's salt) was added to the crystallization drop. After 1 hour of free metal diffusion, crystals were washed in the cryoprotectant solution (precipitant added by 20% glycerol) and flash-frozen in liquid nitrogen. The same procedure was also applied to the crystals of the alanine variants (apo-state) that were soaked with Cu^{2+} ions for 2 hours. To characterize the enzyme-metal complexes, the co-crystallization approach was also attempted by incubating the apo-enzyme with a 5-time molar excess of each metal ion for 1 hour prior to the crystallization setup.

3.2.2 X-ray data collection, structure solution, and refinement

X-ray diffraction data were collected at 100 K, using synchrotron radiation at the DLS beamline I04 equipped with an Eiger 2XE 16M detector, the ESRF beamline ID30B, on an Eiger2 9M detector, and the Petra III beamline P13 on an Eiger 16M detector. Data were integrated with XDS[22] and scaled using AIMLESS[23] from the CCP4i2 suite.[24] Data collection and reduction statistics are shown in Tables 3.3 and 3.4. The crystals of hCA2 and its variants belong to the monoclinic space group $P2_1$. The structures were solved by molecular replacement with Molrep,[25] using the structure of hCA2 (PDB id 2CBA)[26] as the search model (metal ions and water molecules were preventively removed). The structures were refined using REFMAC[27] from the CCP4i2 suite. The molecular graphics software Coot[28] was used for visual inspection and manual modelling of the structures and to add water molecules. MAD collections were performed to demonstrate the presence of each metal ion in the structures of holo-hCA2 and its mutants. For the Co^{2+} complexes, data were collected at 13500 eV (high energy remote), 7760 eV, and 7550 eV (above and immediately below the Co K-edge, respectively). For the Cu^{2+} complexes, data were collected at 13500 eV

(high energy remote), 9100 eV, and 8800 eV (above and immediately below the Cu K-edge, respectively). For the Ni^{2+} complexes, data were collected at 13500 eV (high energy remote), 8370 eV, and 8230 eV (above and immediately below the Ni K-edge, respectively). For the Mn^{2+} complexes, data were collected at 13500 eV (high energy remote), 6590 eV, and 6450 eV (above and immediately below the Mn K-edge, respectively). For the Fe^{2+} complexes, data were collected at 13500 eV (high energy remote), 7200 eV, and 7050 eV (above and immediately below the Fe K-edge, respectively). Anomalous difference maps were calculated using FFT from the CCP4 suite.[29] Anomalous signals ranging between 5 and 30 σ were detected in all structures. The occupancies of metal ions were adjusted to keep their atomic displacement parameters close to those of nearby protein atoms in fully occupied sites. Final structural models were validated and checked with software Molprobity.[30] Final refinement statistics are reported in Tables 3.3 and 3.4 Figures were prepared using the molecular graphics software PyMol.[31]

3.2.3 Differential scanning fluorimetry (DSF) optimization

The hCA2-metal complexes for DSF experiments were prepared by supplementing the Apo-enzyme solution (1 mg/ml) with each metal ion to a final concentration of 0.1 mM for Zn^{2+}, Co^{2+}, Cu^{2+}, Ni^{2+}, Mn^{2+}, and Fe^{2+}.

To perform DSF assays, 10 µl of buffer (100 mM TRIS, pH 7.8; 100 mM MOPS, pH 7.4; 100 mM BES, pH 6.95; and 100 mM BIS-TRIS, pH 6.5) were transferred into a 96-well PCR plate. Subsequently, 10 µl of a mixture containing 4 µl of 5,000x SYPRO Orange in DMSO and 1 ml of protein-metal sample was added to each well. The PCR plates were sealed with Optical-Adhesive Covers (biosystems) and heated in a Stratagene Mx3005P RT-QPCR system (Agilent Technologies, La Jolla, CA, USA), with a linear temperature gradient from 25 °C to 95 °C using 1 °C step increments. The excitation and emission wavelengths for SYPRO Orange were set to 517 nm and 538 nm, respectively. The data were analysed using the MxPro version 4.10 QPCR software and the melting temperature (T_m) was derived from the experimental curve.

3.2.4 Isothermal titration calorimetry (ITC) analysis

ITC experiments were conducted on a MicroCal VP-ITC calorimeter at 25°C. The concentration of apo-hCA2 was determined by UV absorption at 280 nm (ε_{280} = 52,300 M^{-1} cm^{-1}). The experiment involved titrating apo-hCA2 (300 µl, 110 µM) with each metal solution (2.4 mM $CuCl_2$, 4.00 mM $NiCl_2$, 1.1 mM $MnCl_2$). All samples were prepared in a buffer containing 25 mM MOPS at pH 7.4.

The solutions were all buffered in 25 mM MOPS pH 7.4. The titration was performed with 17 injections, each with 2.4 µl volume in 4.8 s followed by 150 s re-equilibration time after each step. Control runs were performed for each assay by titrating metal in the buffer (25 mM MOPS pH 7.4) and used for background subtraction. ITC data were analysed using the MicroCal Origin software and used to obtain best-fit values for the stoichiometry (n), enthalpy (ΔH), and dissociation constant (K_d). Each experiment was performed in duplicate, and the best results are reported here.

3.2.5 Esterase kinetic assays

Kinetic assays were conducted on hCA2 metals variants measuring the esterase activity of hCA2 (representing that of the conversion of CO_2 to HCO_3^-) in an indirect way. This was performed by monitoring the hydrolysis of 4-nitrophenyl acetate[32,33] to 4-nitrophenol[4,34] over time. To perform the assay the apo-enzyme (1 mg/ml, ~34 µM) was supplemented with a large excess (2 mM) of the desired metal salts ($CoCl_2$, $CuCl_2$, $NiCl_2$, $MnCl_2$, or $(NH_4)_2Fe(SO_4)_2$ - Mohr's salt). Final reaction mixtures made of 1 mL assay buffer (0.8 mM 4-NPA, 3% acetone, 10 mM TRIS pH 7.8) and 0.2 mL of the enzyme. Reactions were performed at room temperature by monitoring at 400 nm for 2 min (data pitch of 10 seconds). Each kinetic assay was performed in duplicate.

3.3 Results and Discussion

3.3.1 Thermal Stability measurements

Differential Scanning Fluorimetry was employed to evaluate the stability of metal-substituted hCA2 in different buffers, to inform about the best conditions for enzymatic assays and crystallization experiments. Metal adducts including Co^{2+}, Cu^{2+}, Ni^{2+}, Mn^{2+}, Fe^{2+} produced the characteristic sigmoidal curves (Figure 3.3). The presence of the different metals was characterized by melting temperatures (T_m) between 48 °C and 56 °C, as determined by the maximum of the first derivative. The results, shown in Table 3.1, indicate that the various metal-substituted forms of hCA2 are stable in the tested buffers: TRIS (pH 7.8), MOPS (pH 7.4), BES (pH 6.95), and BIS-TRIS (pH 6.5).

	0.1 mM TRIS pH 7.8	**0.1 mM MOPS pH 7.4**	**0.1 mM BES pH 6.95**	**0.1 mM BIS-TRIS pH 6.5**
Zn-hCA2	49°C	46°C	48°C	54°C
Co-hCA2	55°C	54°C	56°C	53°C
Cu-hCA2	51°C	50°C	51°C	53°C
Ni-hCA2	49°C	47°C	50°C	47°C
Mn-hCA2	49°C	47°C	50°C	47°C
Fe-hCA2	45°C	47°C	49°C	47°C

Table 3.1: Melting temperatures (Tm) of various metal-substituted hCA2 in different buffer solutions.

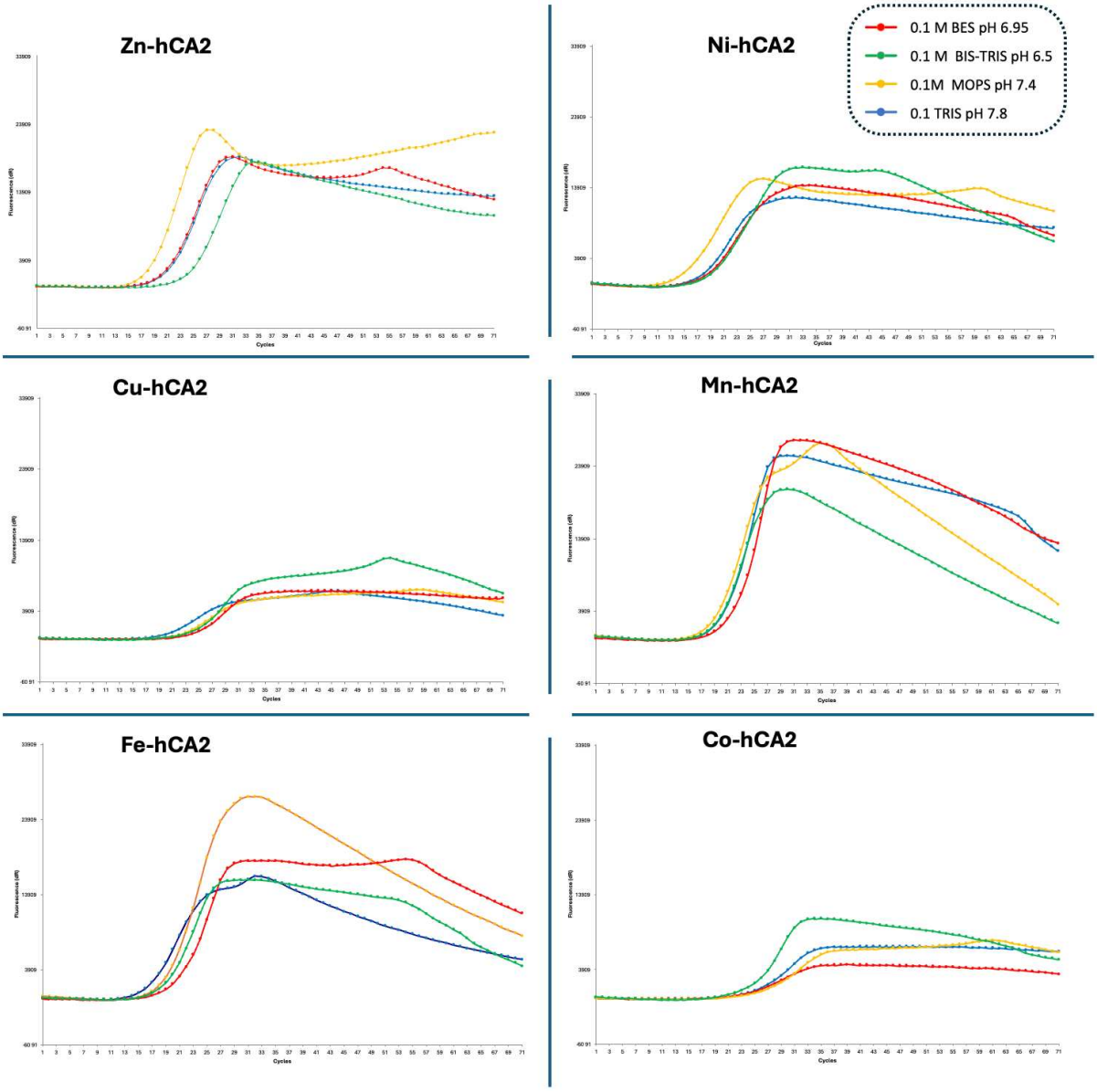

Figure 3.3: DSF melting curves of apo-hCA2 and its metal substituted versions (with Zn^{2+}, Co^{2+}, Cu^{2+}, Mn^{2+} and Fe^{2+}).

3.3.2 Thermodynamic characterization of hCA2 metal complexes

Once the best stabilizing buffer was identified for each metal, isothermal titration calorimetry was employed to determine the thermodynamic parameters characterizing the metal binding to hCA2. The experiments were conducted by titrating a solution of hCA2 with the salts described above. The best results, presented here, were obtained in a 25 mM MOPS pH 7.4 buffer, under the same experimental conditions described in Chapter 2.

Representative isothermal titration curves were successfully obtained for the binding of Cu^{2+}, Ni^{2+}, and Mn^{2+} ions to hCA2. The resulting data were analysed using both one-site and two-site binding models to assess the most accurate fit.

More challenging proved the measurements for the remaining metals. In the case of Co^{2+}, the curves are too noisy to allow a correct interpretation: this might be due to instrumental limitations, or the formation of metal-buffer adducts in the course of the analysis. As for Fe^{2+}, the difficulties are to be attributed to the oxidation of the metal in the experimental setup. To overcome this, future plans will involve degassing of the solutions and the transfer of the ITC instrument in an anaerobic chamber.

The ITC data for Cu^{2+} binding revealed high-affinity interactions between the enzyme and the copper ion, with dissociation constants (K_d) in the nanomolar range for two sets of sites (3.14×10^{-9} M and 2.68×10^{-10} M). The fitting models available in the analysis yielded stoichiometry values (n) of 3.35 and 1.10 under different conditions, suggesting variations in available binding sites based on the experimental setup or the specific metal ion (Figure 3.4 A). However, from a visual inspection of the curve, it is clear that the first inflection point is around n=1 and the second one is for n ~2, so a more accurate data treatment is ongoing.

Both reactions are exothermic and thermodynamically favoured (ΔG between -11.6 kcal/mol and -13.1 kcal/mol, Figure 3.4 B). Interestingly, the entropy contributions ($-T\Delta S$) are significantly different between the two bindings, indicating how one is entropy-driven (-11.2 kcal/mol), whereas for the second the reaction suffers from entropy penalty (+3.99 kcal/mol). One can hypothesize how the entropy-favoured reaction could correspond to the rearrangement of water molecules within the active site, while the other could be subject to an enthalpic gain due to the stabilization of the coordination of the secondary metallic centre. The thermodynamic parameters related to copper binding to the hCA2 are detailed in Table 3.2.

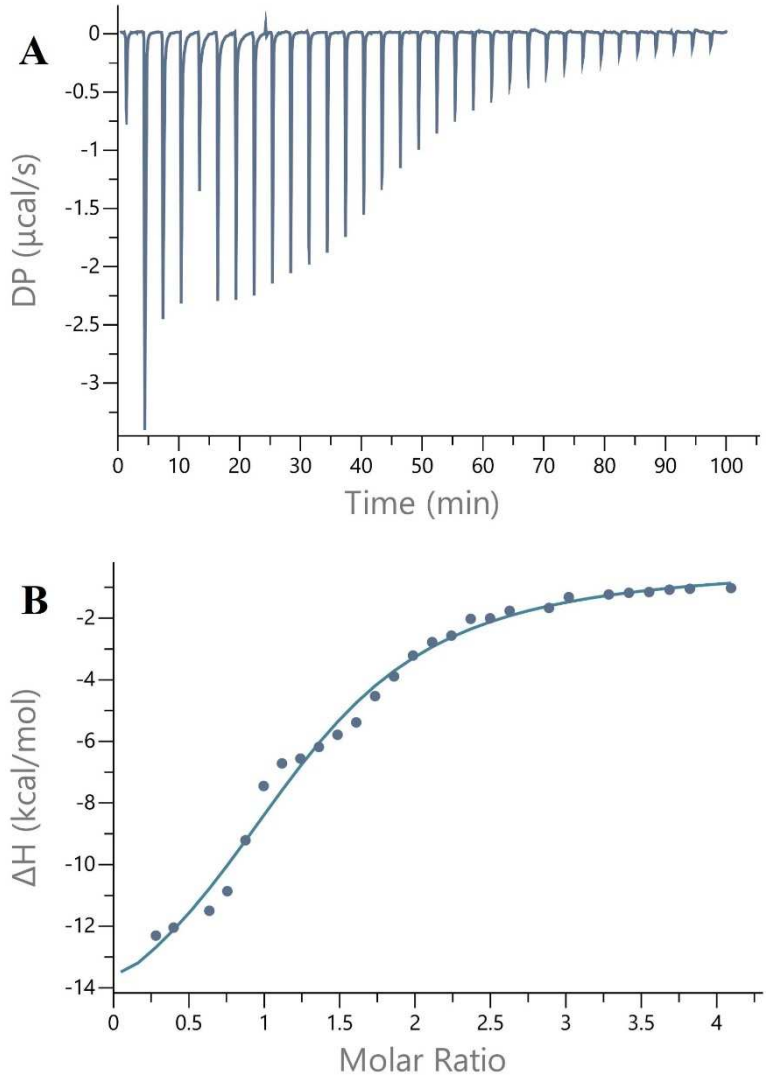

Figure 3.4: (A) ITC plot from the titration of 110 µM hCA2 (300 µl) with 17 × 2.4 µl injections of 10 mM of $CuCl_2$ in 25 mM MOPS at pH 7.4. (B) Integrated isotherm and best associated fit for a two-site binding model.

The case of Ni^{2+} binding, according to our ITC experiments, is sensibly different in that the curve is essentially monomodal. This allowed us to fit it with a single-site model with n~1 and a K_d = 35.1 × 10^{-6} M. The exothermic binding curve (Figure 3.5 A) is once again thermodynamically favoured (ΔG = -6.08 kcal/mol). In this case, however, the main driver is the enthalpy of the process (ΔH = -5.45 kcal/mol) while the entropic gain is minimal ($-T\Delta S$ = -0.625 kcal/mol). This suggests that any disordering effect on the water molecules within the catalytic site is probably compensated by the stabilization of the two additional Ni^{2+}-coordinating ones. The thermodynamic parameters related to nickel binding to the hCA2 are detailed in Table 3.2.

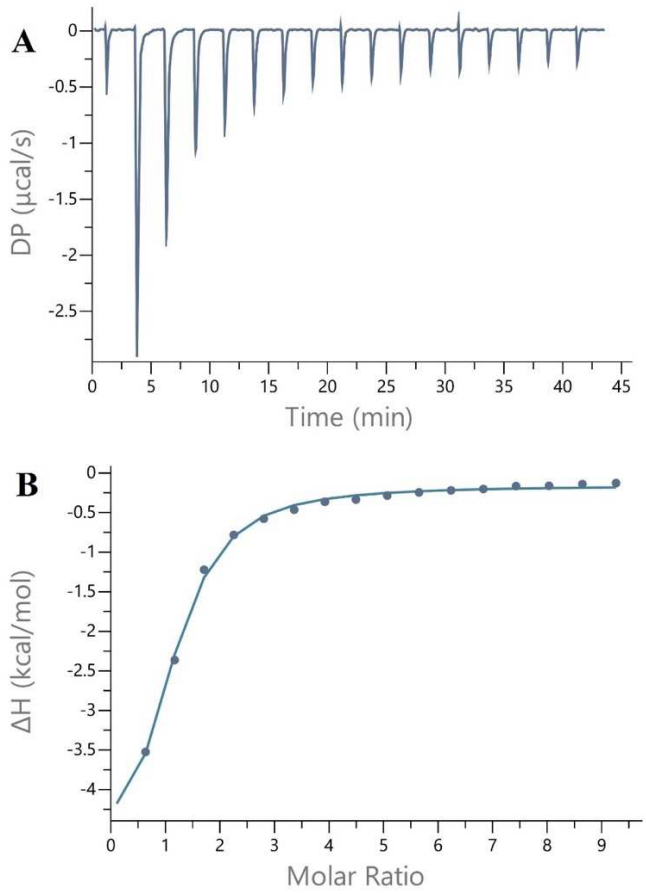

Figure 3.5: (A) ITC plot from the titration of 110 µM hCA2 (300 µl) with 17 × 2.4 µl injections of 10 mM of $NiCl_2$ in 25 mM MOPS at pH 7.4. (B) Integrated isotherm and best associated fit for a one-site binding model.

The third case of binding is exemplified by the ITC for hCA2 and Mn^{2+}. The reaction is still exothermic, but in this case the stoichiometry appears incomplete. Using a single-site fitting, an n~0.2 suggests only a partial occupancy of the metallic site, or a heterogeneous binding affinity across different positions. The mild enthalpic contribution (ΔH = −3.75 kcal/mol) is matched by a similar entropic gain ($-T\Delta S$ = −3.81 kcal/mol), bringing the total energetic stabilization upon binding to ΔG = −7.55kcal/mol (Figure 3.6). The thermodynamic parameters related to manganese binding to the hCA2 are detailed in Table 3.2.

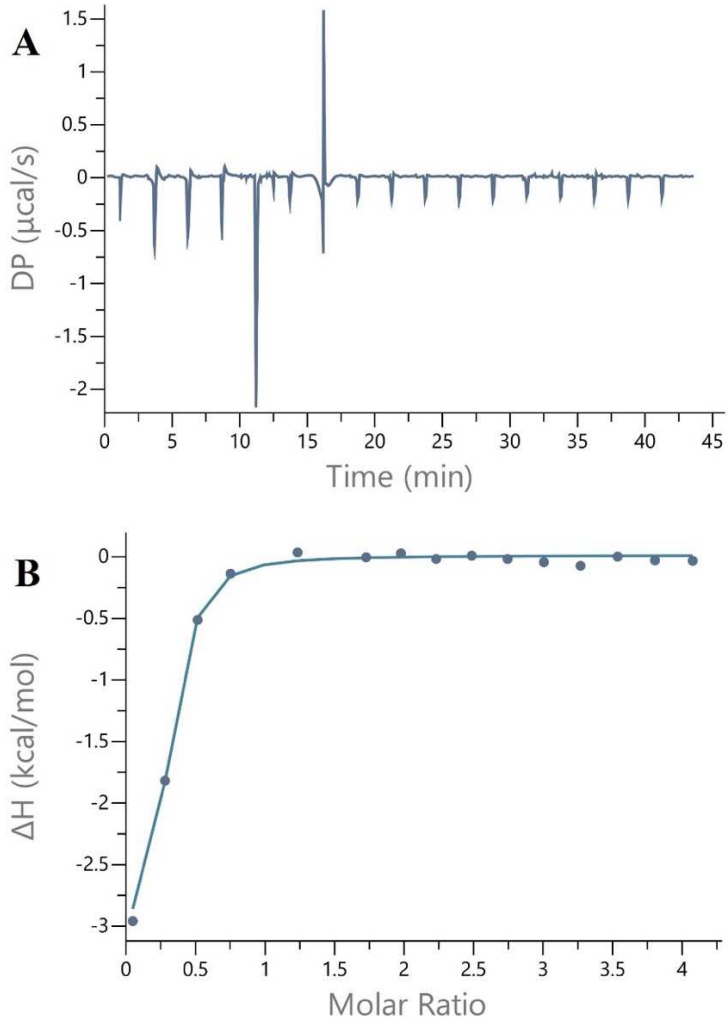

Figure 3.6: (A) ITC plot from the titration of 110 µM hCA2 (300 µl) with 17 × 2.4 µl injections of 10 mM of $MnCl_2$ in 25 mM MOPS at pH 7.4. (B) Integrated isotherm and best associated fit for a one-site binding model. Two outliers were excluded by the model and similar results were obtained from a duplicate experiment.

Protein	[Syr] (M)	[Cell] (M)	*n* (sites)	K_d (M)	ΔH (kcal/mol)	ΔG (kcal/mol)	$-T\Delta S$ (kcal/mol)
Cu-hCA2	$2.00e^{-3}$	$1.0e^{-4}$	3.35	$3.14e^{-9}$	-0.355	-11.6	-11.2
			1.10	$2.68e^{-10}$	-17.1	-13.1	3.99
Ni-hCA2	$5.00e^{-3}$	$1.1e^{-4}$	0.958	$35.1e^{-6}$	-5.45	-6.08	-0.625
Mn-hCA2	1.10^{-3}	55.0^{-4}	0.204	$2.91e^{-6}$	-3.75	-7.55	-3.81

Table 3.2: Fit values obtained to titration of Cu^{2+} in apo-hCA2, Ni^{2+} in apo-hCA2, and Mn^{2+}in apo-hCA2.

3.3.3 Esterase activity characterization

To assess the effect of metal substitutions to hCA2, a comparison of the activity of each variant is necessary. The release of p-nitrophenol upon hydrolysis of p-nitrophenyl acetate provided a quick and reliable colorimetric assay. The graph in Figure 3.7 presents the residual esterase activity of the different metal-substituted forms of hCA2 described here. Assigning a 100% value to the native (Zn^{2+}), the activity is partially retained in the presence of Co^{2+} (50 %). The other metals only display very low residual activity, which is compatible with the observations by other groups with respect to the alteration of catalytic properties. The case of Fe^{2+}, as mentioned for the ITC, could be slightly more complicated given the delicate redox equilibria involving this metal ion. Also in this case, we will follow up the measurements in anaerobic conditions, to rule out instrumental/setup artifacts.

Altogether this behaviour is in line with the results of Kim *et al,*[4] underlining the major role of metal coordination geometry, proving how tetrahedral complexes attainable with Zn^{2+}(d^{10}) and Co^{2+}(d^{7}) are only capable of retaining the CO_2 hydration function. As mentioned earlier, other types of enzymatic activity arise when the metal centre is modified and will be subject to further analysis when the most appropriate and reliable enzymatic and biophysical assays will be established.

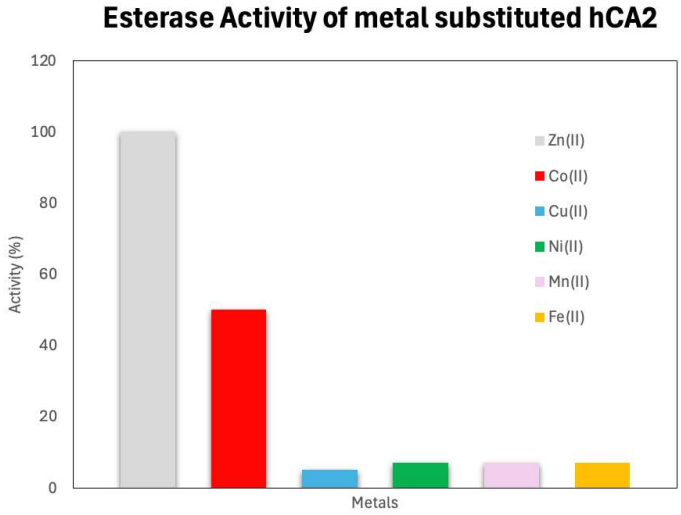

Figure 3.7: Residual esterase activity of the various metal adducts considered in this chapter.

3.3.4 Structural Characterization of hCA2 in complex with different 3*d*-transition metal ions

The structural characterization of hCA2 in complex with selected transition metal ions of the 3*d*-series, namely Mn^{2+}, Fe^{2+}, Co^{2+}, Ni^{2+}, and Cu^{2+}, was performed using both

co-crystallization and soaking approaches. As formerly described for the holo-enzyme, the same results were obtained both by co-crystallisation of the metal-adducts (Figure 3.8), and by allowing free metal diffusion into pre-formed protein crystals via the soaking technique. The use of citrate anions as the precipitant agent was successful only for the complexes with Co^{2+}, Ni^{2+}, and Cu^{2+} whereas it prevented the binding of Mn^{2+} and Fe^{2+} for which ammonium sulphate-based conditions were used for the crystallization. To improve the crystal quality, different compositions were tested, and the best diffracting crystals were obtained using precipitant solutions made of 2.6-2.7 M ammonium sulphate and 0.3 M NaCl, buffered in 50 mM TRIS-Cl at pH 8–8.5.

X-ray data collection and processing statistics for the structures of hCA2 in complex Co^{2+}, Cu^{2+}, Ni^{2+}, Mn^{2+}, and Fe^{2+} are reported in Table 3.3.

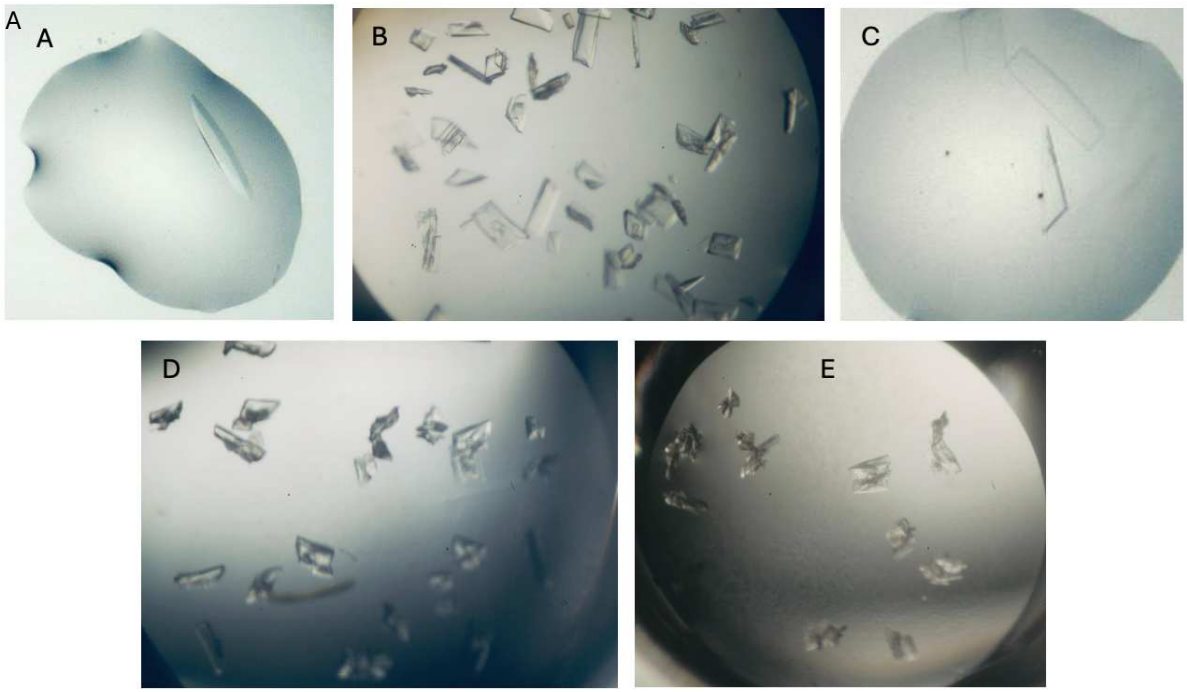

Figure 3.8: Crystal of Co-hCA2 (A), Cu-hCA2 (B), Ni-hCA2 (C) in 1.5 M sodium citrate tribasic dihydrate, 50 mM TRIS pH 7.8. Mn-hCA2 (D) Fe-hCA2 (E) in 2.7 ammonium sulphate, 50 mM TRIS pH 8.5 + 0.3M NaCl.

	Co-hCA2	Cu-hCA2	Ni-hCA2	Mn-hCA2	Fe-hCA2
Precipitant	1.4 M Na_3 citrate *2H_2O, 50 mM TRIS pH 7.8	1.4 M Na_3 citrate *2H_2O, 50 mM TRIS pH 7.8	1.4 M Na_3 citrate *2H_2O, 50 mM TRIS pH 7.8	2.7 M ammonium sulphate, 50 mM TRIS pH 8.5+ 0.3M NaCl	2.7 M ammonium sulphate, 50 mM TRIS pH 8.5+ 0.3M NaCl
DATA COLLECTION STATISTICS					
Diffraction source	I04 (DLS)	I04 (DLS)	I04 (DLS)	I04 (DLS)	I04 (DLS)
Wavelength (Å)	0.9537	0.9537	0.9668	0.9537	0.9537
Temperature (K)	100	100	100	100	100
Detector	Eiger2 XE 16M	Eiger2 XE 16M	Eiger2 XE 16M	Eiger2 XE 16M	Eiger2 XE 16M
Crystal-detector distance (mm)	168.9	168.9	168.9	189.5	189.5
Space group	$P2_1$	$P2_1$	$P2_1$	$P2_1$	$P2_1$
No. of subunits in ASU	1	1	1	1	1
a, b, c (Å)	42.03, 41.08, 71.75	42.22 40.98 71.49	42.52 41.59 72.47	42.05 41.34 72.51	42.31 41.50 72.52
β (°)	104.20	104.13	104.55	104.41	104.50
Resolution range (Å)	41.08-1.48 (1.51-1.48)	40.98-1.55 (1.58-1.55)	41.59 -1.44 (1.46 - 1.44	70.23- 1.65 (1.68-1.65)	41.51-1.53 (1.53-1.50)
Total no. of reflections	271712 (13723)	236837 (10987)	303492 (14918)	201591 (10145)	266715 (11139)
No. of unique reflections	39861 (1986)	34708 (1703)	44655 (2230)	29295 (1436)	39350 (1968)
Completeness (%)	100 (100)	100.0 (100.0)	100.0 (99.8)	100.0 (99.8)	100.0 (99.9)
Multiplicity	6.8 (6.9)	6.8 (6.5)	6.8 (6.7)	6.9 (7.1)	6.8 (5.7)
(I / σ(I))	14.3 (1.7)	9.8 (2.1)	10.3 (1.9)	8.4 (1.9)	9.6 (1.7)
CC(1/2)	1.0 (0.75)	0.99 (0.50)	0.99 (0.73)	0.99 (0.74)	0.99 (0.75)
R_{meas}	0.066 (0.99)	0.090 (0.624)	0.113 (0.972)	0.136 (0.916)	0.108 (0.867)
Overall B factor from Wilson plot (Å^2)	17.6	12.9	10.06	12.4	11.8
REFINEMENT STATISTICS					
Resolution range (Å)	40.78-1.48 (1.51-1.48)	40.98-1.55 (1.59-1.55)	40.21-1.44 (1.48-1.44)	70.23-1.65(1.79-1.65)	41.01-1.50 (1.53-1.50)
Completeness (%)	100.0(100.0)	100.0 (100.0)	99.94 (99.67)	98.89 (99.58)	99.9 (99.9)
No. of reflections, working set	37763(2768)	33063 (2434)	42442 (3104)	27821 (2044)	32270 (2769)
No. of reflections, test set	2084 (142)	1632 (135)	2194 (172)	1457 (105)	2056(140)
Final R_{cryst}	0.1744 (0.246)	0.1720 (0.226)	0.1702 (0.247)	0.1749 (0.245)	0.1743 (0.251)
Final R_{free}	0.2054 (0.269)	0.1945 (0.238)	0.1934 (0.276)	0.2263 (0.279)	0.198 (0.285)
No. of non-H atoms					
Protein	260	260	260	260	260
Ligand	-	-	-	-	-
Ion	1	4	1	1	1
Water	235	283	245	367	365
Total	496	547	506	628	626
R.m.s. deviations bonds (Å)	0.005	0.003	0.010	0.004	0.003
Angles (°)	1.089	1.181	1.733	1.206	1.135
Average B factor (Å^2)	19.2	17.1	14.1	16.1	13.6
Estimate error on coordinates based on R value (Å)	0.074	0.086	0.066	0.108	0.080

Ramachandran plot					
Most favoured (%)	97.6	97.3	96.9	96.5	96.9
Allowed (%)	2.4	2.7	3.1	3.5	3.1

Table 3.3: Data collection, processing, and refinement statistics of Co-hCA2, Cu-hCA2, Ni-hCA2, Mn-hCA2, and Fe-hCA2 structure. Values in parentheses are for the highest-resolution shell.

The structures of the metal-adducts were determined at medium-high resolution (1.44 Å – 1.65 Å), providing detailed descriptions of coordination site(s) occurring in the enzyme. As formerly reported for the apo and holo-hCA2, all crystals belong to the monoclinic space group $P2_1$, with only minor changes in unit cell parameters among the different metal-adducts. The structure of hCA2 is quite rigid and no major modifications of the protein folding are detected upon changing the metal ion bound to the enzyme (rmsd upon Cα matching ranging from 0.09 to 0.13 Å).

3.3.3.1 Co-hCA2 Structural characterization

The first adduct was characterized with Co^{2+}, showing the metal ion bound at the Zn1-site where it replaces Zn^{2+}. The Co^{2+} ion is coordinated by the three histidine residues, His94, His96, and His119, that anchor the Zn^{2+} ion in the holo-enzyme (Figure 3.9). The tetrahedral coordination geometry of Co^{2+} is completed by a water/hydroxide species, W_{Co} (Figure 3.9), mimicking the analogous ligand observed in the Zn^{2+} coordination sphere (metal-coordination distances are reported in Figure 3.9). The configuration of the active site in the Co^{2+} and Zn^{2+} complexes is remarkably similar, with analogous networks of solvent molecules. Indeed, almost overlapping positions for W_{Co}, W_{DW}, W1 and W2 are observed in the catalytic cavity of both complexes. The water molecules W1 and W2 connect Thr200 to the proton shuttling His64, which favours the "in" conformation in the Co-adduct, with the “out” orientation only minorly represented (occupancies estimated to 70% and 30%, respectively). These alternate conformations of the proton shuttling residue are crucial for an efficient proton transfer during catalysis. The meaningful conservation of the active site configuration in the Zn^{2+} and Co^{2+} adducts contributes to explain the residual activity (30-50%) of the enzyme with the latter metal ion, which was proposed to promote the catalytic reaction by a similar mechanism of action.[4] Indeed, the lower catalytic rate of Co^{2+}-substituted hCA2 was formerly exploited in mechanistic studies aimed to achieve relevant information about enzyme catalysis.[4,20,35] At first, the structure of Co-hCA2 was characterized at different pHs, 6.0, 8.5, and 11.0, reporting a pH-dependent shift in the metal coordination sphere. At the most acidic pH the cobalt ion

favours an octahedral geometry (PDB id 3KOI), shifting to a pentagonal/tetrahedral coordination at pH 8.5 (PDB id 3KOK), and to a tetrahedral coordination at pH 11.0 (PDB id 3KON)[20] (Figure 3.10). The structure characterized at intermediate pH (8.5) was explained as a mixture (50% occupancy) of the tetra- and penta-coordinated Co^{2+} species. On the other hand, we observed only a tetrahedral coordination for the Co^{2+} ion at pH 7.8, suggesting that this is the most stable configuration. The ability of Co^{2+} ion to switch to an octahedral coordination geometry contributed to explain the lower catalytic rate.[4] The structure of the Co^{2+}-adduct with bicarbonate shows the product coordinated to the metal ion as a bidentate ligand with Co^{2+} acquiring an octahedral geometry. Thus, the negative charge is distributed between the two oxygen atoms of the bidentate ion, strengthening the bicarbonate binding to Co^{2+} with respect to Zn^{2+}, which acts as a monodentate ligand. At variance with Zn-hCA2, the affinity of bicarbonate for Co^{2+} weakens at increasing pH values. This peculiar behaviour was attributed to the Co^{2+}-bound hydroxide, generated during the catalytic cycle, which creates an electrostatic repulsion with bicarbonate, promoting its dissociation from the Co^{2+}-adduct.

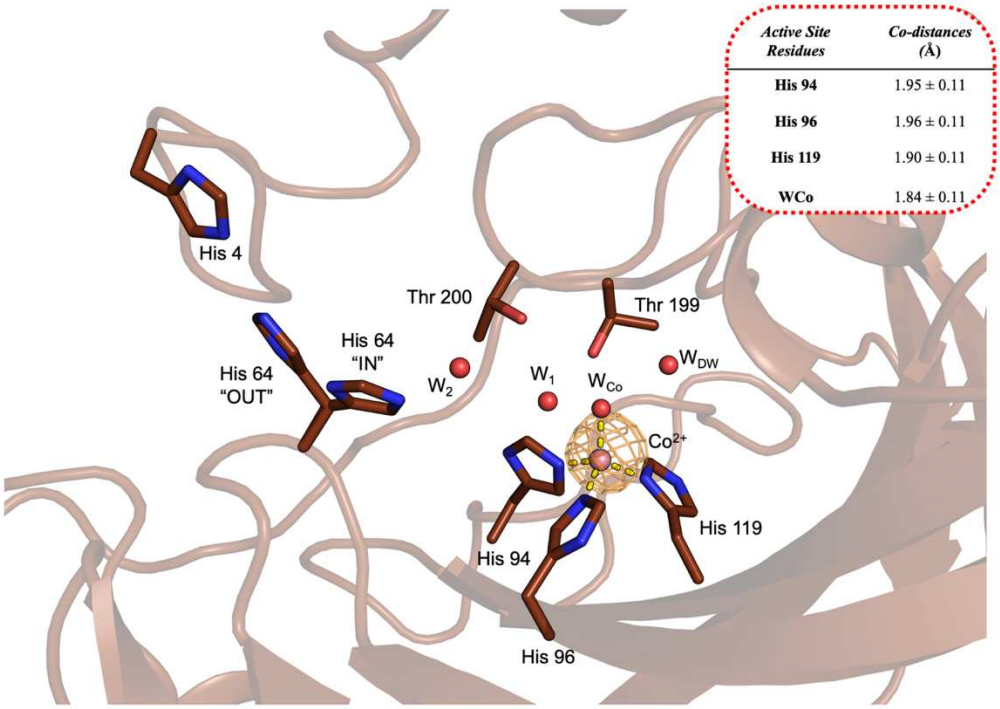

Figure 3.9: Interface view of Co-hCA2 in cartoon. The interacting residues are shown in stick representation. The key water molecules are represented as red spheres. Cobalt ion (brown sphere) is surrounded by the anomalous difference map) contoured at 5.0 σ. Coordination bonds are illustrated as yellow dashed lines. Distances between Active Site Residues and cobalt ion are shown in the panel.

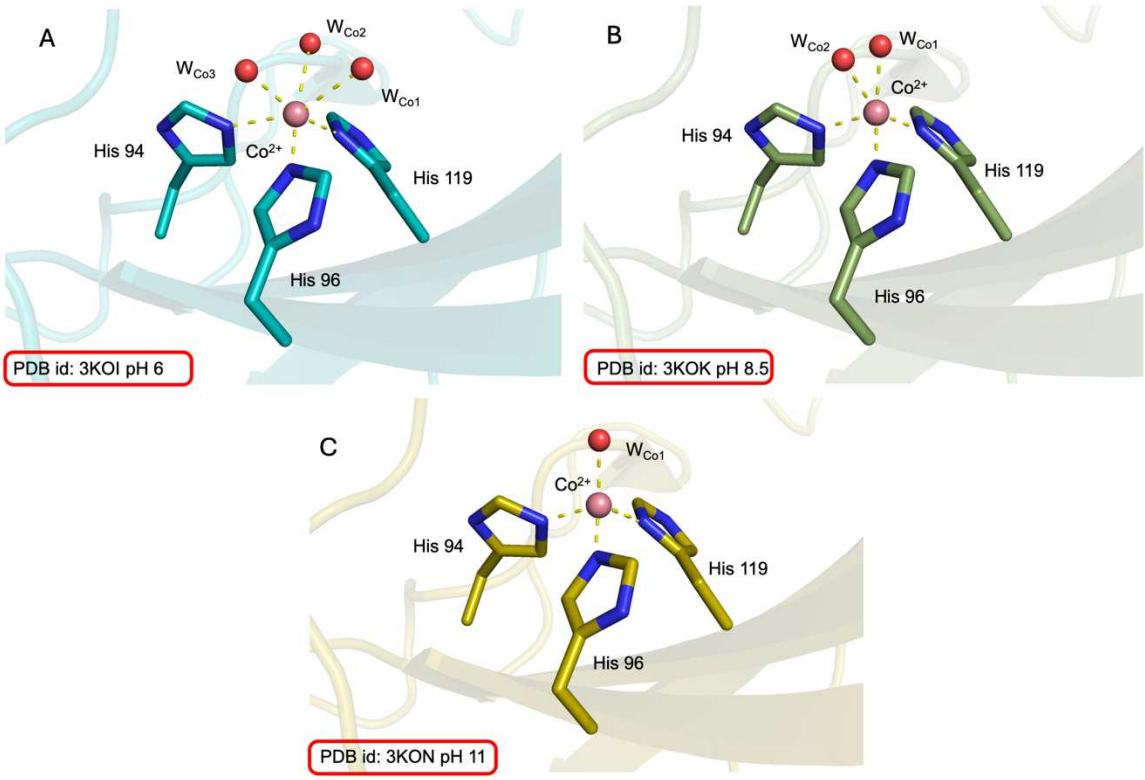

Figure 3.10: The active sites of Co-hCA2 at (A) pH 6.0 (PDB id: 3KOI), (B) pH 8.50 (PDB id: 3KOK), and (C) pH 11.0 (PDB id: 3KON). Reproduced from ref.[20]

3.3.3.2 Ni-hCA2 Structural characterization

The second metal adduct was characterized with Ni^{2+} ions, showing the metal ion anchored to the active site by His94, His96, and His119. The coordination sphere of Ni^{2+} is completed by three water molecules, named W_{Ni1}, W_{Ni2}, and W_{Ni3}, arranged in an octahedral coordination geometry. The coordination distances are summarized in a panel of figure 3.11. Although Ni^{2+} and Zn^{2+} are bound at the same site, the coordination spheres of the two metal ions are different, resulting in an almost negligible enzymatic activity of the Ni^{2+}-complex (residual activity < 10%) (Figure 3.12). The binding of Ni^{2+} is also slightly more labile; indeed, the metal ion populates this site to an estimated occupancy of 80% (instead of the full occupancy estimated for Zn^{2+}). Despite the three anchoring histidine residues are shared, the octahedral configuration of Ni^{2+} includes three water molecules $W_{Ni1\text{-}3,}$ instead of the water/hydroxide species, W_{Zn}, completing the tetrahedral coordination sphere of Zn^{2}. Furthermore, the different positions of $W_{Ni1\text{-}3}$, coordinating the Ni^{2+} ion, alter the network of solvent molecules observed in the catalytic cavity of the holo enzyme. The octahedral coordination sphere of Ni^{2+} hinders the cavity, preventing the binding of W_{DW} and $W_{1,}$ which are not observed in the Ni-adduct. The position of W_{Ni1} hinders the binding area of W_{DW}, being positioned only 1.88 Å away. A similar situation is observed also on the opposite side of the cavity, where W_{Ni3} hinders the site

of W_1 (distance of 1.64 Å). The placement of W_2 is not affected by the Ni^{2+} coordination sphere, resulting in nearly overlapping positions in the two metal complexes. W_2 mediates the interaction with the proton shuttling His64, whose side chain is observed in both "in" and "out" conformations in the Ni^{2+} complex (with the former conformation slightly more represented than the latter; estimated occupancy of 60% and 40%, respectively).

The structure of the Ni^{2+}-adduct was formerly described in the literature.[14,36] The comparison with the structure determined under similar conditions (PDB ID: 6LV5),[4] shows remarkably similar configurations of the catalytic cavity, confirming the octahedral coordination of the Ni^{2+} ion. Kim and coworkers deeply investigated the Ni^{2+}-hCA2 complex, characterizing the structure of the enzyme upon exposure to the CO_2 substrate.[4] The evidence provided by this investigation allowed to explain the drastic reduction of the catalytic rate occulting in the Ni-substituted enzyme. In the Ni^{2+} complex, the metal ion always keeps its octahedral coordination, showing altered electrostatic effects that hamper substrate conversion, product displacement, and proton transfer.

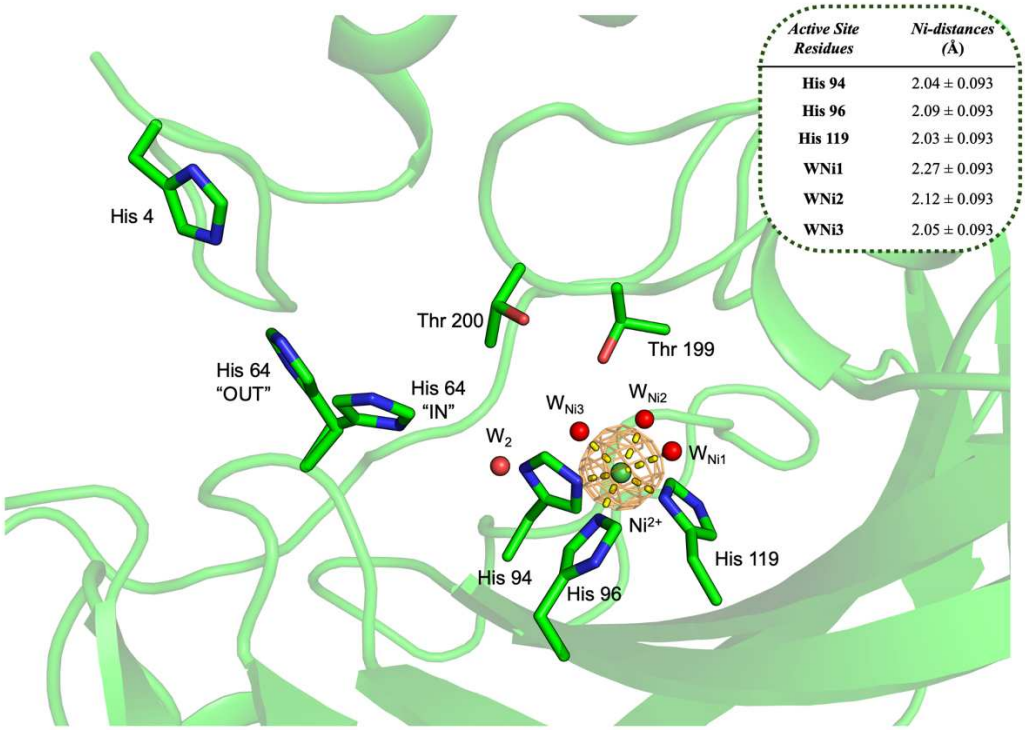

Figure 3.11: Interface view of Ni-hCA2 in cartoon. The interacting residues are shown in stick representation. The key water molecules are represented as red spheres. Nickel ion (green sphere) is surrounded by the anomalous difference map) contoured at 5.0 σ. Coordination bonds are illustrated as yellow dashed lines. Distances between Active Site Residues and nickel ion are shown in the panel.

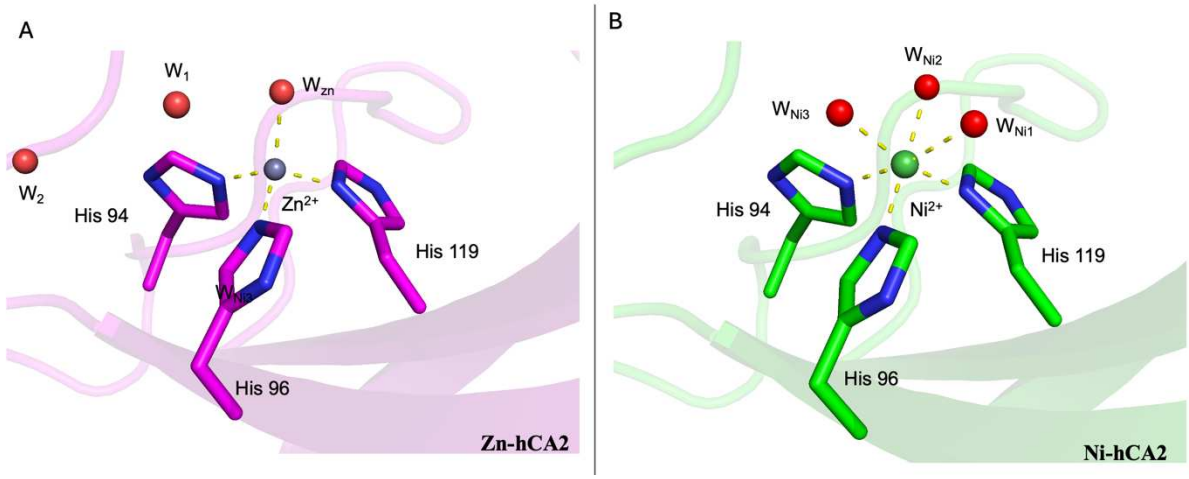

Figure 3.12: Catalytic site comparison:(A) Zn-hCA2-Interacting residues (magenta) are shown in stick representation, with key water molecules as red spheres and zinc as a grey sphere. (B) Ni-hCA2-Interacting residues (green) are in stick representation, with key water molecules as red spheres and nickel as a green sphere.

3.3.3.3 Fe-hCA2 Structural characterization

To the best of our knowledge, the structure of hCA2 in complex with Fe^{2+} has never been reported in the literature. Thus, we provide here the first structural evidence of Fe^{2+} binding to hCA2 to an almost full occupancy (estimated to be 90%). As for all other metal ions characterized so far, Fe^{2+} is anchored to the active site of the enzyme by the three histidine residues His94, His96, and His119 (Figure 3.13). At variance with zinc, Fe^{2+} favour an octahedral coordination geometry, completed in the hCA2 active site by three water molecules, named W_{Fe1}, W_{Fe2}, and W_{Fe3} (coordination distances are summarized in Figure 2.13). The proximity of Thr199 and Glu106 to the metal ion (distance of 3.80 Å and 4.06 Å, respectively), hinders its coordination sphere, inducing a distortion in the octahedral geometry and increasing the lability of W_{Fe3} whose population is estimated to be only 50 %. An analogous octahedral geometry is also observed for Ni^{2+}, where the positions of the three coordinating water molecules, W_{Ni1-3}, are almost overlapping with W_{Fe1-3}, in the Fe-adduct. An additional water molecule, modelled in two alternate positions, is located proximal to W_{Fe1} (2.21 Å). An almost continuous electron density connects these two solvent molecules suggesting the possible presence of a diatomic/triatomic species coordinated to the metal ion. As formerly described for the Ni-adduct, the octahedral coordination of Fe^{2+} prevents the accommodation of W_{DW} and W_1 in the active site. Although W_2 is conserved in the Fe-adduct, the side chain of His64 is flexible, being mostly oriented outside the cavity (estimated occupancy of 30% and 70%, for the “in” and “out” conformation, respectively).

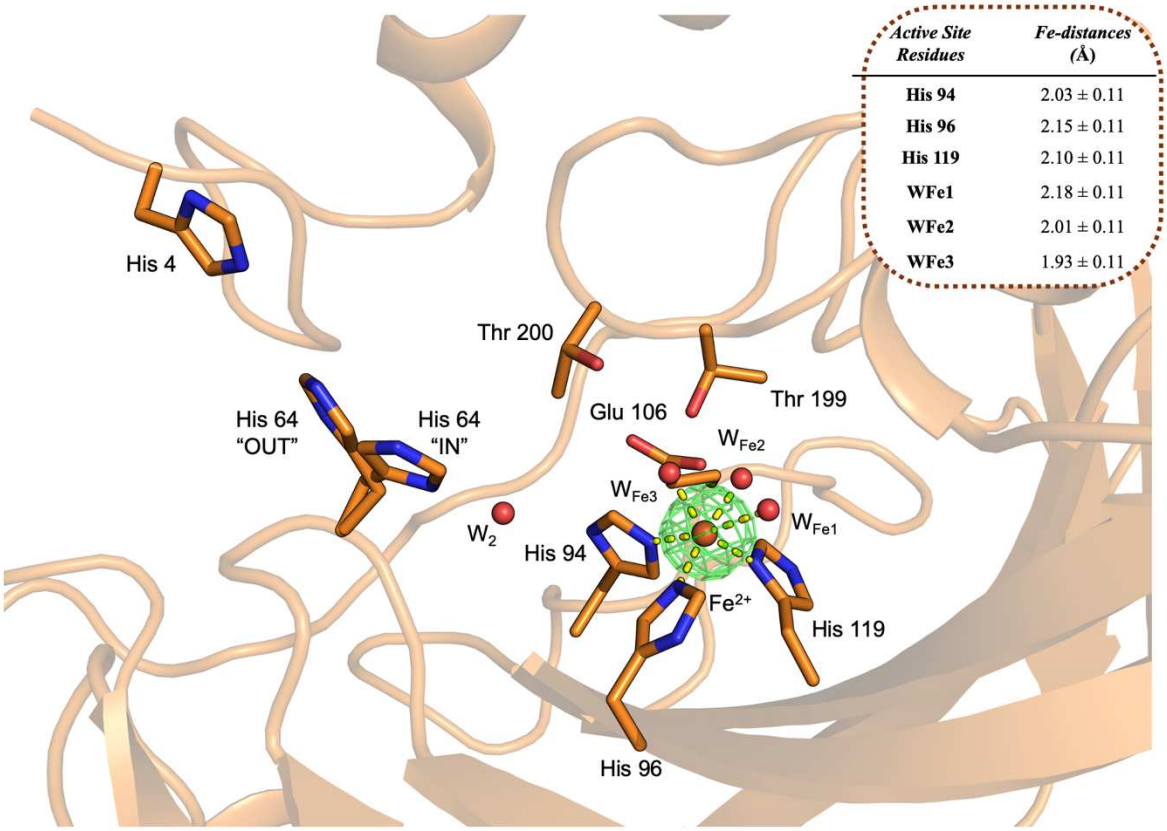

Figure 3.13: Interface view of Fe-hCA2 in cartoon. The interacting residues are shown in stick representation. The key water molecules are represented as red spheres. Iron ion (orange sphere) are surrounded by the anomalous difference map) contoured at 5.0 σ. Coordination bonds are illustrated as yellow dashed lines. Distances between Active Site Residues and Iron ion are shown in the panel.

3.3.3.4 Mn-hCA2 Structural characterization

The fourth metal adduct was characterized with Mn^{2+} ions. As described for the other metals also Mn^{2+} can replace Zn^{2+} in the catalytic cavity where is anchored by His94, His96, and His119. The coordination sphere of Mn^{2+} is completed by two water molecules, named W_{Mn1} and W_{Mn2} (coordination distances are summarized in Figure 3.14). A further water molecule is positioned very close to W_{Mn1} (2.22 Å), resulting in a continuous electron density that could suggest the presence of a diatomic species coordinating the metal ion. The population of the Mn^{2+} ion was refined to a full occupancy, suggesting a stable binding at this site. At variance with Zn^{2+}, Mn^{2+} favours a pentagonal coordination geometry at this site, slightly distorted by the presence of Thr199, located only 3.65 Å apart from the metal ion. The comparison with the structure of the holo-enzyme shows a slightly displaced position of the two metal ions, with Mn^{2+} shifted ~0.5 Å away from the Zn^{2+} ion (Figure 3.15). Furthermore, the different coordination sphere of Mn^{2+} prevents the binding of W_{DW} and W_1, observed in the holo-enzyme. The different chemical properties and binding geometries of the two metal ions reasonably explain the lack of catalytic activity detected for the Mn-adduct. On the other hand,

the coordination sphere of Mn^{2+} does not affect W_2 whose position is overlapping in the two metal complexes. W_2 is H-bonded to the proton shuttling His64 when rotated in the "in" conformation. In the Mn^{2+} complex, both "in" and "out" orientations are observed with the latter being more populated than the former (estimated occupancy to 30% and 70%, respectively).

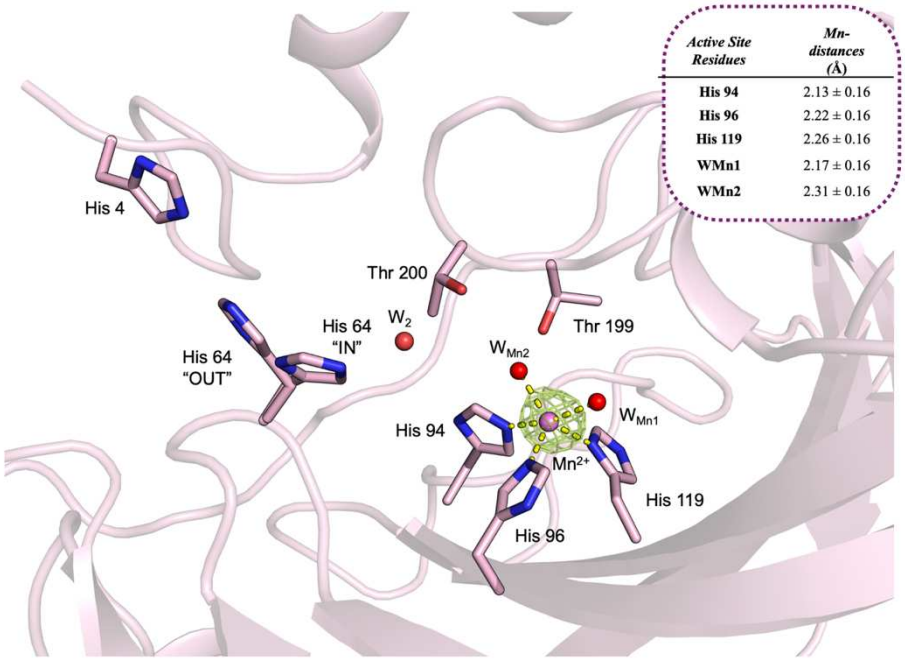

Figure 3.14: Interface view of Mn-hCA2 in cartoon. The interacting residues are shown in stick representation., The key water molecules are represented as red spheres. Manganese ion (pink sphere) is surrounded by the anomalous difference map) contoured at 5.0 σ. Coordination bonds are illustrated as yellow dashed lines. Distances between Active Site Residues and manganese ion are shown in the panel.

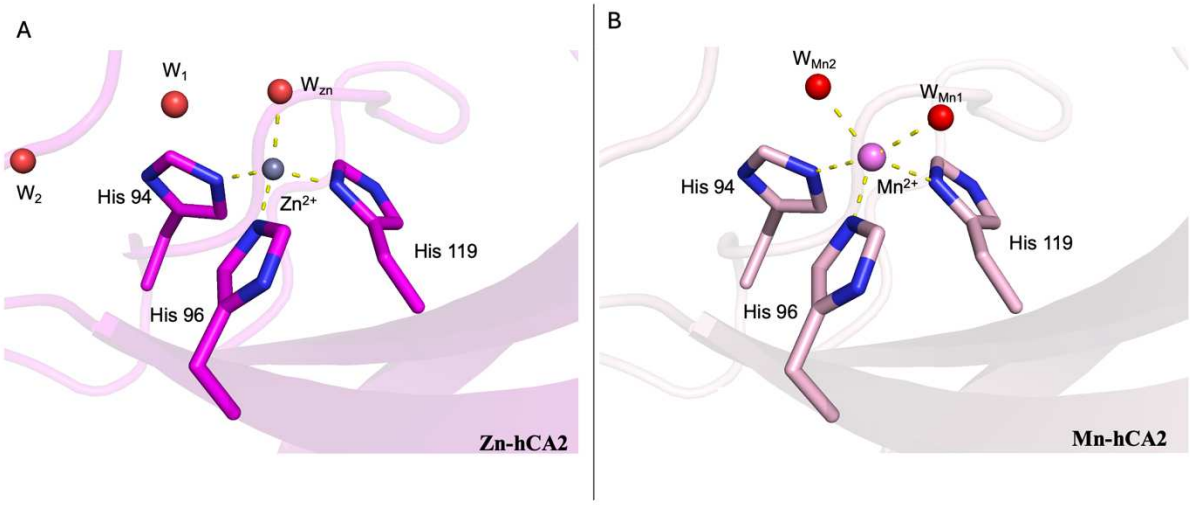

Figure 3.15: Catalytic site comparison:(A) Zn-hCA2-Interacting residues (magenta) are shown in stick representation, with key water molecules as red spheres and zinc as a grey sphere. (B) Mn-hCA2-Interacting residues (light pink) are in stick representation, with key water molecules as red spheres and manganese as a pink sphere.

The structure of the Mn-adduct was formerly described by Hakansson *et al*. (PDB ID 1RZD).[14] Although the position of the Mn^{2+} is almost overlapping in the two structures, the coordination spheres are different (Figure 3.16). At variance with our structure where the coordination of Mn^{2+} is completed by two water molecules, a sulphate anion and a water molecule are reported by Hakansson *et al*. The resulting coordination geometry of Mn^{2+} is octahedral, with the sulphate anion acting as a bidentate ligand. These meaningful differences in the metal coordination can be (at least partially) due to the different crystallization conditions as the experiments were conducted at different pH levels: pH 7.8 for the PDB structure id:1RZD and pH 8.5 for Mn-hCA2.

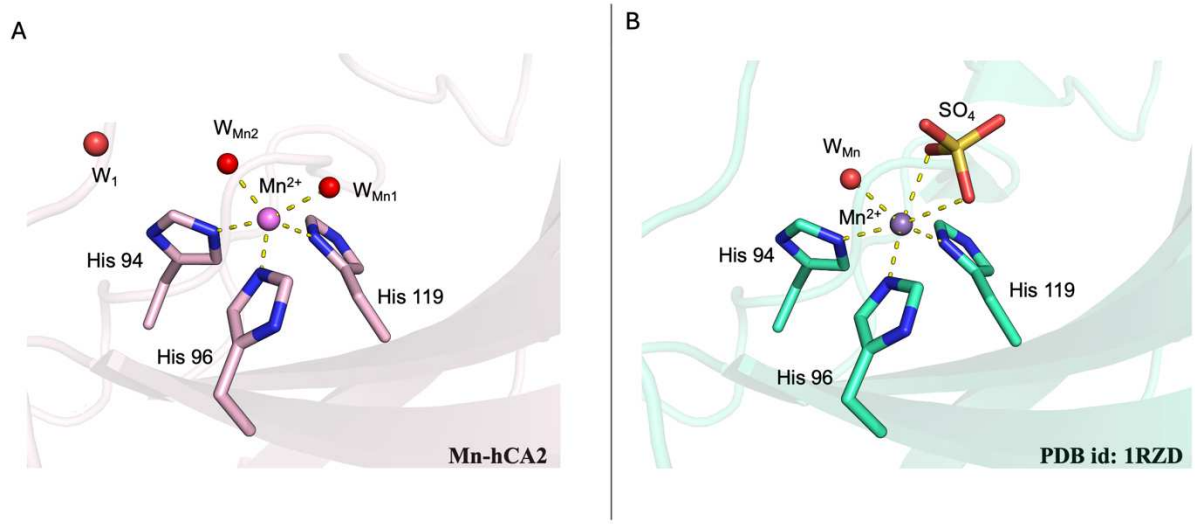

Figure 3.16: Catalytic site comparison (A) Mn-hCA2-Interacting residues (light pink) are in stick representation, with key water molecules as red spheres and manganese as a pink sphere. (B) Mn-hCA2 (PDB id: 1RZD)-Interacting residues (green, cyan)) are shown in stick representation, with key water molecules as red spheres and manganese as a violet sphere.

3.3.3.5 Cu-hCA2 Structural characterization

The fifth hCA2 – metal complex investigated in this work is the adduct with Cu^{2+} ions. As the other metals, also Cu^{2+} is anchored to the enzyme by His94, His96, and His119 (Metal-coordination distances are reported in Figure 3.17). The square pyramidal coordination geometry of the Cu^{2+} ion at this site, named Cu1, is completed by two water molecules, named W_{Cu1} and W_{Cu2}. The proximity of Glu106 and Thr199 to the metal ion (both within 4 Å) prevents the binding of a sixth ligand opposite to His94. Although the positions of the divalent metal cations are overlapping, the different coordination sphere and geometries of Cu^{2+} and Zn^{2+} modifies the solvent network inside the catalytic cavity. The comparison between the two metal adducts shows that W_{Cu1} and W_{Cu2} are displaced by ~1.5-1.7 Å with respect to W_{Zn}, hampering the catalytic properties of the Cu-adduct. The different coordination geometry

induces a slight shift (by ~0.8 Å) of the W_{DW} and W_1 positions, without affecting W_2. Former structural investigations on the Cu^{2+}-adduct confirm this configuration of the active site cavity (PDB id 6LVA),[4] but the replacement of the Cu^{2+}-coordinating water molecules by dioxygen was also reported (PDB ids 1RZC[19] and 6PDV).[12]

At variance with the other metal ions, additional Cu^{2+}-binding sites are observed in the structure of the Cu-adduct. A careful analysis of the anomalous maps calculated from the data collected above and immediately below the Cu K-edge, showed the presence of two additional Cu^{2+} ions bound to the protein, named Cu2 and Cu3. At the periphery of the active site, Cu2 is coordinated by the proton shuttling His64, which is oriented towards the cavity ("in" configuration). The slightly distorted octahedral coordination of Cu2 is completed by the backbone of His-1 (belonging to the N-terminal extension due to the TEV protease cleavage), Asn62, and a water molecule. The Cu2 site is located ~8.9 Å away from the position of Cu1. The third Cu-binding site identified in hCA2 is positioned ~11.4 Å away from Cu2, on the solvent exposed surface where Cu3 is anchored to His3 and His4. Both Cu2 and Cu3 are labile sites, having an estimated occupancy of 50%. At variance with Cu2 which was not formerly reported in the literature, the Cu3 site was described in hCA2 (PDB id 6PDV), where it was proposed to contribute to the nitrite reductase activity acquired by the Cu-adduct.[12] The coordination of Cu3 is peculiar, having a heme-like geometry that induces the rearrangement of the N-terminal tail of the enzyme.

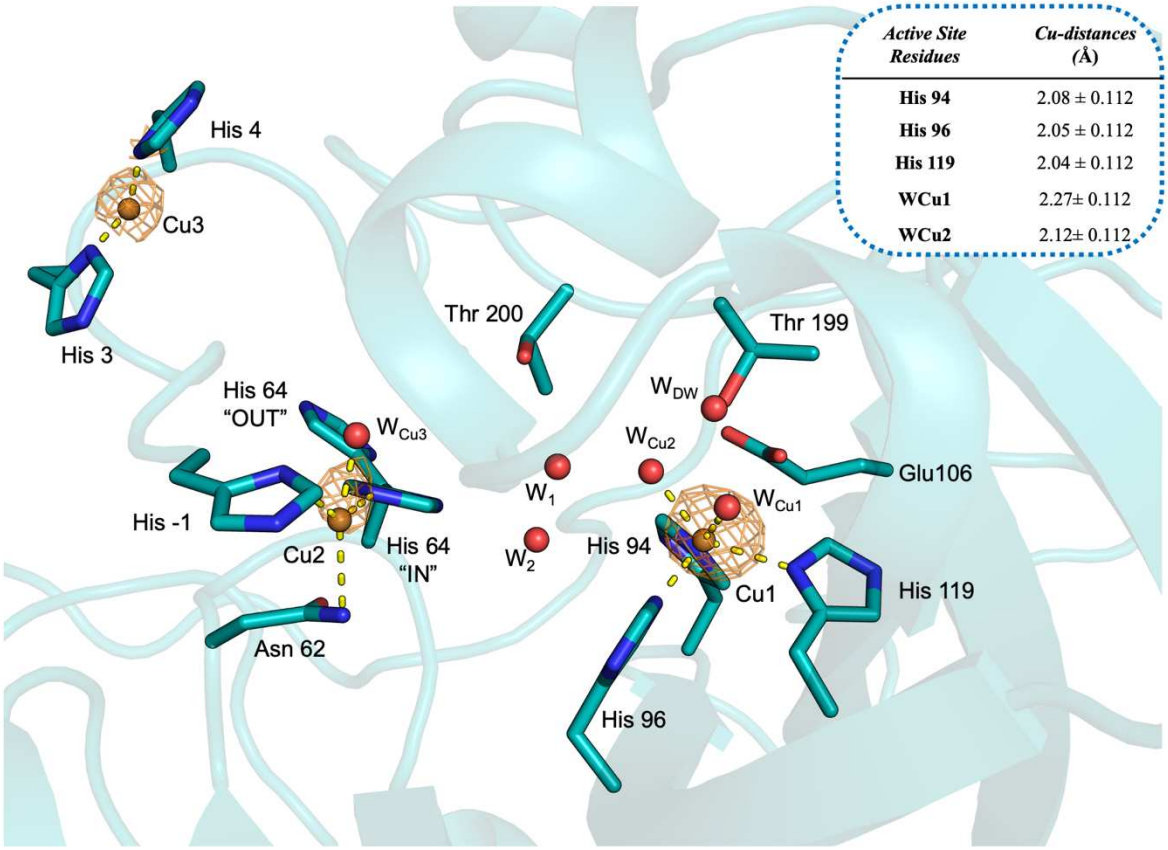

Figure 3.17: Interface view of Cu-hCA2 in cartoon. The interacting residues are shown in stick representation, The key water molecules are represented as red spheres. Copper ions (brown spheres) are surrounded by the anomalous difference map) contoured at 5.0 σ. Coordination bonds are illustrated as yellow dashed lines. Distances between Active Site Residues and copper ion are showed in the panel.

3.3.3.5.1 Structural characterization of the alanine variants in complex with Cu^{2+}

To deeper investigate the peculiar binding of Cu^{2+} to hCA2, the structure of the adducts with the alanine variants were also characterized. The structures were determined to medium-high resolution, ranging from 1.30 Å to 1.70 Å (data collection and refinement statistics are reported in Table 3.4).

	Cu-H4A	**Cu-H94A**	**Cu-H96A**	**Cu-H119A**	**Cu-H9496A**
Precipitant	1.4M Na_3 citrate *$2H_2O$, 50 mM TRIS pH 7.8	1.4M Na_3 citrate *$2H_2O$, 50 mM TRIS pH 7.8	1.4M Na_3 citrate *$2H_2O$, 50 mM TRIS pH 7.8	1.4M Na_3 citrate *$2H_2O$, 50 mM TRIS pH 7.8	1.4M Na_3 citrate *$2H_2O$, 50 mM TRIS pH 7.8
DATA COLLECTION STATISTICS					
Diffraction source	I04 (DLS)	I04 (DLS)	I04 (DLS)	P13 (PETRA III)	P13 (PETRA III)
Wavelength (Å)	0.9537	0.9537	0.9537	0.976	0.976

Temperature (K)	100	100	100	100	100
Detector	Eiger2 XE 16M	Eiger2 XE 16M	Eiger2 XE 16M	Eiger2 XE 16M	Eiger2 XE 16M
Crystal-detector distance (mm)	168.9	168.9	160.03	198.6	160.03
Space group	$P2_1$	$P2_1$	$P2_1$	$P2_1$	$P2_1$
No. of subunits in ASU	1	1	1	1	1
a, b, c (Å)	42.39, 41.72, 72.52	42.24 41.46 72.40	42.15 42.58 72.76	42.66 41.82 72.37	42.39 41.60 72.39
β (°)	104.41	104.47	104.53	104.76	104.43
Resolution range (Å)	41.72-1.30 (1.32-1.30)	70.10-1.40 (1.42-1.40)	70.43 -1.70 (1.73 - 1.70	69.98- 1.65 (1.68-1.65)	70.10-1.3o (1.32-1.30)
Total no. of reflections	375372 (19326)	327647 (16140)	177661 (9324)	203491 (9886)	370204 (18884)
No. of unique reflections	59901 (3075)	48076 (2379)	27033 (1420)	29626 (1443)	358060 (2953)
Completeness (%)	98.9 (99.5)	100.0 (100.0)	99.8 (99.8)	98.9(98.1)	96.3 (99.1)
Multiplicity	6.3 (6.3)	6.8 (6.8)	6.6 (6.6)	6.9 (6.9)	6.4 (6.4)
(I / σ(I))	10.3 (2.2)	13.7 (2.2)	7.2 (1.5)	10.4 (1.8)	11.6 (2.3)
CC(1/2)	0.99 (0.65)	0.99 (0.81)	0.99 (0.57)	0.99 (0.41)	0.99 (0.57)
R_{meas}	0.093 (0.850)	0.068 (0.661)	0.149 (0.290)	0.200 (1.260)	0.105 (0.919)
Overall B factor from Wilson plot ($Å^2$)	6.91	11.03	19.9	11.5	9.49
REFINEMENT STATISTICS					
Resolution range (Å)	40.88-1.30 (1.33-1.30)	70.10-1.40 (1.44-1.43)	70.43-1.70 (1.74-1.70)	41.29-1.65 (1.69-1.65)	40.08-1.30 (1.33-1.30)
Completeness (%)	99.1 (97.7)	100.0 (100.0)	99.62 (99.59)	98.12 (97.9)	96.2 (99.3)
No. of reflections, working set	55642 (4005)	45638 (3387)	25638 (1882)	27957 (2060)	55145 (4178)
No. of reflections, test set	2786 (218)	2422 (145)	1368 (100)	1457 (100)	2871(224)
Final R_{cryst}	0.1799 (0.255)	0.1793 (0.252)	0.1710 (0.273)	0.1841 (0.281)	0.1887 (0.287)
Final R_{free}	0.2000 (0.275)	0.2076 (0.279)	0.2080 (0.284)	0.2217 (0.295)	0.210 (0.300)
No. of non-H atoms					
Protein	260	260	260	260	260
Ligand	-	-	-	-	-
Ion	2	2	2	2	2

Water	283	343	207	259	299
Total	545	605	469	521	561
R.m.s. deviations bonds (Å)	0.003	0.003	0.004	0.004	0.003
Angles (°)	1.069	1.115	1.174	1.198	1.096
Average B factor (Å^2)	18.9	14.8	22.3	15.5	12.7
Estimate error on coordinates based on R value (Å)	0.054	0.066	0.109	0.109	0.057
Ramachandran plot					
Most favored (%)	97.3	96.9	96.5	96.1	96.1
Allowed (%)	2	3.1	3.5	3.9	3.9

Table 3.4: Data collection, processing, and refinement statistic of Cu-H4A, Cu-H94A, Cu-H96A, Cu-H119A, and Cu-H94-H96A structure. Values in parentheses are for the highest-resolution shell.

As formerly observed for Zn^{2+}, the binding of metal cations is differently modulated by the alanine-substitutions at the Zn1 site. The structures of the Cu^{2+}-adducts with the single variants H94A, H96A, and H119A show that all mutants are able to retain a residual ability of Cu-binding at this site, with estimated populations for Cu1, ranging from 40% to 90%. The mutations H94A and H119A significantly compromise Cu1 binding, resulting in only a 40% population of the active site (Figure 3.18 C and E). Since the increased lability of metal binding at this site, the coordination sphere of Cu1 is only partially defined in the mutants, being composed of two histidine residues and a water molecule. The comparison with the structure of hCA2, shows almost overlapping positions for Cu1 in the structures, with a maximal displacement of ~0.8 Å occurring in the structure of the H119A variant. On the other hand, the mutation H96A has a lower impact on Cu^{2+} binding, increasing the population of the active site to 90% (Figure 3.18 D). The position of Cu1 is shifted by only 1.1 Å from the Cu1 site observed in the wild-type enzyme. Moreover, the loss of the anchoring residue in position 96 induces a modification of the metal coordination sphere that acquires a tetrahedral geometry in the H96A variant. Further the two anchoring His94 and His119, the Cu1 coordination sphere is completed by two water molecules, named W_{Cu1A} and W_{Cu2A}. A slightly elongated electron density is observed for $W_{Cu2A,}$ which allows to hypothesize that a diatomic species (e.g., a dioxygen molecule), could be present as coordinating ligand. The population of the Cu1 site is fully

prevented only upon mutation of two anchoring histidine residues. Indeed, no metal binding is observed at this site in the H94A-H96A double variant (Figure 3.18 F).

All single variants at the Cu1 site and the double variant has a second Cu^{2+} ion bound to the enzyme at the periphery of the active site, anchored to the side chain of the proton shuttling His64 which is fully rotated "out" in the structures. The Cu^{2+} ion is further anchored to His4 belonging to the flexible N-terminal tail of the enzyme. Since the partial population of this site, ranging from 40% to 50% in the structures, the coordination sphere of Cu^{2+} is only partially defined. The comparison with the structure of hCA2 -Cu shows that the position of this second Cu^{2+} ion in the variants, named Cu2A, does not match with Cu2 and Cu3 observed in the wild-type enzyme, being located in between these sites. The different locations of Cu2 and Cu2A is due to the different orientations of the proton shuttling His64, which is directed "in" in the wild-type enzyme, whereas it points "out" in the mutants. It is worth noting that the Cu2A overlaps with the position of the Zn2 site in hCA2 described for the first time in this work.

To evaluate the contribution of His4 on Cu^{2+}-binding at the Cu2A site we characterized the structure of the Cu^{2+}-adduct with the H4A variant (Figure 3.18 B). Although the binding of Cu1 at the catalytic site is almost unaltered with respect to the wild-type enzyme, the removal of the anchoring His4 prevents the binding of Cu^{2+} at the Cu2A site. Indeed, no metal ions are observed in the Cu2A site of the H4A variant, despite the unmodified orientation of the proton shuttling His64, which retains its "out" orientation. This evidence suggests that the N-terminal tail of the enzyme has an important role in generating this additional Cu^{2+}-binding site.

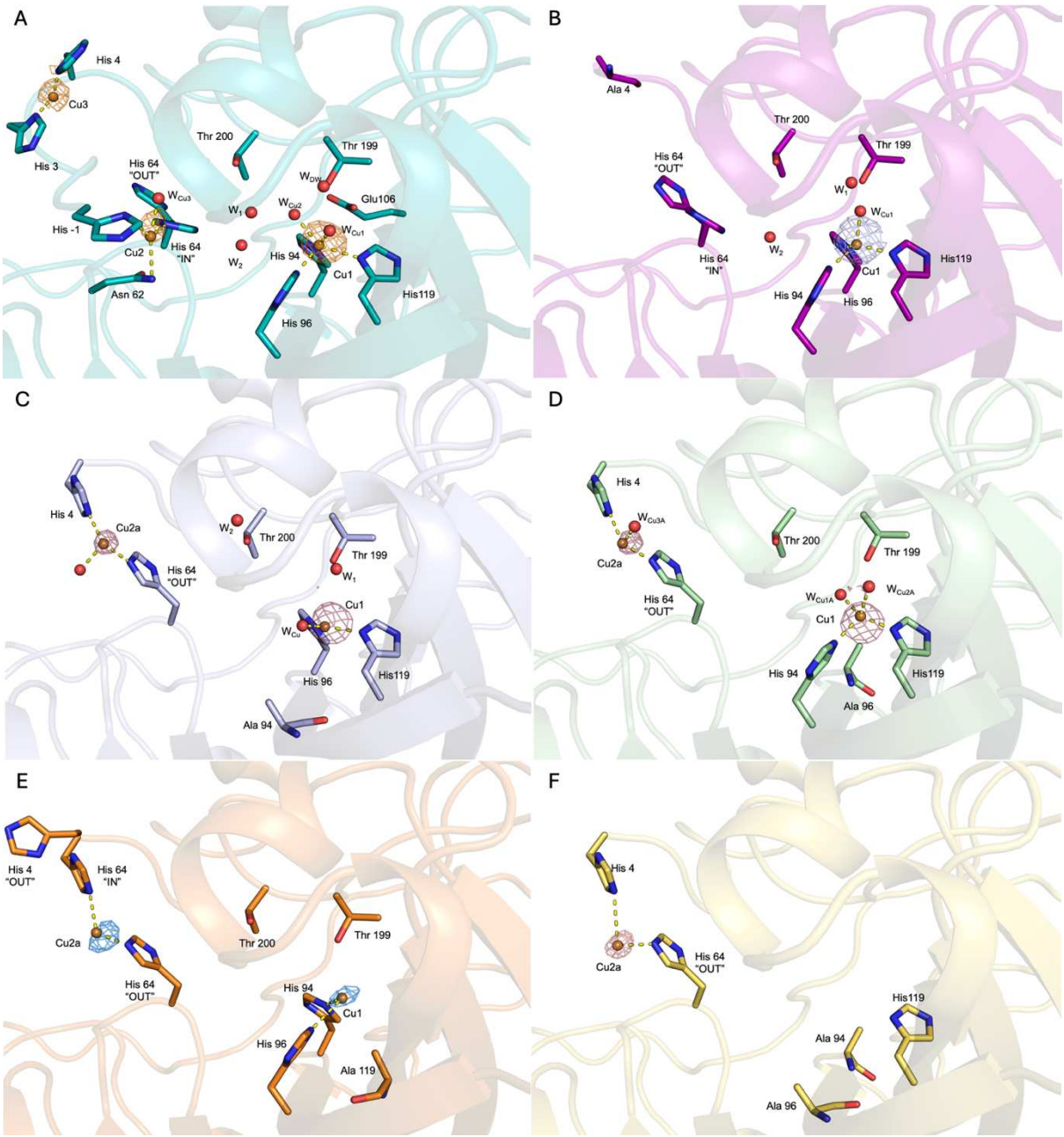

Figure 3.18: (A) Interface view of Cu-hCA2 variant in cartoon, and the interacting residues in sticks in teal. (B) Interface view of Cu- H4A variant in cartoon, and the interacting residues in sticks in violet. (C) Interface view of Cu-H94A variant in cartoon, and the interacting residues in sticks in light blue. (D) Interface view of Cu-H96A variant in cartoon, and the interacting residues in sticks in pale green. (E) Interface view of Cu-H119A variant in cartoon, and the interacting residues in sticks in orange. (F) Interface view of Cu-H94A-H96A variant in cartoon, and the interacting residues in sticks in yellow. The key water molecules are represented as red spheres. Zinc ions (brown spheres) are surrounded by the anomalous difference map) contoured at 5.0 σ. Coordination bonds are illustrated as yellow dashed lines.

Altogether these mutations unveil the critical importance of the two Cu^{2+}-binding sites in influencing the stability and coordination geometry of the metal ion, which are closely related to those observed for Zn^{2+}. The structural information obtained so far lays the groundwork for future activity studies to investigate how additional metal substitutions (*e.g.,* with metal ions

with similar electronic properties), coupled with mutations in other key residues can affect the catalytic properties of the enzyme. In particular, since Cu^{2+} derivatization determines a novel catalytic activity of the enzyme (converting it into a nitrite reductase), more modifications at the level of the metal site or the substrate-binding residues can be envisioned for enzyme reprogramming.

3.4 Conclusions

This chapter confirms the central role played by Zn^{2+} in determining the esterase function of hCA2. Its unique size and charge properties, together with the electronic configuration, determine the perfect arrangement of the catalytic site.

As expected, the substitution with other metals of the first transition series, reduces dramatically its activity, which is only retained in the Co^{2+} variant, the only capable of coordinating the three histidines and the catalytic water in a tetrahedral arrangement. Biophysical characterization, especially by ITC, has unravelled the determinant of metal binding for some of the most intriguing divalent cations in this study. In particular, it confirms the duality of sites for Cu^{2+}, each one with its own specific mode of binding. Furthermore, the clarification on the interactions between Mn^{2+} and the enzymes complements the limited information on how hCA2 can be repurposed to a peroxidase.[11]

The confirmation of the mode of binding of the enzyme to Ni^{2+} and its interpretation in energetic terms provide a starting point to investigate chemical reactions, requiring an octahedral geometry. This could also extend to other ions in the d-block that can achieve electronic configurations comparable to that of Ni^{2+}. This is the case of Fe^{2+} (d^6) which displays the tendency to octahedral coordination. Similarly to Ni^{2+}-substituted hCA2, also Fe-hCA2 retains a very low esterase activity. Fe^{2+} is a very labile species, with little affinity to the histidines in the active sites compared to other metals, but is nonetheless encountered in other families of CAs, such as the eukaryotic γ and the bacterial ones. These forms, often based on a Fe^{2+} catalytic core, in anaerobic conditions show comparable activity to their Zn^{2+} counterpart. However, as a weakly bound Fe^{2+} rapidly oxidises to Fe^{3+} in aerobic environments, studies on this ion coupled with hCA2 would be essentially speculative.

3.5 References

(1) Ragsdale, S. W. Metals and Their Scaffolds To Promote Difficult Enzymatic Reactions. *Chem. Rev.* **2006**, *106* (8), 3317–3337. https://doi.org/10.1021/cr0503153.

(2) Holm, R. H.; Kennepohl, P.; Solomon, E. I. Structural and Functional Aspects of Metal Sites in Biology. *Chem. Rev.* **1996**, *96* (7), 2239–2314. https://doi.org/10.1021/cr9500390.

(3) Parkin, G. Synthetic Analogues Relevant to the Structure and Function of Zinc Enzymes. *Chem. Rev.* **2004**, *104* (2), 699–768. https://doi.org/10.1021/cr0206263.

(4) Kim, J. K.; Lee, C.; Lim, S. W.; Adhikari, A.; Andring, J. T.; McKenna, R.; Ghim, C.-M.; Kim, C. U. Elucidating the Role of Metal Ions in Carbonic Anhydrase Catalysis. *Nat. Commun.* **2020**, *11* (1), 4557. https://doi.org/10.1038/s41467-020-18425-5.

(5) Valdez, C. E.; Smith, Q. A.; Nechay, M. R.; Alexandrova, A. N. Mysteries of Metals in Metalloenzymes. *Acc. Chem. Res.* **2014**, *47* (10), 3110–3117. https://doi.org/10.1021/ar500227u.

(6) Lionetto, M.; Caricato, R.; Giordano, M.; Schettino, T. The Complex Relationship between Metals and Carbonic Anhydrase: New Insights and Perspectives. *Int. J. Mol. Sci.* **2016**, *17* (1), 127. https://doi.org/10.3390/ijms17010127.

(7) Lisi, G. P.; Hughes, R. P.; Wilcox, D. E. Coordination Contributions to Protein Stability in Metal-Substituted Carbonic Anhydrase. *JBIC J. Biol. Inorg. Chem.* **2016**, *21* (5–6), 659–667. https://doi.org/10.1007/s00775-016-1375-6.

(8) Krishnamurthy, V. M.; Kaufman, G. K.; Urbach, A. R.; Gitlin, I.; Gudiksen, K. L.; Weibel, D. B.; Whitesides, G. M. Carbonic Anhydrase as a Model for Biophysical and Physical-Organic Studies of Proteins and Protein−Ligand Binding. *Chem. Rev.* **2008**, *108* (3), 946–1051. https://doi.org/10.1021/cr050262p.

(9) Piazzetta, P.; Marino, T.; Russo, N.; Salahub, D. R. The Role of Metal Substitution in the Promiscuity of Natural and Artificial Carbonic Anhydrases. *Coord. Chem. Rev.* **2017**, *345*, 73–85. https://doi.org/10.1016/j.ccr.2016.12.014.

(10) Krishnamurthy, V. M.; Kaufman, G. K.; Urbach, A. R.; Gitlin, I.; Gudiksen, K. L.; Weibel, D. B.; Whitesides, G. M. Carbonic Anhydrase as a Model for Biophysical and Physical-Organic Studies of Proteins and Protein−Ligand Binding. *Chem. Rev.* **2008**, *108* (3), 946–1051. https://doi.org/10.1021/cr050262p.

(11) Okrasa, K.; Kazlauskas, R. J. Manganese-Substituted Carbonic Anhydrase as a New Peroxidase. *Chem. – Eur. J.* **2006**, *12* (6), 1587–1596. https://doi.org/10.1002/chem.200501413.

(12) Andring, J. T.; Kim, C. U.; McKenna, R. Structure and Mechanism of Copper–Carbonic Anhydrase II: A Nitrite Reductase. *IUCrJ* **2020**, *7* (2), 287–293. https://doi.org/10.1107/S2052252520000986.

(13) LINDSKOG, S.; NYMAN, P. METAL-BINDING PROPERTIES OF HUMAN ERYTHROCYTE CARBONIC ANHYDRASES. *Biochim Biophys Acta* **1964**, *1* (85), 462–474. https://doi.org/doi: 10.1016/0926-6569(64)90310-4.

(14) Håkansson, K.; Wehnert, A.; Liljas, A. X-Ray Analysis of Metal-Substituted Human Carbonic Anhydrase II Derivatives. *Acta Crystallogr. D Biol. Crystallogr.* **1994**, *50* (1), 93–100. https://doi.org/10.1107/S0907444993008790.

(15) Structure and Mechanism of Copper-Carbonic Anhydrase II a Nitrite Reductase (2).Pdf.

(16) Lane, B. S.; Burgess, K. Metal-Catalyzed Epoxidations of Alkenes with Hydrogen Peroxide. *Chem. Rev.* **2003**, *103* (7), 2457–2474. https://doi.org/10.1021/cr020471z.

(17) Krishnamurthy, V. M.; Kaufman, G. K.; Urbach, A. R.; Gitlin, I.; Gudiksen, K. L.; Weibel, D. B.; Whitesides, G. M. Carbonic Anhydrase as a Model for Biophysical and Physical-Organic Studies of Proteins and Protein−Ligand Binding. *Chem. Rev.* **2008**, *108* (3), 946–1051. https://doi.org/10.1021/cr050262p.

(18) Jing, Q.; Okrasa, K.; Kazlauskas, R. J. Stereoselective Hydrogenation of Olefins Using Rhodium-Substituted Carbonic Anhydrase—A New Reductase. *Chem. – Eur. J.* **2009**, *15* (6), 1370–1376. https://doi.org/10.1002/chem.200801673.

(19) Hakansson, K. X-Ray Analysis of Metal-Substituted Human Carbonic Anhydrase II Derivatives.

(20) Avvaru, B. S.; Arenas, D. J.; Tu, C.; Tanner, D. B.; McKenna, R.; Silverman, D. N. Comparison of Solution and Crystal Properties of Co(II)–Substituted Human Carbonic Anhydrase II. *Arch. Biochem. Biophys.* **2010**, *502* (1), 53–59. https://doi.org/10.1016/j.abb.2010.07.010.

(21) Briganti, F.; Mangani, S.; Orioli, P.; Scozzafava, A.; Vernaglione, G.; Supuran, C. T. Carbonic Anhydrase Activators: X-Ray Crystallographic and Spectroscopic Investigations for the Interaction of Isozymes I and II with Histamine. *Biochemistry* **1997**, *36* (34), 10384–10392. https://doi.org/10.1021/bi970760v.

(22) Kabsch, W. *XDS*. *Acta Crystallogr. D Biol. Crystallogr.* **2010**, *66* (2), 125–132. https://doi.org/10.1107/S0907444909047337.

(23) Evans, P. Scaling and Assessment of Data Quality. *Acta Crystallogr. D Biol. Crystallogr.* **2006**, *62* (1), 72–82. https://doi.org/10.1107/S0907444905036693.

(24) Potterton, L.; Agirre, J.; Ballard, C.; Cowtan, K.; Dodson, E.; Evans, P. R.; Jenkins, H. T.; Keegan, R.; Krissinel, E.; Stevenson, K.; Lebedev, A.; McNicholas, S. J.; Nicholls, R. A.; Noble, M.; Pannu, N. S.; Roth, C.; Sheldrick, G.; Skubak, P.; Turkenburg, J.; Uski, V.; Von Delft, F.; Waterman, D.; Wilson, K.; Winn, M.; Wojdyr, M. *CCP* 4 *i* 2: The New Graphical User Interface to the *CCP* 4 Program Suite. *Acta Crystallogr. Sect. Struct. Biol.* **2018**, *74* (2), 68–84. https://doi.org/10.1107/S2059798317016035.

(25) Vagin, A.; Teplyakov, A. Molecular Replacement with *MOLREP*. *Acta Crystallogr. D Biol. Crystallogr.* **2010**, *66* (1), 22–25. https://doi.org/10.1107/S0907444909042589.

(26) Håkansson, K.; Carlsson, M.; Svensson, L. A.; Liljas, A. Structure of Native and Apo Carbonic Anhydrase II and Structure of Some of Its Anion-Ligand Complexes. *J. Mol. Biol.* **1992**, *227* (4), 1192–1204. https://doi.org/10.1016/0022-2836(92)90531-N.

(27) Murshudov, G. N.; Skubák, P.; Lebedev, A. A.; Pannu, N. S.; Steiner, R. A.; Nicholls, R. A.; Winn, M. D.; Long, F.; Vagin, A. A. *REFMAC* 5 for the Refinement of Macromolecular Crystal Structures. *Acta Crystallogr. D Biol. Crystallogr.* **2011**, *67* (4), 355–367. https://doi.org/10.1107/S0907444911001314.

(28) Emsley, P.; Lohkamp, B.; Scott, W. G.; Cowtan, K. Features and Development of *Coot*. *Acta Crystallogr. D Biol. Crystallogr.* **2010**, *66* (4), 486–501. https://doi.org/10.1107/S0907444910007493.

(29) Winn, M. D.; Ballard, C. C.; Cowtan, K. D.; Dodson, E. J.; Emsley, P.; Evans, P. R.; Keegan, R. M.; Krissinel, E. B.; Leslie, A. G. W.; McCoy, A.; McNicholas, S. J.; Murshudov, G. N.; Pannu, N. S.; Potterton, E. A.; Powell, H. R.; Read, R. J.; Vagin, A.; Wilson, K. S. Overview of the *CCP* 4 Suite and Current Developments. *Acta Crystallogr. D Biol. Crystallogr.* **2011**, *67* (4), 235–242. https://doi.org/10.1107/S0907444910045749.

(30) Williams, C. J.; Headd, J. J.; Moriarty, N. W.; Prisant, M. G.; Videau, L. L.; Deis, L. N.; Verma, V.; Keedy, D. A.; Hintze, B. J.; Chen, V. B.; Jain, S.; Lewis, S. M.; Arendall, W. B.; Snoeyink, J.; Adams, P. D.; Lovell, S. C.; Richardson, J. S.; Richardson, D. C. MolProbity: More and Better Reference Data for Improved All-atom Structure Validation. *Protein Sci.* **2018**, *27* (1), 293–315. https://doi.org/10.1002/pro.3330.

(31) Janson, G.; Zhang, C.; Prado, M. G.; Paiardini, A. PyMod 2.0: Improvements in Protein Sequence-Structure Analysis and Homology Modeling within PyMOL. *Bioinformatics* **2017**, *33* (3), 444–446. https://doi.org/10.1093/bioinformatics/btw638.

(32) Scozzafava, A.; Supuran, C. T. Hydroxyurea Is a Carbonic Anhydrase Inhibitor. *Bioorg. Med. Chem.* **2003**, *11* (10), 2241–2246. https://doi.org/10.1016/S0968-0896(03)00112-3.

(33) . Y. Pocket; Meany, J. E. The Catalytic Versatility of Erythrocyte Carbonic Anhydrase. I. Kinetic Studies of the Enzyme-Catalyzed Hydration of Acetaldehyde. *Biochemistry 4* (11), 2535–2541.

(34) Coleman, J. E. Mechanism of Action of Carbonic Anhydrase. *J. Biol. Chem.* **1967**, *242* (22), 5212–5219. https://doi.org/10.1016/S0021-9258(18)99413-5.

(35) HAkanssont, K.; Wehnertl, A. Structure of Cobalt Carbonic Anhydrase with Bicarbonate.

(36) Silva, J. M.; Giuntini, S.; Cerofolini, L.; Geraldes, C. F. G. C.; Macedo, A. L.; Ravera, E.; Fragai, M.; Luchinat, C.; Calderone, V. Non-Crystallographic Symmetry in Proteins: Jahn–Teller-like and Butterfly-like Effects? *JBIC J. Biol. Inorg. Chem.* **2019**, *24* (1), 91–101. https://doi.org/10.1007/s00775-018-1630-0.

Chapter 4

Structural and functional studies on hCA2 derivatization with Ir^{3+}

4.1 Introduction: Iridium in light-driven water splitting

Iridium is one of the rarest elements and belongs to the series of the periodic table. In its ground state Ir has the electronic configuration $4f^{14}\ 5d^{7}\ 6s^{2}$ and can be ionized to various oxidation states ranging from -1 to +6[1] (Table 4.1). In its most common oxidation state, Ir(III), the configuration d^6 allows the formation of penta-coordinated complexes, but it is more often found in low-spin octahedral arrangements.[1]

Oxidation state	Electronic configuration	Coordination number	Characteristic geometry
-I	d^{10}	4	Tetrahedral
I	d^{8}	4	Square planar
		5	Trigonal bipyramidal
II	d^{7}	4	Square planar
III	d^{6}	5	Trigonal bipyramidal
		6	Octahedral
IV	d^{5}	6	Octahedral
V	d^{4}	6	Octahedral
		5	Trigonal bipyramidal
VI	d^{3}	6	Octahedral

Table 4.1: Structural configurations of iridium in various oxidation states.[1]

Iridium-based nanomaterials have proven highly promising catalysts for water oxidation reactions.[2,3,4,5,6] Water oxidation, or splitting, is also one of the most studied biological events, as it occurs at the level of photosystem II in green plants as part of the process called photosynthesis. As a result of a chain of events, not only light is converted into chemical energy (stored in the form of ATP), but water is split in molecular oxygen (O_2) and protons (H^+). The overall multi5-step process requires the sequential extraction of four electrons and four protons

from water with a potential of 0.82 V versus the normal hydrogen electrode (NHE) at pH 7 (Figure 4.1).[7,8]

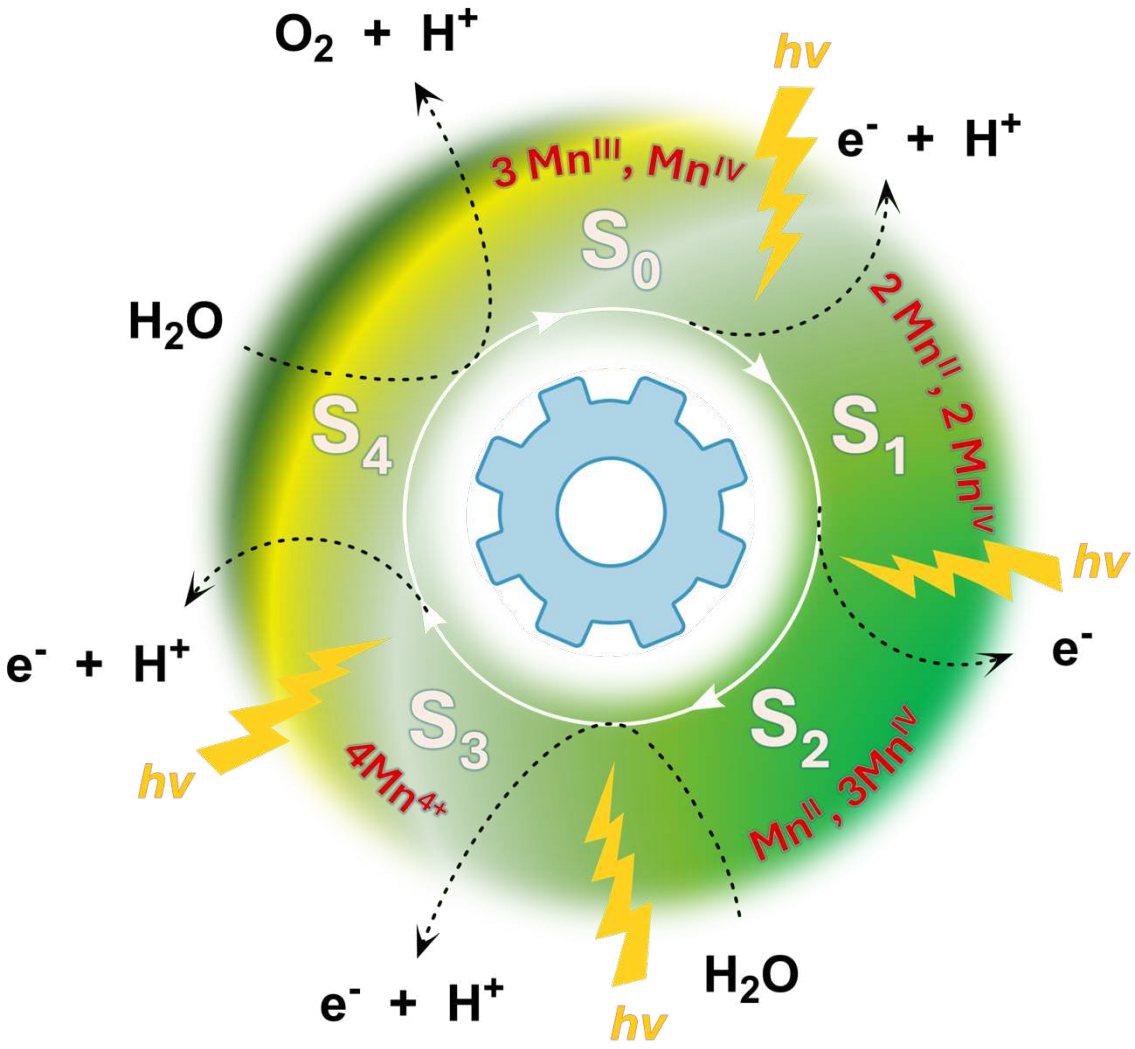

Figure 4.1: Schematic representation of the S-state cycle, where the absorption of four photons by photosystem II results in the splitting of two water molecules and the production of O2, progressing through five intermediate states (S0, S1, S2, S3, and S4). Protons (H+) are released at each stage, except during the transition from S1 to S2. Readapted from Ref. [8]

Understanding the water splitting mechanisms is crucial to enable its replication in artificial systems and energy devices. This is a key part of research on sustainable energy technologies, such as artificial photosynthesis and water-splitting catalysts. Among these catalysts, the pentamethyl-cyclopentaenyl (Cp*)Ir series, with the general formula [Cp*IrL1L2L3]X_n[9,10,11,12] showed high performance levels under various test conditions.[9,13] These versatile catalysts can be used in homogeneous or heterogeneous systems to maximize their performances in different reaction conditions (chemical, photochemical, and electrochemical processes). This showed their potential as tools in advancing sustainable catalytic technologies[14,15] and significant

attention has been directed toward modulating reactivity by carefully selecting suitable ligands for the remaining two coordination positions.[10,12,16] Kim *et al.*[17] noted how a number of Ir^{3+} coordination complexes have been variously used as water splitting catalysts.[10,11,12,18,19] In particular, the observation that imidazole-containing compounds can mimic the active site of histidine-coordinated metals in proteins like CAs, the substitution of the naturally occurring Zn^{2+} could be used to repurpose the enzyme.[19,20] The authors demonstrated how the Ir^{3+}-substituted bovine CA can elicit some degree of water splitting activity.[17]

Developing from this purely biochemical work, we wanted to extend the description of the phenomenon from a structural point of view, and to complement it with biophysical investigation. To do this, we produced the Ir^{3+}-hCA2 complex from the apo-enzyme and analysed the metal coordination properties by means of X-ray crystallography. As for other metals, we also studied Ir^{3+} binding by means of isothermal titration calorimetry and investigated the water-splitting activity of the human isoform of the enzyme which is object of this thesis.

4.2 Materials and methods

4.2.1 Protein expression, purification and crystallization

Apo-hCA2 and the five alanine variants were obtained as described in Chapter 2 (sections 2.2.1-2.2.). The purified proteins were dialyzed overnight in 50 mM BES at pH 6.95. The enzyme and the alanine variants were crystallized using the sitting drop vapor-diffusion method at 8 °C. Drops were prepared by mixing equal volumes (2µl) of protein (3-10 mg/ml) and precipitant (2.7-2.8 ammonium sulphate in either 50 mM TRIS pH 8.5, or 50 mM BIS-TRIS pH 6.5, or 50-mM BES pH 6.95) solutions equilibrated over a 200-µL reservoir. Crystal of apo-hCA2 and its alanine variants were soaked with $IrCl_3$ (1.25 mM), allowing free Ir^{3+} diffusion for 4-16 hours.

The co-crystallized approach was also attempted by loading the apo-proteins with a molar excess (5-15 equivalents) of $IrCl_3$ and incubating the sample overnight at 4 °C prior to the crystallization setup. Before flash-freezing in liquid nitrogen, all crystals (resulting either from the co-crystallization or the soaking approach) were washed in the cryoprotectant solutions (consisting of precipitant solutions supplemented with 20% glycerol).

4.2.2 X-ray data collection, structure solution, and refinement

X-ray diffraction data were collected at 100 K, using synchrotron radiation at the DLS beamline I04 equipped with an Eiger 2XE 16M detector, the ESRF beamline ID30B, on an Eiger2 9M detector, and the Petra III beamline P13 on an Eiger 16M detector. Data were integrated with XDS[21] and scaled using AIMLESS from the CCP4i2 suite.[22] Data collection and reduction statistics are shown in Table 4.5. The crystals of hCA2 and its variants belong to the monoclinic space group $P2_1$. The structures were solved by molecular replacement with Molrep,[23] using the structure of hCA2 (PDB code 2CBA)[24] as the search model (metal ions and water molecules were preventively removed). The structures were refined using REFMAC[25] from the CCP4i2 suite. The molecular graphics software Coot[26] was used for visual inspection and manual modelling of the structures and to add water molecules. The binding of iridium was evaluated by performing data collection at multiple energies (13.5 keV, 12.7 keV and 11.1 keV); anomalous difference Fourier maps were then calculated using the program FFT from the CCP4 suite.[27] Anomalous signals ranging between 6 and 10 σ were detected in the structures. The occupancies of metal ions were adjusted to keep their atomic displacement parameters close to those of nearby protein atoms in fully occupied sites.

Final structural models were validated and checked with the software Molprobity;[28] refinement statistics are reported in Table 4.5. Figures were prepared using the molecular graphics software PyMol.[29]

4.2.3 Isothermal titration calorimetry (ITC) and Surface Plasmon Resonance (SPR) analysis

ITC experiments were performed in a MicroCal VP-ITC calorimeter at 25 °C. The concentration of apo-hCA2 was determined spectrophotometrically at 280 nm (ε_{280} = 52,300 M^{-1} cm^{-1}). The experiment involved titrating apo-hCA2 (300 µl, 250 µM) with $IrCl_3$ (70 µl, 6.84 mM). All samples were prepared in 25 mM BES, pH 6.95 The titration was performed in 17 injections of 2.4 µl in 4.8 s followed by 150 s re-equilibration time after each step. Control runs were performed for each assay by titrating metal in the buffer (25 mM MOPS pH 7.4) and used for background subtraction. ITC data were analysed using the MicroCal Origin software and used to obtain best-fit values for stoichiometry (*n*), enthalpy (*ΔH*), and dissociation constant (K_d). Each experiment was performed in duplicate, and the best results are reported here. SPR experiments were performed at 25 °C using the Biacore T200 (version 3.2.1) system and 50 mM BES pH 6.95 as running buffer. The immobilization process was carried out on 100 µl protein samples (50 µg/ml in 0.01M acetate pH 5.5) to a constant flow rate of 30 µl/min. The sensor CHIP CM5 was activated for 7 minutes by injecting a mixture of 0.1 M EDC, 0.1 M NHS, and 1 M ethanolamine.

$IrCl_3$ solutions (200 µl) at five different concentrations (500 µM, 250 µM, 100 µM, 50 µM, 10 µM) were prepared in 50 mM BES, pH 6.95. Analyses were performed in duplicate, proceeding from the lowest to the highest iridium concentration. Data sets were processed and analysed using the Biacore T200 evaluation software.

4.2.4. Water oxidation catalytic activity

The water oxidation catalytic activity of Ir-loaded hCA2 and its alanine variants was evaluated using $NaIO_4$ as a sacrificial oxidant[30]. Apo-hCA2 (3mg/ml, in 50 mM BES, pH 6.95) was incubated with 1.5 mM $IrCl_3$ overnight at 4 °C. Then, the Ir-loaded enzyme was added to the reaction buffer, 25 mM sodium phosphate pH 7, supplemented with 5 mM $NaIO_4$, to a final concentration of 0.12 mg/ml. In the reaction, oxygen evolution is coupled with the reduction of $NaIO_4$,[13] allowing the spectrophotometric monitoring of the sacrificial oxidant degradation

at 280-310 nm. Control experiments were performed on apo-hCA2, Zn-loaded hCA2, and $IrCl_3$ as possible water-oxidizing catalysts. Each experiment was performed in triplicate.

4.3 Results and Discussion

4.3.1 Carbonic Anhydrase Sequence Alignment

Kim and co-workers focused their studies on the CA extracted from bovine erythrocytes.[17] As this material is commercially available, but there is no detailed information about the exact isoform, it is plausible that the behaviour described in the paper should be attributed to a mixture of bovine Cas in relation to their abundance in the hematic tissue. For this reason, we analysed and compared our recombinant protein sequence (Uniprot entry P00918) with those from *Bos taurus* (bCA2*)* in the same database. The sequences were aligned using Protein blast and are presented in figure 4.2. The sequence alignment between hCA2 and bCA2 revealed a high degree of conservation, with 81% sequence identity and 87% sequence similarity over 256 aligned residues; the residues comprising the catalytic site are fully conserved in both sequences. Although the various isoforms present a high overall similarity, there can still be differences in their binding mode to the various metals, as well as more complex and long-range modulations on the water network. For this reason, our structural results might not match completely the behaviour of the bovine system.

The sequence alignment revealed specific amino acid substitutions, highlighted in red, distributed along the protein sequence, which may influence the local conformation of the protein. Some of these differences are in regions potentially involved in catalytic activity and structural stability. For instance, the L → V substitution could affect the flexibility of the side chain, as valine is smaller and less flexible than leucine, potentially influencing local structural dynamics. Similarly, the D → S substitution may alter hydrogen bond formation, given that aspartic acid is negatively charged at physiological pH, whereas serine is a neutral polar residue. This modification could impact electrostatic interactions and hydrogen bonding patterns, ultimately affecting the stability and functionality of the protein.

Nonetheless, the high level of similarity within the active site in terms of crucial residues for the reference structure in relationship with the bovine CA2 (PDB id: 1V9E)[31] and the one considered in this study, suggests an overall preservation of essential features for the development of the catalytic activity.

Proteins	Sequences	
h-CA2	SHHWGYGKHNGPEHWHKDFPIAKGERQSPVDIDTHTAKYDPSLKPLSVSYDQATSLRILN	60
b-CA2	SHHWGYGKHNGPEHWHKDFPIANGERQSPVDIDTKAVVQDPALKPLALVYGEATSRRMVN	60
h-CA2	NGHAFNVEFDDSQDKAVLKGGPLDGTYRLIQFHFHWGSLDGQGSEHTVDKKKYAAELHLV	120
b-CA2	NGHSFNVEYDDSQDKAVLKDGPLTGTYRLVQFHFHWGSSDDQGSEHTVDRKKYAAELHLV	120
h-CA2	HWNTKYGDFGKAVQQPDGLAVLGIFLKVGSAKPGLQKVVDVLDSIKTKGKSADFTNFDPR	180
b-CA2	HWNTKYGDFGTAAQQPDGLAVVGVFLKVGDANPALQKVLDALDSIKTKGKSTDFPNFDPG	180
h-CA2	GLLPESLDYWTYPGSLTTPPLLECVTWIVLKEPISVSSEQVLKFRKLNFNGEGEPEELMV	240
b-CA2	SLLPNVLDYWTYPGSLTTPPLLESVTWIVLKEPISVSSQQMLKFRTLNFNAEGEPELLML	240
h-CA2	DNWRPAQPLKNRQIKA	256
b-CA2	ANWRPAQPLKNRQVRG	256

Figure 4.2: Sequence alignment among the human-CA2 (PDB ID: 2CBA)[32] and the bovine-CA2 sequence (PDB ID: 1V9E).[31] Unconserved residues are highlighted in red, while catalytic site residues are marked with asterisks.

4.3.2 hCA2 Characterization: thermal stability and binding assays

The ITC titration curve for Ir^{3+} binding to apo-hCA2 (Figure 4.3) indicates a mildly exothermal reaction with a stoichiometry of ~1, as expected for the single metal-binding site within the catalytic cavity. Upon fitting the data with a single-site model, the relatively low enthalpic contribution (ΔH = -1.13 kcal/mol) summed with a light entropic gain ($-T\Delta S$ = -1.83 kcal/mol), and lead to a modest binding free-energy (ΔG = -2.96 kcal/mol) compared to other metals. The overall binding constant (K_d = 6.79 × 10^{-3} M) is two orders of magnitude higher than that reported for the bovine CA (K_a = 1.23 × 10^4 M^{-1}, K_d = 8.13 × 10^{-5} M)[17] (Table 4.3). It would be difficult to describe the exact reasons for these differences, as we lack the structure of Ir^{3+}-bound form of the bovine isozyme, or mixture thereof. Is it possible to hypothesize that, although the Zn^{2+}-bound for hCA2 and bCA2 are very conserved in the active site, additional features in the unconserved parts of the proteins might mediate the adaptation of the protein structure to the binding of this bulky non-natural metal ion.

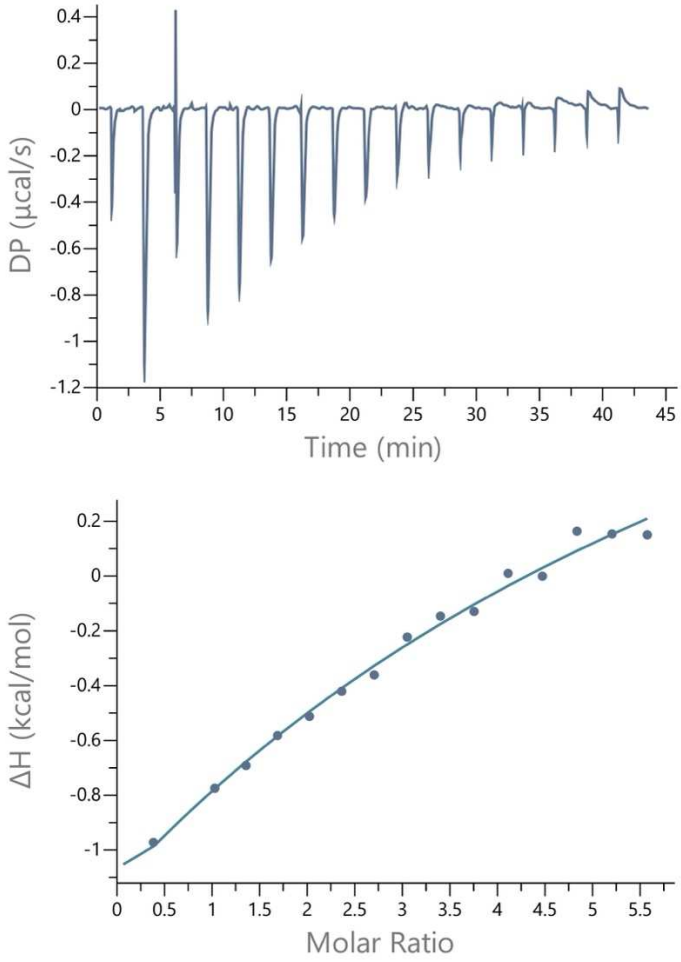

Figure 4.3: (A) ITC data involved titrating 250 µM, apo-hCA2 (300 µl) with 17 injections × 8.84 µl of 10 mM of $IrCl_3 \bullet XH_2O$ (70µl) in 50 mM BES at pH 6.95. (B) Integrated isotherm and best associated fit for a one-site binding model. The third injection was excluded from the one-site binding model as it could not be reliably fitted into the model.

	[Syr] (M)	**[Cell] (M)**	***n* (sites)**	***K*$_d$ (M)**	**Δ*H*** **(kcal/mol)**	**Δ*G*** **(kcal/mol)**	**-*T*Δ*S*** **(kcal/mol)**
Ir-hCA2	$6.84e^{-3}$	$2.5e^{-4}$	1.18	$6.79e^{-3}$	-1.13	-2.96	-1.83
Ir-bCA2	$1.5\ e^{-3}$	$1.0e^{-4}$	1.0	$8.13e^{-5}$	-10.8	-5.56	-5.2

Table 4.3: Biophysical values obtained upon titration of apo-hCA2 with Ir^{3+} using the one site binding model. The data were compared with those reported in the study by Kim et al[17].

To further investigate this incongruency between the human and the bovine isoform of the enzyme, we performed surface plasmon resonance (SPR) experiments. The analysis of the sensorgram for the binding of Ir^{3+} was analysed and is reported below (Figure 4.4). Fitting the experimental data with a monomodal curve results in an intermediate binding constant (K_d = 6.01 × 10^{-4} M) between our ITC data and those of the group working with the bovine CA. Far from providing a definitive value for the binding constant, it nonetheless confirms the

weak nature of binding. The discrepancies between ITC and SPR can be partly explained by the different nature of the two measurements (in solution vs immobilized protein) and of the binding dynamics in the two experiments. Moreover, the failure to reach a saturation plateau in both experiments could suggest the possible occurrence of non-specific interactions, potentially involving multiple Ir^{3+} ions per protein molecule.

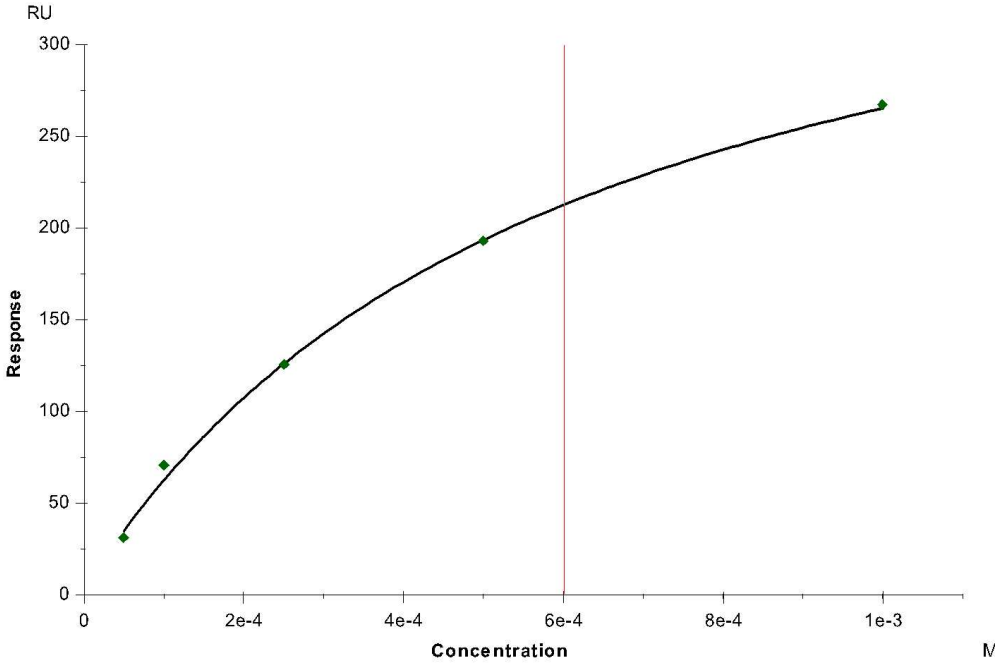

Figure 4.4: Fitting curve of a single-cycle kinetic in SPR analysis.

4.3.3 Ir hCA2 esterase and water oxidation activity

Like for the other metals described in the previous chapter, we screened also the Ir^{3+}-substituted form of hCA2 for esterase activity. As expected, the replacement of Zn^{2+} with a cation which is not only much bulkier but also in a different electronic configuration, led to almost complete loss of activity (10%), compared to esterase activity of Zn^{2+} (100%). This is corroborated by our structural data (discussed below), which confirm the change of geometry from the tetrahedral to the expected trigonal bipyramidal one.

The novel, water-splitting catalytic activity, was also verified with a sodium periodate ($NaIO_4$) based colorimetric assay. $NaIO_4$, an oxidant working at neutral pH, could be used in nearly-physiological conditions[13]. In the assay, IO_4^- ions interact with the metallic centre of the catalyst leading to form an active metal-oxo species that oxidises the substrate water molecule. As IO_4^- is subject to natural degradation, formation of IO_4^--hydroxyl species which can contribute to

the overall reaction[33,30] requires accurate working procedures and controls. The UV absorption of IO_4^- (ε_{290} = 45.5 $M^{-1}cm^{-1}$ and ε_{310} = 14.7 $M^{-1}cm^{-1}$, calculated by Lambert-Beer law) and provides an indirect measurement of the evolution of oxygen.

Our data confirm also for the human CA2 the capacity of oxidising water when the metallic centre is substituted with an Ir^{3+} ion. The degradation reaction of sodium periodate ($NaIO_4$) catalysed by carbonic anhydrase was monitored spectrophotometrically at 290nm 310nm. The measured absorbance rate was 0.0063 AU/s 0.0021 AU/s, with a reaction time of 35 seconds and an initial concentration of 5 mM. The total change in absorbance was calculated as:

$$\Delta A = rate\ (AU/s) \cdot time\ (s) = 0.0063 \cdot 35 = 0.0735AU$$

Using the Lambert-Beer law (1), it was possible to determine the change in concentration of the periodate:

$$A = \varepsilon \cdot c \cdot b \qquad (1)$$

Where:

- ε = 45.5 $M^{-1}cm^{-1}$ is the molar extinction coefficient of $NaIO_4$ at 290 nm,
- b=1 cm is the optical path length of the cuvette.

$$\Delta c = \frac{\Delta A}{\varepsilon \cdot b} = \frac{0.0735}{14.7 \cdot 1} = 5 \cdot 10^{-3} M = 5\ mM$$

The percentage of $NaIO_4$ consumption relative to the initial concentration is:

$$\%\ NaIO_4\ consumption = \frac{\Delta c}{c_0} \cdot 100 = \frac{5}{5} \cdot 100 = 100\%$$

These data indicated that periodate was completely consumed within 35 seconds, demonstrating rapid turnover and efficient catalysis of the water oxidation reaction by carbonic anhydrase. In contrast, the reaction rates were negligible in the presence of natural Zn2+ or the other transition metal ions (Co^{2+}, Cu^{2+}, Ni^{2+}, Mn^{2+}, and Fe^{2+}) presented in Chapter 3. Similarly, the negative control with a 10 mM $IrCl_3$ (without hCA2) exhibited only weak activity, with slopes of 0.0019 AU/s at 290 nm and 0.0008 AU/s at 310 nm and the activity at 30%, likely due to the formation of IrO_x species in solution (Figure 4.5).

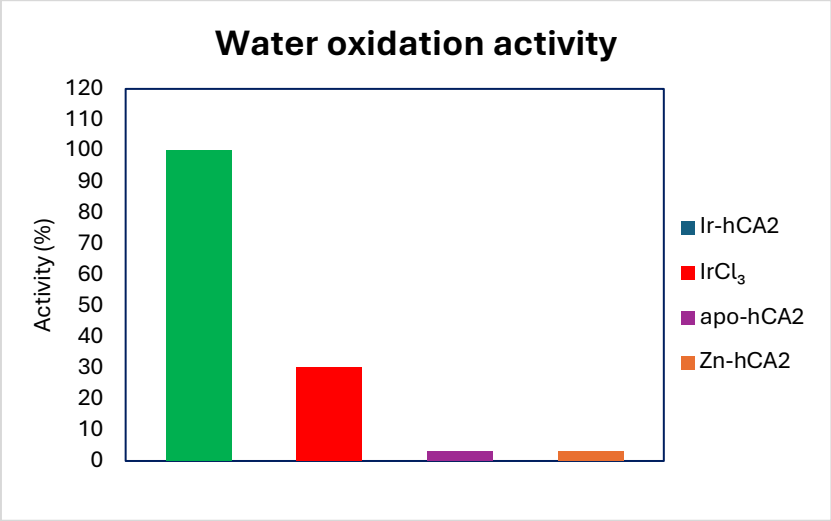

Figure 4.5: Histogram of water oxidation activity: Ir-hCA2 is represented in green, $IrCl_3$ in red, apo-hCA2 in purple, and Zn-hCA2 in orange.

4.3.4 Ir-hCA2 Structural Characterization

Different attempts to characterize the structure of Ir-substituted hCA2 were done using both the co-crystallization and soaking approaches. Crystallization trials were performed using ammonium sulphate-based precipitants, buffered in either 50 mM TRIS, pH 8.5-, or 50 mM BES, pH 6.95, or 50 mM BIS-TRIS, pH 6.5. Ir-loading was attempted by both soaking preformed apo-protein crystals grown under these conditions for 4 -16 hours, and by co-crystallizing the enzyme upon 4 -16 h incubation with a molar excess of Ir^{3+}. A comprehensive summary of the crystallization trials and the related results is provided in Table 4.4 (results are color-coded as red for 'lack of iridium binding in the structure', and green for 'structural evidence of Ir-substituted enzyme'). All crystals obtained relying on precipitant solutions buffered in 50 mM BES, pH 6.95 resulted in poor diffraction patters, preventing the characterization of the enzyme-metal complexes.

The characterization of the Ir-substituted hCA2 was particularly challenging. Indeed, the structure of the enzyme-metal complex was obtained only by co-crystallizing the Ir-substituted hCA2, resulting upon exposure to an excess of Ir^{3+} ions for 16 h. Even under these optimized conditions, the maximum population achieved for Ir^{3+} within the hCA2 catalytic site was ~30%. Control experiments were carried out on the apo and holo-enzyme in buffer BES (50 mM, pH 6.95) that were crystallized under the same conditions used to obtain the Ir-substituted hCA2.

Protein	Precipitant	Iridium in the catalytic site
Ir-hCA2 - Soaking 4 hours	2.7 M Ammonium Sulphate + 50 mM TRIS pH 8.5	No iridium
Ir-hCA2- Soaking 4 hours	2.7 M Ammonium Sulphate + 50 mM BIS-TRIS pH 6.5	No iridium
Ir-hCA2- Soaking overnight	2.7 M Ammonium Sulphate + 50 mM BIS-TRIS pH 6.5	No iridium
Ir-hCA2– Cocrystallization 4 hours	2.7 M Ammonium Sulphate + 50 mM BIS-TRIS pH 6.5	No iridium
Ir-hCA2 - Cocrystallization over night	2.7 M Ammonium Sulphate + 50 mM BIS-TRIS pH 6.5	Occupancy 30%
Apo-hCAII in BES	2.7 M Ammonium Sulphate + 50 mM BIS-TRIS pH 6.5	APO
Zn-hCA2 - Cocrystallization 4 hours	2.7 M Ammonium Sulphate + 50 mM BIS-TRIS pH 6.5	Zn

Table 4.4: The classification of Ir-hCA2 structures is represented using a color-coding system: red indicates structures where iridium is absent, green represents structures where iridium is present (with the corresponding occupancy values indicated), yellow corresponds to the protein in its apo form, and blue denotes the protein bound to Zn.

The structure of Ir-substituted hCA2 was determined at 1.60 Å resolution (Table 4.5), showing Ir^{3+} ions bound within the enzyme catalytic cavity at the three histidine residues His94, His96, and His119. Two additional water molecules, named W_{Ir1} and W_{Ir2}, complete the coordination sphere of the metal ion, resulting in a distorted trigonal bipyramidal geometry (ligand coordination distances are summarized in Figure 4.5). As formerly observed also for other metal ions acquiring a pentagonal coordination at this site, the distortion of the ligand sphere is induced by the proximity of Glu106 and Thr199. Indeed, they are both positioned within only ~3.9 Å form the metal ion, disfavouring the binding of a sixth ligand and inducing a distortion of the trigonal bipyramidal coordination geometry (Figure 4.6). The occupancy of Ir^{3+} within the hCA2 active site was estimated to ~30%. The low population of the site correlates with biophysical data indicating a weak binding affinity (estimated K_d of $6.79e^{-3}$ M). The binding affinity of Ir^{3+} for the wild-type enzyme is significantly weaker than that measured for Zn^{2+} (estimated K_d of $3.88e^{-6}$ M). This evidence suggests that Ir^{3+}-substitutions in the holo-

enzyme are highly unlikely and modifications at the active site should be introduced to improve the Ir^{3+}-binding.

	Ir-hCA2
Precipitant	2.7 M ammonium sulphate + 50 mM BIS-TRIS pH 6.5
DATA COLLECTION STATISTICS	
Diffraction source	P13 (PETRA III)
Wavelength (Å)	0.976
Temperature (K)	100
Detector	Eiger 16M
Crystal-detector distance (mm)	162.3
	0.002
Space group	$P2_1$
No. of subunits in ASU	1
a, b, c (Å)	42.49, 41.77, 72.80
β (°)	104.55
Resolution range (Å)	41.77-1.63 (1.63-1.60)
Total no. of reflections	218484 (11205)
No. of unique reflections	31499 (1609)
Completeness (%)	95.8 (99.6)
Multiplicity	6.9 (7.0)
I/σ(I)	9.1 (2.3)
CC(1/2)	0.99 (0.64)
R_{meas}	0.131 (0.904)
Overall B factor from Wilson plot ($Å^2$)	12.3
REFINEMENT STATISTICS	
Resolution range (Å)	41.16-1.60 (1.64-1.60)
Completeness (%)	95.6 (99.3)
No. of reflections, working set	29938 (2305)
No. of reflections, test set	1520 (94)
Final R_{cryst}	0.1849 (0.243)
Final R_{free}	0.2212 (0.259)
No. of non-H atoms	
Protein	260
Metal ion	1
Water	213
Total	474
R.m.s. deviation bonds (Å)	0.004
R.m.s. deviation angles (°)	1.124
Average B factor ($Å^2$)	15.3
Estimate error on coordinates based on R value (Å)	0.100
Ramachandran plot	
Most favored (%)	96.1
Allowed (%)	3.9

Table 4.5: Data collection, processing, and refinement statistic of structure Ir-hCA2 o. n. co-crystallization. Values in parentheses are for the highest-resolution shell.

The comparison with the structure of the holo-enzyme shows that the metal substitution at the catalytic site does not perturb the protein structure, as indicated by the low value of the rmsd upon Cα matching, resulting of 0.12 Å. Once focusing on the active site, some differences arise

from the peculiar coordination of the two metal ions. At variance with Zn^{2+} which has a tetrahedral geometry, Ir^{3+} favours pentagonal coordination, resulting in a distorted trigonal bipyramid. As a consequence of the change in the metal coordination sphere, the solvent network in the active site is also modified. W_{DW} and W_1 observed in the holoenzyme are not present in the Ir-adduct due to the hindrance generated by the metal coordination sphere. On the other hand, the position of W_2 almost overlaps in the two metal complexes. Furthermore, the proton shuttling His64 is fully rotated outside the cavity in both structures. At variance with the holo-enzyme where a second Zn^{2+} ion is anchored between the sidechains of His4 and His64, blocking the proton shuttling residue in the "out" orientation, no additional metal bindings are observed in the complex with Ir^{3+}(Figure 4.6).

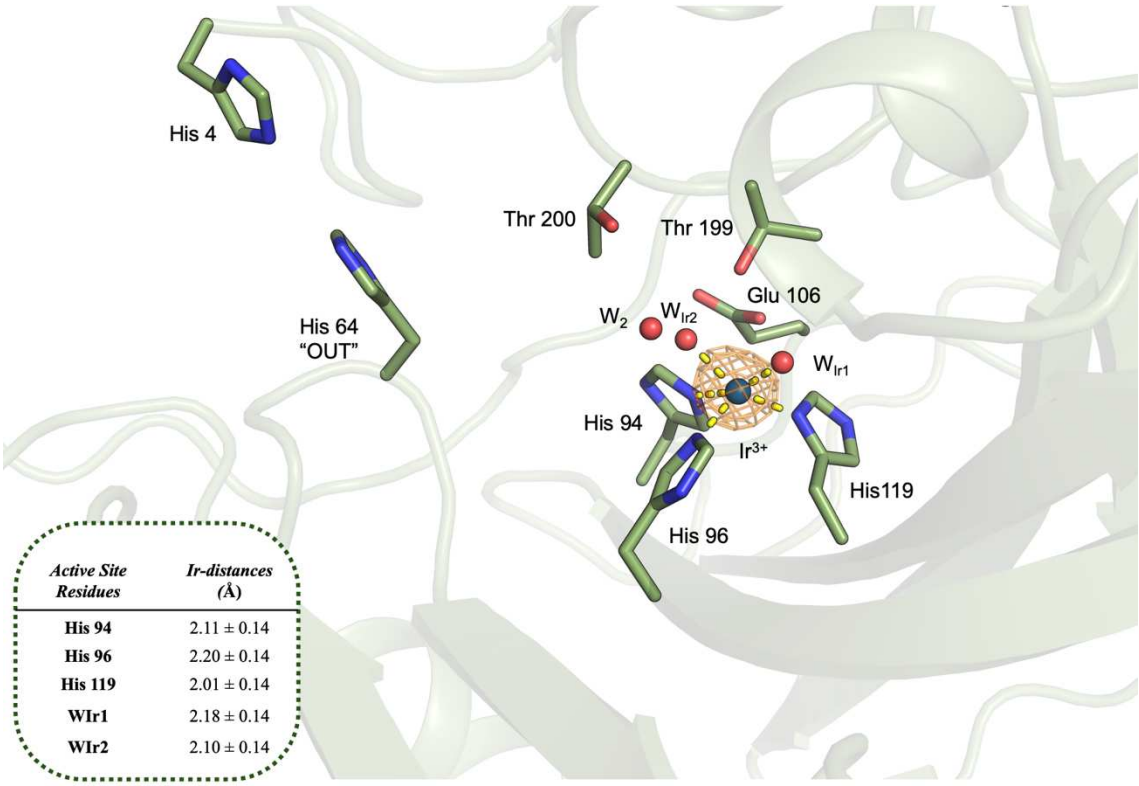

Active Site Residues	Ir-distances (Å)
His 94	2.11 ± 0.14
His 96	2.20 ± 0.14
His 119	2.01 ± 0.14
WIr1	2.18 ± 0.14
WIr2	2.10 ± 0.14

Figure 4.6: Interface view of Ir-hCA2 in cartoon. The interacting residues are shown in stick representation. The key water molecules are represented as red spheres. Iridium ion (blue sphere) is surrounded by the anomalous difference map contoured at 5.0 σ. Coordination bonds are illustrated as yellow dashed lines. Distances between Active Site Residues and iridium ion are shown in the panel.

4.3.4.1 Structural characterization of hCA2 alanine variants exposed to Ir^{3+}

The five alanine variants were exposed to Ir^{3+} ions and crystallized under the same conditions used to characterize the metal adduct with the wild-type enzyme. The crystals grown using the co-crystallization approach were very small, and they showed very poor diffraction patterns, preventing the structural characterization. The soaking approach was then attempted by exposing apo-protein crystals to concentrated solutions of Ir^{3+} for 16 h. Even so, it was possible to characterize the structures of all variants using this approach, no metal ions were observed binding to the proteins. This result was not surprising since the same approach was also not successful for the characterization of the Ir-adduct with the wild-type enzyme. A summary of the trials attempted on the alanine variants is shown in Table 4.6.

Protein	Precipitant	Co-crystallization	Soaking
Ir-H4A	2.7 M Ammonium Sulphate + 50 mM BIS-TRIS pH 6.5	No diffraction	No iridium
Ir-H94A	2.7 M Ammonium Sulphate + 50 mM BIS-TRIS pH 6.5	No diffraction	No iridium
Ir-H96A	2.7 M Ammonium Sulphate + 50 mM BIS-TRIS pH 6.5	No diffraction	No iridium
Ir-H119A	2.7 M Ammonium Sulphate + 50 mM BIS-TRIS pH 6.5	No diffraction	No iridium
Ir-H94A-H96A	2.7 M Ammonium Sulphate + 50 mM BIS-TRIS pH 6.5	No diffraction	No iridium

Table 4.6: The classification of Ir-hCA2 structures is represented using a color-coding system: red indicates structures where iridium is absent, orange represents structures where crystals showed poor diffraction patterns.

4.4 Conclusions

This chapter explores the effect of the incorporation of Ir^{3+} into the catalytic site of hCA2, expanding the biochemical evidence provided by the bovine CA(s)[17]. Our approach combined biochemical and biophysical assays with high-resolution structural characterization of the Ir-hCA2 complex. Despite the low incorporation rate, the Ir^{3+}-substituted form of the enzyme shows a distorted coordination geometry compared to the native Zn^{2+}-based protein. Metal binding studies corroborate our structural evidence, showing how the event is energetically favoured, but the affinity of the active site for the metal ion is low.

Overall, our experiments prove the relevance of Ir^{3+} in reprogramming the native activity of hCA2, converting it into an enzyme capable of the production of oxygen from water. This paves the road for future efforts to extend this approach to other metals of similar electronic properties or to alter the active site environment and improve metal binding and the efficiency of the water splitting reaction. Furthermore, dedicated mechanistic studies could help elucidate the stages of the complex 4-electron mechanism mediated by the enzyme. Our groundwork in establishing the conditions for the preparation of Ir^{3+}-substituted hCA2 crystals will be useful to extend the work to time-resolved crystallographic studies to track the formation of intermediates and of the product in the crystals.

4.5 References

(1) Housecroft, C. E. Iridium: Inorganic & Coordination Chemistry. In *Encyclopedia of Inorganic Chemistry*; King, R. B., Crabtree, R. H., Lukehart, C. M., Atwood, D. A., Scott, R. A., Eds.; Wiley, 2005. https://doi.org/10.1002/0470862106.ia101.

(2) Harriman, A.; Pickering, I. J.; Thomas, J. M.; Christensen, P. A. Metal Oxides as Heterogeneous Catalysts for Oxygen Evolution under Photochemical Conditions. *J. Chem. Soc. Faraday Trans. 1 Phys. Chem. Condens. Phases* **1988**, *84* (8), 2795. https://doi.org/10.1039/f19888402795.

(3) Singh, A. K.; Roy, L. Evolution in the Design of Water Oxidation Catalysts with Transition-Metals: A Perspective on Biological, Molecular, Supramolecular, and Hybrid Approaches. *ACS Omega* **2024**, *9* (9), 9886–9920. https://doi.org/10.1021/acsomega.3c07847.

(4) Kudo, A.; Miseki, Y. Heterogeneous Photocatalyst Materials for Water Splitting. *Chem Soc Rev* **2009**, *38* (1), 253–278. https://doi.org/10.1039/B800489G.

(5) Singh, A.; Spiccia, L. Water Oxidation Catalysts Based on Abundant 1st Row Transition Metals. *Coord. Chem. Rev.* **2013**, *257* (17–18), 2607–2622. https://doi.org/10.1016/j.ccr.2013.02.027.

(6) Andreiadis, E. S.; Chavarot-Kerlidou, M.; Fontecave, M.; Artero, V. Artificial Photosynthesis: From Molecular Catalysts for Light-driven Water Splitting to Photoelectrochemical Cells. *Photochem. Photobiol.* **2011**, *87* (5), 946–964. https://doi.org/10.1111/j.1751-1097.2011.00966.x.

(7) Blakemore, J. D.; Crabtree, R. H.; Brudvig, G. W. Molecular Catalysts for Water Oxidation. *Chem. Rev.* **2015**, *115* (23), 12974–13005. https://doi.org/10.1021/acs.chemrev.5b00122.

(8) Barber, J. Photosynthetic Water Splitting by the $Mn_4\ Ca^{2+}\ O_X$ Catalyst of Photosystem II: Its Structure, Robustness and Mechanism. *Q. Rev. Biophys.* **2017**, *50*, e13. https://doi.org/10.1017/S0033583517000105.

(9) Hull, J. F.; Balcells, D.; Blakemore, J. D.; Incarvito, C. D.; Eisenstein, O.; Brudvig, G. W.; Crabtree, R. H. Highly Active and Robust Cp* Iridium Complexes for Catalytic Water Oxidation. *J. Am. Chem. Soc.* **2009**, *131* (25), 8730–8731. https://doi.org/10.1021/ja901270f.

(10) Blakemore, J. D.; Schley, N. D.; Balcells, D.; Hull, J. F.; Olack, G. W.; Incarvito, C. D.; Eisenstein, O.; Brudvig, G. W.; Crabtree, R. H. Half-Sandwich Iridium Complexes for Homogeneous Water-Oxidation Catalysis. *J. Am. Chem. Soc.* **2010**, *132* (45), 16017–16029. https://doi.org/10.1021/ja104775j.

(11) Savini, A.; Bellachioma, G.; Ciancaleoni, G.; Zuccaccia, C.; Zuccaccia, D.; Macchioni, A. Iridium(Iii) Molecular Catalysts for Water Oxidation: The Simpler the Faster. *Chem. Commun.* **2010**, *46* (48), 9218. https://doi.org/10.1039/c0cc03801f.

(12) Savini, A.; Bucci, A.; Bellachioma, G.; Giancola, S.; Palomba, F.; Rocchigiani, L.; Rossi, A.; Suriani, M.; Zuccaccia, C.; Macchioni, A. New Iridium(III) Organometallic Complexes Bearing Strong Electron Donating Bidentate Ligands as Catalysts for Water Oxidation. *J. Organomet. Chem.* **2014**, *771*, 24–32. https://doi.org/10.1016/j.jorganchem.2014.05.029.

(13) Parent, A. R.; Brewster, T. P.; De Wolf, W.; Crabtree, R. H.; Brudvig, G. W. Sodium Periodate as a Primary Oxidant for Water-Oxidation Catalysts. *Inorg. Chem.* **2012**, *51* (11), 6147–6152. https://doi.org/10.1021/ic300154x.

(14) Tan, P.; Kwong, H.-K.; Lau, T.-C. Catalytic Oxidation of Water and Alcohols by a Robust Iron(III) Complex Bearing a Cross-Bridged Cyclam Ligand. *Chem. Commun.* **2015**, *51* (61), 12189–12192. https://doi.org/10.1039/C5CC02868J.

(15) Thomsen, J. M.; Huang, D. L.; Crabtree, R. H.; Brudvig, G. W. Iridium-Based Complexes for Water Oxidation. *Dalton Trans.* **2015**, *44* (28), 12452–12472. https://doi.org/10.1039/C5DT00863H.

(16) Hong, D.; Murakami, M.; Yamada, Y.; Fukuzumi, S. Efficient Water Oxidation by Cerium Ammonium Nitrate with $[Ir^{III}$ (Cp*)(4,4′-Bishydroxy-2,2′-Bipyridine)$(H_2$ O)$]^{2+}$ as a Precatalyst. *Energy Env. Sci* **2012**, *5* (2), 5708–5716. https://doi.org/10.1039/C2EE02964B.

(17) Kim, M.; Lee, S. Catalytic Water Oxidation by Iridium-Modified Carbonic Anhydrase. *Chem. – Asian J.* **2018**, *13* (3), 334–341. https://doi.org/10.1002/asia.201701543.

(18) McDaniel, N. D.; Coughlin, F. J.; Tinker, L. L.; Bernhard, S. Cyclometalated Iridium(III) Aquo Complexes: Efficient and Tunable Catalysts for the Homogeneous Oxidation of Water. *J. Am. Chem. Soc.* **2008**, *130* (1), 210–217. https://doi.org/10.1021/ja074478f.

(19) Wang, X.; Jia, J.; Huang, Z.; Zhou, M.; Fei, H. Luminescent Peptide Labeling Based on a Histidine-Binding Iridium(III) Complex for Cell Penetration and Intracellular Targeting Studies. *Chem. – Eur. J.* **2011**, *17* (29), 8028–8032. https://doi.org/10.1002/chem.201100568.

(20) Ma, D.; Wong, W.; Chung, W.; Chan, F.; So, P.; Lai, T.; Zhou, Z.; Leung, Y.; Wong, K. A Highly Selective Luminescent Switch-On Probe for Histidine/Histidine-Rich Proteins and Its Application in Protein Staining. *Angew. Chem. Int. Ed.* **2008**, *47* (20), 3735–3739. https://doi.org/10.1002/anie.200705319.

(21) Kabsch, W. *XDS*. *Acta Crystallogr. D Biol. Crystallogr.* **2010**, *66* (2), 125–132. https://doi.org/10.1107/S0907444909047337.

(22) Potterton, L.; Agirre, J.; Ballard, C.; Cowtan, K.; Dodson, E.; Evans, P. R.; Jenkins, H. T.; Keegan, R.; Krissinel, E.; Stevenson, K.; Lebedev, A.; McNicholas, S. J.; Nicholls, R. A.; Noble, M.; Pannu, N. S.; Roth, C.; Sheldrick, G.; Skubak, P.; Turkenburg, J.; Uski, V.; Von Delft, F.; Waterman, D.; Wilson, K.; Winn, M.; Wojdyr, M. *CCP* 4 *i* 2: The New Graphical User Interface to the *CCP* 4 Program Suite. *Acta Crystallogr. Sect. Struct. Biol.* **2018**, *74* (2), 68–84. https://doi.org/10.1107/S2059798317016035.

(23) Vagin, A.; Teplyakov, A. Molecular Replacement with *MOLREP*. *Acta Crystallogr. D Biol. Crystallogr.* **2010**, *66* (1), 22–25. https://doi.org/10.1107/S0907444909042589.

(24) Håkansson, K.; Carlsson, M.; Svensson, L. A.; Liljas, A. Structure of Native and Apo Carbonic Anhydrase II and Structure of Some of Its Anion-Ligand Complexes. *J. Mol. Biol.* **1992**, *227* (4), 1192–1204. https://doi.org/10.1016/0022-2836(92)90531-N.

(25) Murshudov, G. N.; Skubák, P.; Lebedev, A. A.; Pannu, N. S.; Steiner, R. A.; Nicholls, R. A.; Winn, M. D.; Long, F.; Vagin, A. A. *REFMAC* 5 for the Refinement of Macromolecular Crystal Structures. *Acta Crystallogr. D Biol. Crystallogr.* **2011**, *67* (4), 355–367. https://doi.org/10.1107/S0907444911001314.

(26) Emsley, P.; Lohkamp, B.; Scott, W. G.; Cowtan, K. Features and Development of *Coot*. *Acta Crystallogr. D Biol. Crystallogr.* **2010**, *66* (4), 486–501. https://doi.org/10.1107/S0907444910007493.

(27) Winn, M. D.; Ballard, C. C.; Cowtan, K. D.; Dodson, E. J.; Emsley, P.; Evans, P. R.; Keegan, R. M.; Krissinel, E. B.; Leslie, A. G. W.; McCoy, A.; McNicholas, S. J.; Murshudov, G. N.; Pannu, N. S.; Potterton, E. A.; Powell, H. R.; Read, R. J.; Vagin, A.; Wilson, K. S. Overview of the *CCP* 4 Suite and Current Developments. *Acta Crystallogr. D Biol. Crystallogr.* **2011**, *67* (4), 235–242. https://doi.org/10.1107/S0907444910045749.

(28) Williams, C. J.; Headd, J. J.; Moriarty, N. W.; Prisant, M. G.; Videau, L. L.; Deis, L. N.; Verma, V.; Keedy, D. A.; Hintze, B. J.; Chen, V. B.; Jain, S.; Lewis, S. M.; Arendall, W. B.; Snoeyink, J.; Adams, P. D.; Lovell, S. C.; Richardson, J. S.; Richardson, D. C. MolProbity: More and Better Reference Data for Improved All-atom Structure Validation. *Protein Sci.* **2018**, *27* (1), 293–315. https://doi.org/10.1002/pro.3330.

(29) Janson, G.; Zhang, C.; Prado, M. G.; Paiardini, A. PyMod 2.0: Improvements in Protein Sequence-Structure Analysis and Homology Modeling within PyMOL. *Bioinformatics* **2017**, *33* (3), 444–446. https://doi.org/10.1093/bioinformatics/btw638.

(30) Hetterscheid, D. G. H.; Reek, J. N. H. Periodate as an Oxidant for Catalytic Water Oxidation: Oxidation via Electron Transfer or O-Atom Transfer? *Eur. J. Inorg. Chem.* **2014**, *2014* (4), 742–749. https://doi.org/10.1002/ejic.201300249.

(31) Saito, R.; Sato, T.; Ikai, A.; Tanaka, N. Structure of Bovine Carbonic Anhydrase II at 1.95 Å Resolution. *Acta Crystallogr. D Biol. Crystallogr.* **2004**, *60* (4), 792–795. https://doi.org/10.1107/S0907444904003166.

(32) Håkansson, K.; Carlsson, M.; Svensson, L. A.; Liljas, A. Structure of Native and Apo Carbonic Anhydrase II and Structure of Some of Its Anion-Ligand Complexes. *J. Mol. Biol.* **1992**, *227* (4), 1192–1204. https://doi.org/10.1016/0022-2836(92)90531-N.

(33) Valkai, L.; Peintler, G.; Horváth, A. K. Clarifying the Equilibrium Speciation of Periodate Ions in Aqueous Medium. *Inorg. Chem.* **2017**, *56* (18), 11417–11425. https://doi.org/10.1021/acs.inorgchem.7b01911.

Chapter 5

Conclusions and Future Prospective

5.1 Final remarks

The present doctoral research led to significant insights into the structural and functional dynamics of human Carbonic Anhydrase II (hCA2), particularly in relation to its Zn^{2+} coordination, metal substitution, and catalytic properties. Through a multidisciplinary approach integrating site-directed mutagenesis, enzymatic kinetics, calorimetric titration, and high-resolution structural characterization, we have elucidated the fundamental role of Zn^{2+} in maintaining enzymatic activity and active site integrity.

Our studies on Zn^{2+} coordination residues (H94, H96, and H119) have demonstrated their crucial role in substrate binding and catalysis. The mutational analysis confirmed that any perturbation of these residues leads to significant structural rearrangements, reducing or completely abolishing enzymatic function. On the other hand, our findings on the secondary Zn^{2+} site suggested that, whilst not displaying a direct contribution during the catalysis, a secondary role in terms of structural stabilization and allosteric regulation might be occurring. Furthermore, the investigation of metal-substituted variants unravelled the impact of different transition metals on the enzymatic function upon zinc replacement. Amongst the screened metals, Co^{2+} has proven to be the only one displaying partial restoration of the native catalytic activity, while substitutions with Ni^{2+}, Fe^{2+}, Mn^{2+}, and Cu^{2+} induced significant structural and functional modifications within the catalytic pocket.

The incorporation of Ir^{3+} within the catalytic site was successful, and the performed experiments on the attained Ir-hCA2 proved the relevance of tuning the original enzyme activity towards photo-splitting. Despite a low incorporation rate, the Ir-hCA2 complex highlighted a distorted coordination geometry, leading to the conversion of hCA2 into an O_2-producing enzyme. This discovery paves the way for future research into artificial metalloenzymes capable of facilitating complex redox reactions, including water oxidation.

From a broader perspective, this work underscores the remarkable versatility of hCA2 as a scaffold for enzyme engineering applications. The ability to express and modify hCA2 in *E. coli*, combined with its intrinsic stability under diverse experimental conditions, makes it a compelling candidate for green chemistry, and energy production.

Appendix 1

Participation at conferences and congresses

Abstract and poster

Beatrice De Bonis, Giusy Tassone, Marco Mazzorana, Cecilia Pozzi. **Production, characterization, and optimization of engineered enzymes for application in artificial photosynthetic systems**. Poster at National Congress of the Division of Chemistry of Biological Systems (Italian Chemistry Society), SCI2022, June 20-22nd, 2022, Napoli (Italy).

Beatrice De Bonis, Giusy Tassone, Marco Mazzorana, Cecilia Pozzi. **Production, characterization, and optimization of engineered enzymes for application in artificial photosynthetic systems**. Poster at 4th Joint Italian Crystallographic Association (AIC) and Italian Synchrotron Radiation Society (SILS) Conference. September 12-15th, 2022, Trieste (Italy).

Beatrice De Bonis, Giusy Tassone, Marco Mazzorana, Cecilia Pozzi. **Production and characterization of metal substituted human Carbonic Anhydrase II for artificial photosynthesis.** Poster at 50th Meeting of Italian Crystallographic Association (AIC), September 5-8th, 2023, Bologna (Italy).

Beatrice De Bonis, Giusy Tassone, Marco Mazzorana, Cecilia Pozzi. **Production and characterization of metal substituted human Carbonic Anhydrase II for artificial photosynthesis.** National Congress of the Division of Chemistry of Biological Systems (Italian Chemical Society), SCI2023, September 27-29th, 2023, Milano (Italy).

Beatrice De Bonis, Giusy Tassone, Marco Mazzorana, Cecilia Pozzi. **Characterization of different metal adducts in human Carbonic Anhydrase II for artificial photosynthesis.** XXVIII National Congress, SCI2024, August 26-30th, 2024, Milano (Italy).

Further School and Congress

- 3rd Italian Crystallographic Association Biological Macromolecules group meeting, May 23-24th, 2022 Fiesole (Italy).

- Idrogeno: quale ruolo nella transizione energetica? May 27th, 2022, Bologna (Italy).

- Workshop via Zoom: Systems Chemistry in Italy - Emerging Properties from Complex Chemical Systems, September 25th , 2023, Roma (Italy).

- Summer school Emory Unisi, Chemistry for Life & Environment Education, Collaboration, Innovation. XIX Edition. Lab session – Giusy Tassone & Beatrice De Bonis. Crystallization of N-terminal domain of human heat shock protein 90 (hHsp90-NTD). May 27th - 4th July 2024, Siena (Italy).

-